UNIVERSITÉ DE STRASBOURG

ÉCOLE DOCTORALE de Physique et Chimie-Physique

Institut de physique et chimie des matériaux de Strasbourg (IPCMS) UMR 7504

THÈSE présentée par :

Deeksha GUPTA

soutenue le : 5 **April 2024**

pour obtenir le grade de : **Docteur de l'université de Strasbourg**

Discipline/ Spécialité : Condensed Matter Physics

Polarized Hot Electron Induced Ultrafast Magnetization Dynamics in Ferrimagnet-based Spin Valve Structures

THÈSE dirigée par :

Mme BOEGLIN Christine	Directeur de Recherche, IPCMS, Université de Strasbourg

RAPPORTEURS :

M KUCH Wolfgang	Professeur, Freie Universität, Berlin, Germany
M VODUNGBO Boris	Maître de Conférence, LCPMR, Sorbonne Université, Paris

---

AUTRES MEMBRES DU JURY :

Mme BUDA PREJBEANU Liliana	Professeur, SPINTEC, Grenoble
M RUELLO Pascal	Professeur, IMMM, Le Mans Université, Le Mans
M ALOUANI Mebarek	Professeur, IPCMS, Université de Strasbourg,

---

Invitées:

M SIROTTI Fausto	Directeur de Recherche, Ecole Polytechnique, Palaiseau
M HOLLDACK Karsten	Beamline Scientist, HZB-BESSY II, Berlin
M HEHN Michel	Professeur, IJL, Université de Lorraine, Nancy
M BERGEARD Nicolas	Charge de Recherche, IPCMS, Université de Strasbourg

Abstract

The generation of spin currents is a key ingredient in the spintronics based memory devices such as spin transfer torques - magnetic random-access memory. Advances in ultrafast magnetism [1] in the last decade have demonstrated that the switching time can be reduced to the sub-picosecond time scales with low power consumption [1]. Ever since this pioneer works, several experiments on ferromagnetic 3d transition metals have studied the ultrafast spin dynamics induced by such fs spin currents in spin-valve structures [2–7], while recent studies suggest that antiferromagnetic materials are more promising for ultrafast spintronics [8]. Among these AFM materials, the rare-earth/ transition metal (RE-TM) alloys represent model systems [8,9]. Here, I investigate the sub-picosecond and picosecond spin current-induced demagnetization dynamics in RE-TM alloys. To distinguish the element-specific dynamics, I used the element-selective technique of Time-resolved X-Ray Magnetic Circular Dichroism available at the large-scale infrastructures HZB-BESSY II - Berlin.

In this thesis work, the focus is on studying the ultrafast demagnetization dynamics of thin buried ferrimagnetic layer (FeGd and CoGd alloys), using the ultrashort spin-polarized hot-electron (SPHE) pulses as a pump and ultrashort X rays as a probe.

I have explored the impact of SPHE induced effect on two different spin valve structures consisting of out-of-plane $Fe_{74}Gd_{26}$/Cu/{Co/Pt}*3 , and of an in-plane $Co_{61}Gd_{39}$/Cu/CoPt. The key findings are summarized as follows:

In $Fe_{74}Gd_{26}$ based spin valves:

- In the case of out-of-plane $Fe_{74}Gd_{26}$ based spin-valves, we investigated the spin-polarized hot electron induced dynamics of Fe 3d and Gd 4f moments, and through fitting, crucial parameters such as demagnetization time, hot electron pulse width, and recovery were obtained. The estimation of hot electron pulses highlighted their elongation as they traversed different capping layers.
- I observed that ultrafast spin current accelerated the Fe3d dynamics in the case of P configuration, which shows that antiparallel spins between Fe3d and SPHE spins help in the demagnetization of the Fe3d sublattice.
- Theoretical calculations based on atomistic spin dynamics with STT successfully reproduced the spin dependent demagnetization dynamics at Fe and Gd edges. The calculations approximated that the thin polarizer film Co/Pt could generate 100 % polarization of the spin current and show that the spin polarization of the SPHE current out of Co/Pt multilayers is opposite to the Co magnetization.

In $Co_{61}Gd_{39}$ based spin valves:

- A slow demagnetization of the hot-electron induced dynamics at Gd4f sublattice could be related to the concentration of such alloys irrespective of the excitation source (laser light or hot electron pulses).
- I observed that ultrafast spin current accelerated the Gd4f dynamics in the case of AP configuration, which shows that parallel spins between Gd4f and SPHE spins help the demagnetization of Gd4f sublattice.
- The surface-sensitive soft X-ray photoelectron spectroscopy (XPS) technique has evidenced a concentration profile of Gd at the surface of the GdCo alloy. The profile shows an enhanced Gd content in the first 2 nm in $Co_{65}Gd_{35,}$ whereas, for a $Co_{80}Gd_{20}$ alloy, a single segregated Gd monolayer on the top of an almost homogenous alloy was defined.

Acknowledgement

I would like to thank everyone who helped me professionally and personally during this journey of four year of my Ph.D.:

First and foremost, I thank Christine Boeglin for giving me the opportunity to work at the IPCMS. I thank her for introducing me to the field of ultrafast magnetism, for providing excellent advice in my doctoral research, for offering opportunities to participate in beamtime with other projects and groups, and for her support in numerous non-academic situations relating to administration, etc. Since my arrival in Strasbourg, her support has been invaluable.

I would like to thank Nicolas Bergeard for the discussions and suggestions. His support through all the beamtimes and advise with all the scientific and technical things helped me to further improve my knowledge.

I thank Matthias Riepp, for helping me in different ways either solving in error in python code or in clearing some doubts. I had amazing time with you sharing the same office in last two years.

I thank Niko Pontius, Christian Schüßler-Langeheine and Karsten Holldack for their assistance during all the beamtimes onsite and remotely during COVID period, for hosting me during my secondment for two months at Femtoslicing beamline, BESSYII. I am thankful to them for explaining me in great detail the working principle of slicing facility.

I thank Radu Abrudhan for his assistance during static XMCD measurements at PM3, BESSYII, Berlin.

I thank Michel Hehn for preparing all the samples for this project work and following all the discussion and providing suggestion.

I thank to Tom Ferte for doing SEM imaging on my samples.

I thank Prof. Olle Eriksson and Maryna Pankratova for theoretical calculations and discussions for the spin hot electron project.

I thank Prof. Fausto Sirotti and Matthieu Silly for their support during TEMPO beamtime for XPS measurements at SOLEIL, Paris. I am thankful to Prof. Fausto for all the discussion and teaching the XPS measurements.

I thank Emmanuelle Jal, Sorbonne University for giving me chance to participate in the TR-XRMR measurement at FLASH II, Hamburg. During this beamtime, I had a chance to meet many amazing people and learned how to do reflectivity measurements.

I thank to Matthias pace for your help during different beamtimes, discussions and also in many non-professional ways, while settling in Strasbourg.

I thank Prof. Ovidiu Ersen and Antonio Stocco for being thesis committee members and following my work over last three years.

I would like to thank all the jury members for reviewing my thesis work and fruitful discussion during the defense.

I would like to thank all the administrative people who helped me to deal with bureaucratic work, especially, our first program coordinator Nataliia Voivoda, for constant help in official and non-official work. I thank Catherine Bonnin, Mme. Monnin and Celine for helping in missions, reimbursement and purchase order over the years.

I am very thankful to QUSTEC PhD Program which supported by funding from the European Union's Horizon 2020 research and innovation programme under the Marie Skłodowska-Curie grant agreement number 847471. I am also very thankful to my department DSI and supervisor, Christine Boeglin for providing additional co-funding for three-month extension at the end of my thesis contract.

I also fondly remember my master thesis supervisor Prof. Pranaba Kishor Muduli, who introduced me to spintronic research and for providing me the platform to begin my research career.

I would like to thank Erika and Gunther for their love and care.

Soon after my arrival COVID broke out and before knowing people, I was locked in my room. But, today, I feel very lucky to have many friends in Himanshi, Jinu, Jose, Matthias, Naveen, Nivedita, Pankhuri, Rekha, Ritika, Satakshi, Shivangi, Smriti, Sushmita, Swarnshikha, Valentina, Vineesha, and Yamini, thank you all for being with me in different phases.

I would like to thank Anmol for his constant support in all aspect in my life either in personal or professional, scientific or non-scientific. Thanks for being constant in my life. I can never be thanking you enough.

I am very grateful to my Uncle, Ashok Tau ji, who always believed in me and motivated me to keep progressing and helped in all possible ways.

I am deeply grateful to my family—Maa, Papa, Sakshi (sister), and Keshav (brother)—for their unwavering love and support, which made it possible for me to achieve this. Their encouragement has been invaluable. I dedicate my thesis to my family with heartfelt thanks for everything.

Thank you everyone!

Table of Contents

Chapter 1 Introduction

The theoretical demonstration of the existence of the spin quantum state of electrons is already a hundred years old. Since then, magnetic domains have shown their importance in many research fields. One of the most important applications nowadays is modern information technology for magnetic recording media. More than 60 years ago, conventional manipulation by external magnetic fields was used in Hard Disk Drive (HDD) and in Heat Assisted Magnetization Recording (HAMR) [10]. The increase in data storage capacity and faster access time not only leads to reduced dimensions of the domains encoding the information but also the need for faster access times.

In this context, it was a revolution in the recording industry when Giant magnetoresistance (GMR) was discovered by Albert Fert [11] and Peter Grunberg [12] in 1988. It led to the beginning of a new era in modern magnetism called Spintronics [13,14]. Resistivity was shown to change via the mechanism of spin-dependent scattering between two parallel–antiparallel magnetic layers in spin-valve structures. This work initiated new developments, for instance, the Magnetoresistive Random-Access Memory (MRAM) [15].

In parallel, magnetic writing has been further developed using different methods, such as field-, current- and light-induced switching of magnetic nanodomains. The advantage of electronically induced devices over conventional magnetic field-driven devices lies in their low power consumption, one of the most current problems today. Because today's needs also ask for faster processing time at the lowest possible costs, new concepts combine current- and light-induced methods based on ultrashort pulses of spin-polarized currents, introducing the concept of Spin transfer torque (STT) in spin valve structures [16,17]. STT-based devices have been on the market since 2016 [18], and switching time can be fast, up to 200 ps [13], but on the cost of reducing pulse duration, hence the switching energy. Despite all the above-mentioned switching processes used in memory devices, all these effects revolve around one crucial element: Spin current. Understanding its generation, optimization, and interaction with other magnetic layers is essential for further technological improvement.

In the same year as the discovery of STT, in 1996, the discovery of ultrafast demagnetization dynamics by Bigot and Beaurepaire in 1996 opened a new field of research in magnetism called femtomagnetism. They observed that on shining an IR laser pulse, the magnetization of Ni film can be quenched within less than 1 ps [19]. This discovery spared many experiments confirming

the ultrafast magnetization dynamics across various materials, including conventional transition metal ferromagnets such as Fe, Ni, and Co [20] as well as pure rare-earth magnets (Gd, Tb, Dy) [20,21] and alloys showing out-of-plane anisotropy [22–25].

A study by Stanciu et al. showed that magnetization of a GdCoFe ferrimagnetic alloy can be reversed using a circular polarized laser of 40 fs duration without applying any magnetic field [26]. This phenomenon, known as helicity-dependent all-optical switching (HD-AOS), enables deterministic switching using either left or right circular polarized light [26]. Soon after, Radu et al. illustrated that even linearly polarized light could induce the magnetization reversal in GdCoFe alloys, introducing the concept of helicity-independent all-optical switching (HI-AOS) [27].

Besides their technological significance, the exploration of materials on the femto-picosecond time scale offers intriguing insights from a fundamental perspective. This particular time scale corresponds to the fundamental magnetic interactions such as exchange interaction, spin-orbit coupling, and magnetic anisotropy [28]. Several mechanisms have been proposed to elucidate the loss of magnetization at fs time scale, including three- temperature model by Bigot [19] as well as several local [20,29–31] and non-local mechanisms [2,32]. Among them, the non-local mechanism, introduced by Battiato et al. and known as superdiffusive spin transport, explained that loss of magnetization on laser excitation is due to the migration of laser-excited electrons into the adjacent metallic layer [32]. This process generated the superdiffusive spin current (SC) in an ultrafast regime due to spin dependent mean free paths of the excited electrons. Before developing this superdiffusive model, Malinowski et al. experimentally demonstrated the transport of spin angular momentum upon laser excitation in a magnetic multilayer structure [3]. Subsequently, different groups employed the concept of superdiffusive spin current to manipulate the magnetization of adjacent magnetic layers [5,6,33–35] and generate spin current pulses in the THz range [36]. Recently, work from Igarashi et al. [7] showed the switching in ferromagnetic spin valve structure less than a picosecond even with the use of 80 nm of Cu between two magnetic layers, merging Spintronics and femtomagnetism. They observed the antiparallel orientation of both magnetic layers in the spin valve that favors the hot-electron (HE) induced switching of the soft layer [6,7]. Surprisingly, other counterintuitive results revealed that some spin valve systems show switching in the soft layer only for a parallel orientation of the hard and soft layer [35]. Those results conclude that the orientation for successful switching depends on the fluence in a given spin-

valve system, which again raises questions about multiple mechanisms behind spin switching.

Studies using element and magnetic-sensitive time-resolved X-rays have shown that laser-induced hot electrons can be used as indirect excitations of the ultrafast demagnetization in Ni [37], work which was followed by many others [38–40]. Up to this date, such studies have also considered different ferrimagnets, including TM-RE alloys [24,41]. However, no spin polarized effects in the HE-induced demagnetization have yet been studied in 4f RE and TM-RE alloys. This is one of the motivations of my thesis work, which focuses on describing spin-polarized current-induced ultrafast demagnetization with element selectivity in RE-TM ferrimagnets, important materials to push Spintronics and magnetic data storages towards the sub-picosecond regime. These materials are also among systems that show single pulse all-optical switching, an important property for applications using ultrafast spintronics [26,27,42–44]

1.1 Motivation for this thesis work:

Until now, several experiments have studied the ultrafast spin dynamics induced by such fs spin currents in spin-valve structures [3,5,6]. However, these works were focused on the direct excitation of magnetic multilayers, and spacer layer was too thin to avoid excitation of the bottom magnetic layer, and that led to a complex to study the spin current solely. Another approach can be to block IR light and use HE pulses [37–41,45] to excite the magnetic structure and polarize the HE current before the detection layer. However, these works are focused on ferromagnetic 3d transition metals. Recent studies suggest that antiferromagnetic materials (AFM) are more promising for ultrafast magnetization control in ultrafast spintronics devices [46]. Among these AFM materials, the rare-earth / transition metal (RE-TM) alloys represent model systems [9]. Over the past years, many studies have been carried out to observe AOS in such types of model systems [27,47,48]. Due to the different temperature dependence of two magnetic sublattices, i.e., 3d and 4f moments, both sublattices possess different dynamics on heating with intense IR Laser systems.

Additionally, these alloys show a variety of electronic and magnetic properties on changing the atomic concentration and temperature [49,50]. Therefore, studying such materials is very crucial for engineering the different materials for further advancement in magnetic devices. Therefore, it's crucial to understand the impact of polarized spin currents on these materials.

Therefore, to understand the behavior of spin current, Here, I investigate the femtosecond spin polarized hot electron induced spin dynamics in such RE-TM alloys. To observe the spin current induced effect on TM 3d as well as Gd 4f moments, I utilized the element-selective time-resolved X-ray magnetic circular dichroism technique at femtoslicing beamline at HZB-BESSY II, Berlin. This large-scale facility provides ultrashort X-ray pulses of ~100 fs as a probe with circular polarization, and their energy can be tuned up to 1300 eV. Therefore, using such state of the art experiment, we can resolve the element-specific dynamics in RE-TM alloy systems. Additionally, the theoretical modeling based on atomistic spin-dynamics simulations [50,51] reproduces the experimental ultrafast dynamics of this system, a fact that allows us to identify the microscopic process of spin angular moment transfer at the femto- and picosecond time scale.

1.2 Thesis structure:

The work done in this thesis is guided by the needs described above and, thus, understanding the mechanisms at work microscopic during spin-polarized current-induced demagnetization in TM-RE alloys. More precisely, we aimed to evidence time-resolved effects in both sublattices, 3d TM and 4f RE moments. The microscopic processes defining the ultrafast excitation by ultrashort spin currents of such complex multi-sublattice ferrimagnets need detailed and microscopic understanding in the subpicosecond time scale.

We used a method combining element and magnetic sensitivity experiment with femtosecond time resolution at the FemtoSpex beam line of HZB-BESSY II.

Relying on the TM-RE composition and interatomic exchange, theoretical modeling based on atomistic spin-dynamics simulations allows to reproduce the results and identify the microscopic process of spin angular moment transfer at the shortest time scale. This work has been conducted in collaboration with the group of O. Eriksson – Uppsala.

This thesis is organized as follows:

Chapter 2 Provides an overview of the theoretical framework crucial to this work. This includes fundamental magnetic interactions and their associated temporal scale, the ultrafast magnetization dynamics and different mechanisms involved, and the generation and propagation of hot electrons and spin currents in magnetic media. I will briefly explain the properties of the rare earth (RE) – transition metal (TM) alloy system. In the last, we explore the

fundamentals of light-matter interactions and elucidate the principles of different magneto-optic phenomena. Subsequently, I will discuss the key concepts of X-ray-based phenomena, including X-ray absorption spectroscopy (XAS), and X-ray magnetic circular dichroism (XMCD).

Chapter 3 Includes the various lab-based, such as magneto-optic Kerr magnetometry (MOKE) and large-scale X-ray-based experimental techniques like XAS-XMCD at PM3 beamline, BESSYII, Berlin and XPS at TEMPO beamline, SOLEIL synchrotron, Paris, employed for sample characterization. Additionally, I discuss the femtoslicing facility at FemtoSpex beamline, BESSYII, utilized for time-resolved XMCD to measure the element-specific dynamics.

Chapter 4 Elaborates on the significance of complex sample structure used in spin-polarized hot electron study. I will discuss the static characterization study performed to optimize the spin valve sample structure, which consists of different RE-TM alloy-based systems.

Chapter 5 I explore the spin-polarized hot electron induced ultrafast dynamics measured at Fe L_3 and Gd M_5 in FeGd alloy systems, focusing on the system with out of plane anisotropy easy axis. The experiments are compared with the theoretical calculations (performed by Maryna Pankratova, Uppsala University) based on atomistic spin dynamics combined with spin transfer torque.

Chapter 6 is divided into two parts – The first part focuses on presenting the spin-polarized hot electron induced dynamics recorded at Gd M_5 edge in CoGd system, with in-plane magnetic anisotropy easy axis. Additionally, I also discuss the hot-electron induced dynamics of CoGd systems. The second part of this chapter involves investigating Gd segregation on the surface of CoGd alloy as a function of Gd composition, using surface sensitive X-ray photoemission spectroscopy.

Chapter 7 In the final chapter of this thesis, I provide a comprehensive summary of the significant findings and contributions made throughout the study and address open questions to inspire further discussion and exploration in the field.

Chapter 2 Fundamentals

This chapter explores the background of theoretical aspects used in this thesis. It contains the different magnetic interaction and their time scale, ultrafast magnetism, and different models to explain the ultrafast magnetization dynamics, generation, and propagation of laser-excited unpolarized and spin-polarized hot electrons. Then, I discuss the magnetic properties and importance of Rare-Earth (RE) – Transition Metal (TM) based ferrimagnetic materials. Subsequently, in the last section, light-matter interactions and various phenomena based upon this are discussed.

2.1 Magnetic interactions and their time scale

This section describes the relevant magnetic interactions and their respective time scales. The main focus of this part is to discuss the interaction in terms of their energy and corresponding time scale and their relevance for ultrafast magnetism.

The most important and strongest interaction in condensed matter magnetism is the exchange interaction. It is responsible for the existence of different magnetic ordering, i.e., parallel (ferromagnetism) and antiparallel (antiferromagnetic). The exchange interaction is purely a quantum mechanical phenomenon and originates as a result of the electrostatic Coulomb interaction between electrons and the Pauli exclusion principle, which states that no two electrons can stay in the same quantum state. The total wave function must be antisymmetric. The total wave function is the combination of a spatial and a spin component. According to Pauli, for the symmetric spatial components, i.e., two electrons tend to have the same quantum numbers *n, l, m* but have to have different spin quantum numbers *s*. This leads to antiparallel spin orientation of both electrons and vice versa for the antisymmetric spatial function.

Heisenberg, in 1927, proposed a theoretical model describing the microscopic origin of exchange interaction, known as Heisenberg Hamiltonian, which can be written as follows:

$$H_{ex} = -\sum_{i \neq j} J_{ij}\, \overrightarrow{S_i}.\overrightarrow{S_j}$$

Where, $\overrightarrow{S_i}$ and $\overrightarrow{S_j}$ are the spins at site i and j, respectively. J_{ij} is the exchange interaction parameter. In the case of parallel orientation of both spins, J_{ij} must be positive to minimize the total energy of the system and hence originates

ferromagnetic, and the antiparallel alignment favors the negative value of J_{ij} and creates the antiferromagnetic ordering [52]. Exchange interaction can be direct or indirect, depending on the presence of a mediator. When the electrons from neighboring magnetic atoms interact directly via exchange interaction, which is called direct exchange, most itinerant ferromagnets (Fe, Ni, and Co) have magnetic ordering due to direct exchange. In the absence of direct overlapping of the electron orbitals, for instance, in the case of localized 4f moments, the indirect exchange takes place through the intermediate electrons. This type of indirect exchange is termed as Runderman-Kittel-Kasuya-Yosida (RKKY) interaction [53]

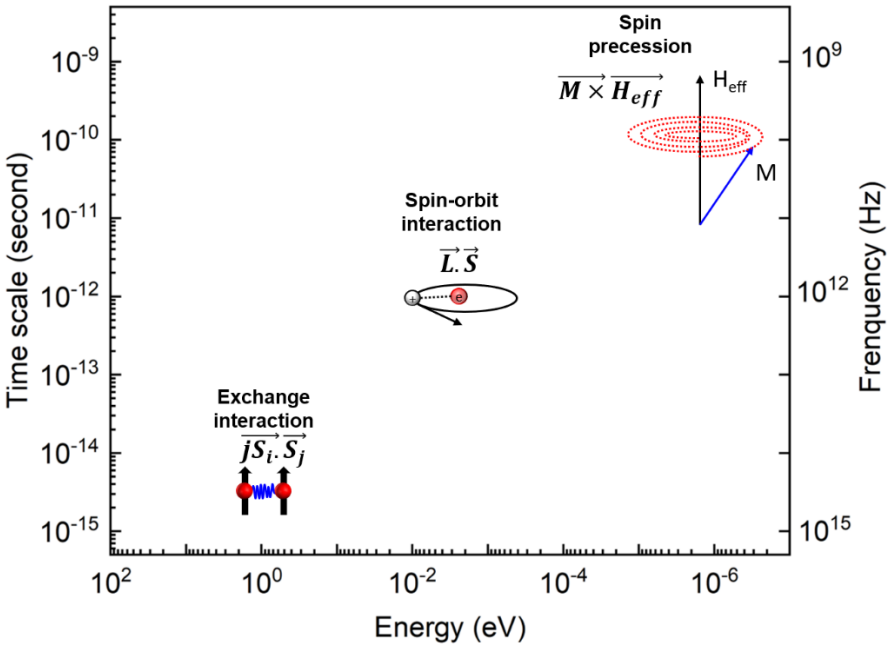

Figure 2.1: Fundamental magnetic interactions and their corresponding time and associated frequency scale given by t = h/E (adapted from [28])

Spin-orbit interaction (SOI) is the second important interaction. It is the relativistic interaction between the spin and the orbital motion of the electrons. This can be understood by considering the electron in the rest frame and positive nuclei revolves around the electron and generates the magnetic field. This field interact with its intrinsic spin, and give rise to spin-orbit coupling. It can be stated as the coupling of orbital motion of electron inside an electric field couples with its spin. The SOI is the origin of magnetocrystalline anisotropy, which leads to align the magnetization in preferred directions.

The Hamiltonian of SOI can be written as [52]:

$$H_{SOI} = \frac{e^2}{4\pi\epsilon_0 m_e^2 c^2 r^3} \vec{L}.\vec{S}$$

Where m_e, and e are the electronic mass and charge. c is the speed of light, and r is the atomic radius. L and S are the orbital and spin momentum. Therefore, it allows the transfer of the angular momentum between spin and lattice within the material.

Figure 2.1 shows the relation among these interactions and their respective time scales based on time-Energy correlation: t = h/E, particularly for 3d metals [28]. The important magnetic interactions, the interatomic exchange energy, atomic spin-orbit energy, and spin precession occur at femto to nanosecond time scale and within the frequency domain of TeraHertz (THz) to GigaHertz (GHz) range depending on their energies.

The discovery of magnetization manipulation at femto-picosecond time scale [19] opened a new research era. The femtosecond light sources provide a path to study these fundamental interactions at this ultrashort time scale, which is not possible by using conventional electromagnets.

2.2 Ultrafast magnetism

The work by Beaurepaire et al. demonstrated the first experimental evidence of sub picosecond demagnetization in a ferromagnet [19]. In this work, they used the time-resolved magneto-optic Kerr effect, in which the Ni film was excited by a femtosecond IR pulse of duration 60 fs, and probed the change in magnetization by recording the hysteresis as a function of pump-probe delay. They observed the sharp reduction in magnetization within 1 ps, faster than previously estimated spin-lattice relaxation time for ferromagnets (30ps) [54]. This work ignited the field of ultrafast magnetism, also named femtomagnetism. Until now, several experiments on different types of magnetic materials have confirmed the ultrafast demagnetization dynamics. However, the microscopic modeling of the phenomena is still under debate.

Since 1996, the research has opened many questions:

- How fast magnetization can be changed?
- What are the mechanisms responsible in ultrafast demagnetization?
- How is the angular momentum conservation followed upon the laser excitation?

Several theoretical mechanisms have been proposed to explain the loss of magnetization at this time scale. In the next sections, I will discuss the different models that have been used to explain ultrafast magnetization dynamics.

2.2.1 Electron excitation and thermalization

As explained in the previous section, when an intense IR laser pulse (1.5 eV) shines on the metal surface, electrons close to the Fermi level absorb the photon energy and excite the electrons to the empty states above Fermi energy. The process of hot electron excitation in metal by laser is shown in Figure 2.2. The excitation and relaxation process on laser pulse excitation can be explained in three steps: first, it creates a *non-thermal hot electron distribution above Fermi energy up* to the energy equal to incident photons. The optically excited electrons do not obey the Fermi-Dirac distribution. The resulting non-Fermi distribution is shown by a hypothetical rectangular shape in Figure 2.2 (b). The dimensions are determined by the energy of the excited laser (hv) and the absorbed energy density.

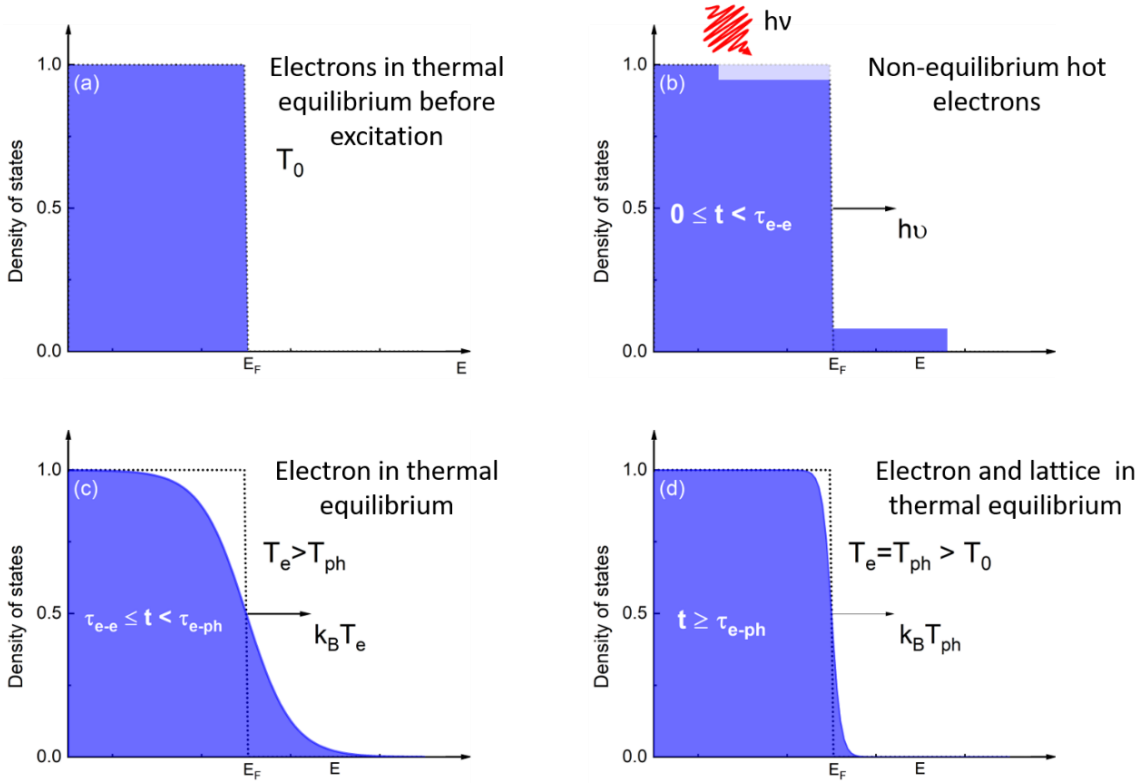

Figure 2.2: Electron excitation and relaxation processes in 4 steps: (a) The Fermi-Dirac distribution function as a function of energy at T_0 in equilibrium. (b) Non-thermal hot electron generation at t =0 upon excitation by an optical laser pulse and excites the hot electrons above E_F, which can move with ballistic velocities, (c) Electrons reach to thermal equilibrium by electron-electron scattering at characteristic times of t = $\tau_{e\text{-}e}$, and follow Fermi-Dirac distribution with the temperature T = T_e higher than lattice temperature and propagates with diffusive velocity (10^4 m/s). (d) Electrons transfer their energy to the lattice by electron-phonon scattering.

These excited electrons travel with the Fermi velocity, i.e., 10^6 m/s deeper to the sample, depending on the mean free paths (λ_e) of electrons [55]. The mean free path of an electron depends on the number of empty states above the Fermi level (E_F) and the impurity states. Figure 2.3 shows the correlation between the mean free path with the number of d states available above E_F (Figure taken from C. E. Graves [56]).

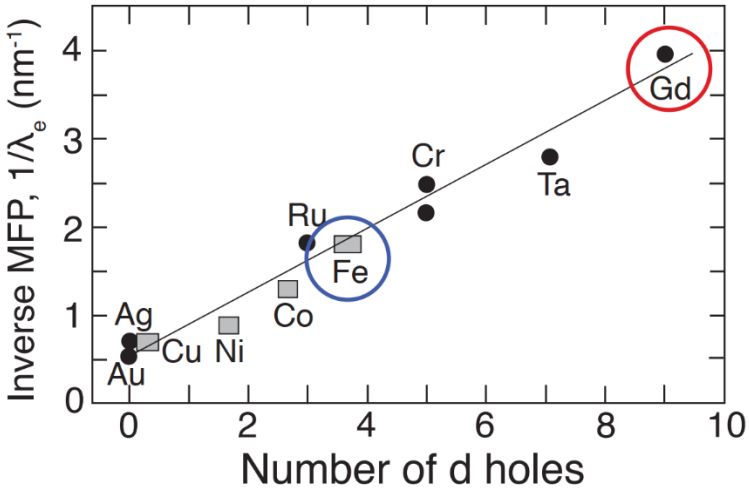

Figure 2.3: Dependence of mean free path on the number of empty states (number of d holes) above Fermi level for different elements, Figure taken from C. E. Graves [56].

Furthermore, these excited hot electrons come into thermal equilibrium by partially transferring their energy to other electrons by inelastic electron-electron scattering (50-500 fs), resulting in the generation of a cascade of secondary electrons with lower energies. Upon thermal equilibrium of hot electrons (shown in Fig. 2.2 c), the electronic distribution returns to the Fermi-Dirac distribution with the electronic temperature T_e. These hot electrons diffuse deeper into the bulk with relatively slower velocity ~10^4 m/s than ballistic. The diffusion length depends on the electron-phonon coupling, which helps electrons to come under equilibrium with lattice (within 100 fs – 1 ps) (Figure 2.2 (d)).

2.2.2 Three temperature (3TM) model

Beaurepaire et al. [19] provided a phenomenological model to describe the ultrafast magnetization dynamics. In their model, they consider electron, spin and lattice as separate but coupled reservoirs, as shown in Figure 2.4(a). Their coupling efficiency depends on the different coupling parameters, electron-spin (G_{es}), electron-lattice (G_{ep}), and spin-lattice (G_{sp}). This

thermodynamic model was an extension of earlier developed 2 temperature model [57]. The earlier model explained the laser induced electron dynamics in normal metals. Beaurepaire et al. included spin as a third reservoir which has its own specific heat (c_e), electron-spin (G_{es}), and spin-lattice (G_{sp}) coupling, as illustrated in Figure 2.4.

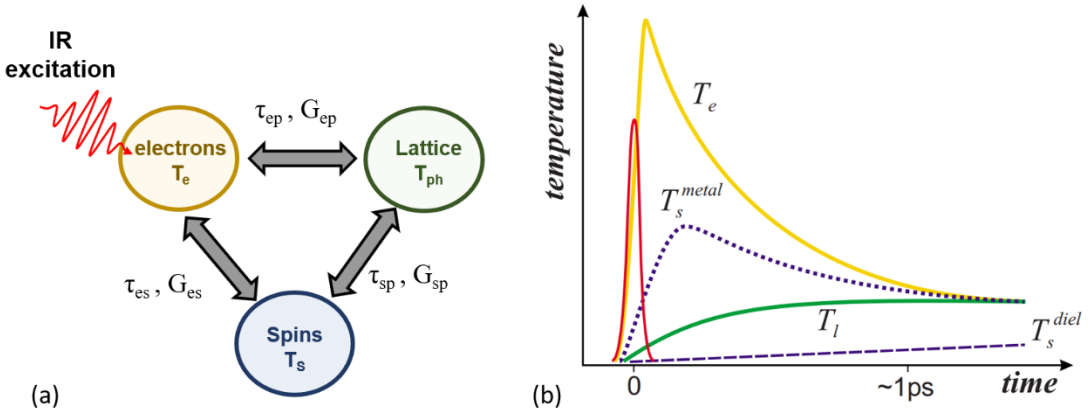

Figure 2.4: Phenomenological 3 temperature model (3TM). (a)Three coupled heat reservoirs – Electron, spin and lattice, which exchange their energies upon laser excitation of electronic system. (b) Temperature profile of three systems as function of time. After 1 ps, all three systems come under equilibrium (taken from [58]).

The 3 TM can be described in three coupled equations, as follows:

$$c_e(T_e)\frac{dT_e}{dt} = -G_{ep}(T_e - T_p) - G_{es}(T_e - T_s) + P(t)$$

$$c_s(T_s)\frac{dT_s}{dt} = -G_{es}(T_s - T_e) - G_{sp}(T_s - T_p)$$

$$c_p(T_p)\frac{dT_p}{dt} = -G_{ep}(T_p - T_e) - G_{sp}(T_p - T_s)$$

Where, c_e, c_s, and c_p are the specific heat of electron, spin and lattice, respectively. P(t) is the laser power. The laser power is usually defined by Gaussian function: $e^{-(t/tG)2}$, where t_G is the laser pulse length. T_e, T_s, and T_p are their respective temperatures. The effective temperature of each system can be different due to different specific heat values. For instance, electronic specific heat is very small compared to the lattice. This leads to the sharp rise in electronic temperature by few thousand of K within first 10-100 fs after excitation, while lattice remains cold even after equilibrium.

The temperature profile in Figure 2.4(b) shows the thermal equilibration of three systems (taken from [58]). This model provides a descriptive picture of the energy transfer and equilibration right after the laser excitation. However, major drawback of this model is that it's not including microscopic processes as the conservation of angular momentum.

2.2.3 Microscopic mechanisms

As mentioned in previous section, 3TM model lacks the conservation of angular momentum. During demagnetization, some part of angular momentum must be taken away from the spin system. Therefore, to understand the possible mechanism for ultrafast demagnetization dynamics under consideration of angular momentum conservation, several local and non-local microscopic mechanism have been proposed by several groups.

2.2.3.1 The microscopic 3TM (m3TM) model

Koopmans et al. [20] proposed a model known as microscopic three temperature model (m3TM). This model is based on Elliot Yafet-like spin flip scattering. This model links the demagnetization rate with the microscopic spin-flip process. The Elliot-Yafet type scattering is based on the interaction of an electron with phonon, that can induce a spin flip with a spin-flip probability a_{sf}. This model also classified the magnetization dynamics in two categories: Type I and Type II based on following Figure of merit, T_C/μ_B, T_C is the Curie temperature and μ is the atomic magnetic moment. They explained the transition from type I to type II by the dependence on the magnetic properties.

2.2.3.2 Other scattering mechanisms

Other mechanisms have been proposed, such as spin-flip electron-electron Coulomb scattering [31], laser-induced spin flip 7,9], electron-magnon scattering [29], and recently heat conserving model [59].

2.2.3.3 Super diffusive spin transport

The m3TM model considers the transfer of angular momentum from spin to phonon system via spin-flip scattering event. By intriguing the work of Malinowski et al. [3], in which they observed experimentally the transfer of spin angular momentum in a multilayer structure, Battiato et al. [32] proposed the superdiffusive spin transport model, based on the transfer of angular momentum without spin flipping.

As explained in section 2.2.1, upon laser excitation, hot electrons diffuse deeper into the bulk with the velocity in the range from ballistic to diffusive. This model utilized the spin dependent transport properties of excited

electrons. In magnetic materials, majority electrons have larger mean free path than minority electrons. This leads to flow of majority electrons away from the magnetic layer to the adjacent layer or substrate, and results in the reduction in magnetization. This model successfully reproduced the ultrafast demagnetization dynamics in Ni grown on metallic substrate [60]. We note that in Beaurepaire's work the Ni film was grown on glass, what did not prevent the observation of the ultrafast dynamics in Ni [19].

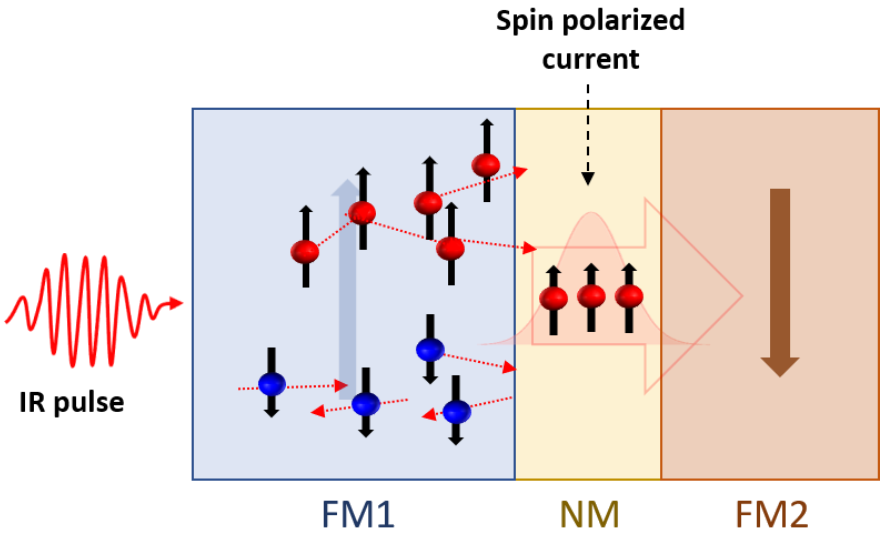

Figure 2.5: Schematic of laser induced ultrafast spin current generation based on superdiffusive spin transport model [32] and propagation through spin valve type multilayer structure.

Later, different experiments evidenced the presence of nonequilibrium spin current [4–6,33,61–64]. Figure 2.5 shows the schematic illustration of a super - diffusive spin current transport in a ferromagnetic multilayer structure used in different studies [3,6,61]. This ultrafast spin current does not only cause the demagnetization but also manipulates the magnetization of adjacent magnetic layers by spin transfer torque [5,34] and generates THz spin current pulses [65].

2.3 Spin current and its utilization for magnetization manipulation

The importance of spin current has already been discussed in the introduction part of this thesis. In this section, the important fundamentals of spin current, i.e., generation, transport and its detection will be discussed. Spin current can be understood as the flow of electron current in a conducting material with all spins in one direction. In general, spin current can be created by passing the unpolarized electrons through a magnetic material, as depicted in Figure 2.6. Upon crossing the magnetic layers, electrons spin is polarized in

the direction of magnetization of magnetic layer. The polarization depends on the density of states at the Fermi level as well as on the sd scattering [66].

The spin dependent scattering of conduction electrons is the key mechanism for spin polarization. According to Stoner model [28], d band of ferromagnetic materials, Fe, Co and Ni divided into two d bands due to exchange interaction. The states which contain more electrons shift lower to the Fermi level, called majority spin state, and empty states, so called minority spin states shifts to the higher level. This leads to more empty state of minority character above Fermi.

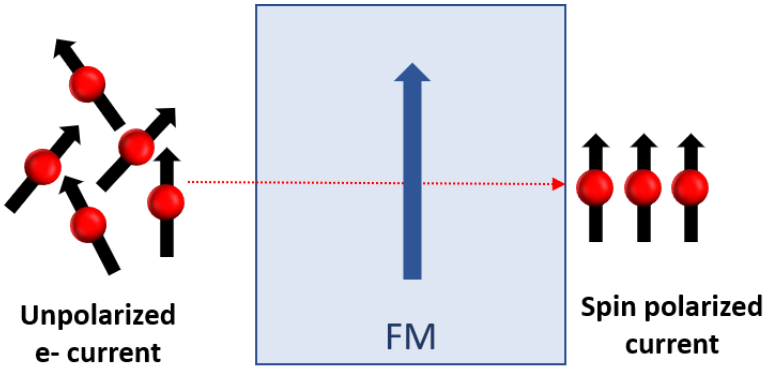

Figure 2.6: Schematic of spin polarized current generation: the unpolarized current stream through a magnetic layer and leaving with the spins align in the direction of the magnetization of ferromagnetic layer.

Therefore, itinerant minority electrons have high probability to scatter in minority bands. Due to spin dependent scattering probability, electrons with spins parallel to majority band experience less scattering and show higher probability to be transmitted through the ferromagnets. However, antiparallel spins experience the high resistance and are reflected at the interfaces. This effect is known as spin filtering effect.

If the spin polarized current density is above certain threshold, it can exert the torque and even switch the magnetization, and this effect is called the spin transfer torque (STT). The schematic of STT based sample device, so called spin valve structure is shown in Figure 2.7.

In spin valve structure, first magnetic layer is used as a spin polarizer, called fixed layer, and second one is used as a detector. These DC current operated STT devices can be fast upto few hundreds of picoseconds. Very recently, Renesas developed the fastest MRAM based on STT with read access time of 4.2 ns [67]. In contrast to conventional current based STT devices, the laser pulses can generate the spin current in femtosecond-picosecond range.

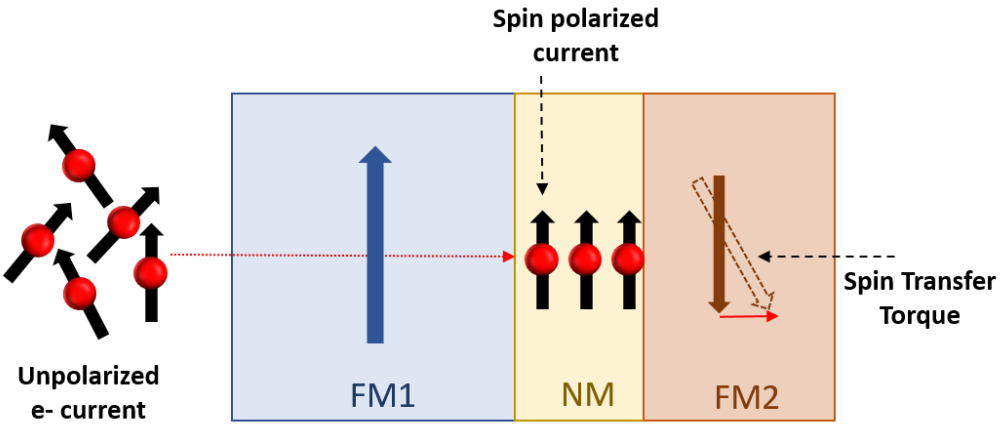

Figure 2.7: Schematic illustration of spin transfer torque (STT) effect in a spin valve structure. The thicker FM1 acts as a polarizer, to polarize the incoming unpolarized electron current. The second FM2 is a detection layer or free layer, which can rotate or even switch depending on the current density of incoming polarized current. Both the magnetic layers are magnetically separated by a non-magnetic (NM) spacer layer [66].

Malinowski et al, first utilized the spin valve structure to study the ultrafast demagnetization dynamics [3]. Surprisingly they observed the different dynamics, when both layers were parallel and antiparallel. This difference in dynamics was attributed to the spin transfer of laser excited hot electrons between both magnetic layers. Battiato et al. [32] explained this behavior by their superdiffusive spin transport model. Until now, Different studies have been shown the magnetization manipulation by ultrafast spin-transfer torque either by ballistic non-thermal or diffusive thermal hot electrons [5,34,36]. Laser excitation also generates a thermal gradient across the magnetic layer during the thermalization of hot electrons. Electrons spins experience different conductivities, due to this thermal gradient and results in the spin current generation, this effect is known as spin dependent Seebeck effect (SDSE) [68]. However, this effect is dominant at longer time scale, and therefore it's possible to distinguish the contribution of spin current generated from SDSE and ultrafast demagnetization [68–70].

Upto this date, such studies have also considered different ferrimagnets including TM-RE alloys [24,41]. However, no spin polarized effects in the HE induced demagnetization have been yet studied in 4f RE and TM-RE alloys. This is one of the motivations of my thesis work, which focuses on describing spin polarized current induced ultrafast demagnetization with element selectivity in RE-TM ferrimagnets, important materials in order to push spintronics and magnetic data storages towards the sub-picosecond regime.

2.4 Ferrimagnetic Rare-earth (RE) and transition metal (TM) alloy systems

Constant demand of increasing the speed and density of magnetic memories required not only research for the techniques but also materials, which can be an alternative for conventional ferromagnets (Fe, Ni and Co). Antiferromagnetic materials represent the ideal characteristics from technological point of view; higher working frequency (THz range), zero magnetization add the benefit of smaller stray field which can be useful for reducing the size of magnetic bits and improving density. However due to zero net magnetization, it's very difficult to use the antiferromagnetic materials as an active component in spintronic devices [8].

Ferrimagnets are the type of magnetic materials consisting of uncompensated antiparallelly coupled sublattices, which results in a finite non-zero magnetic moment, shown in Figure 2.8 (a). These materials form a bridge between ferro and antiferro – magnetic materials.

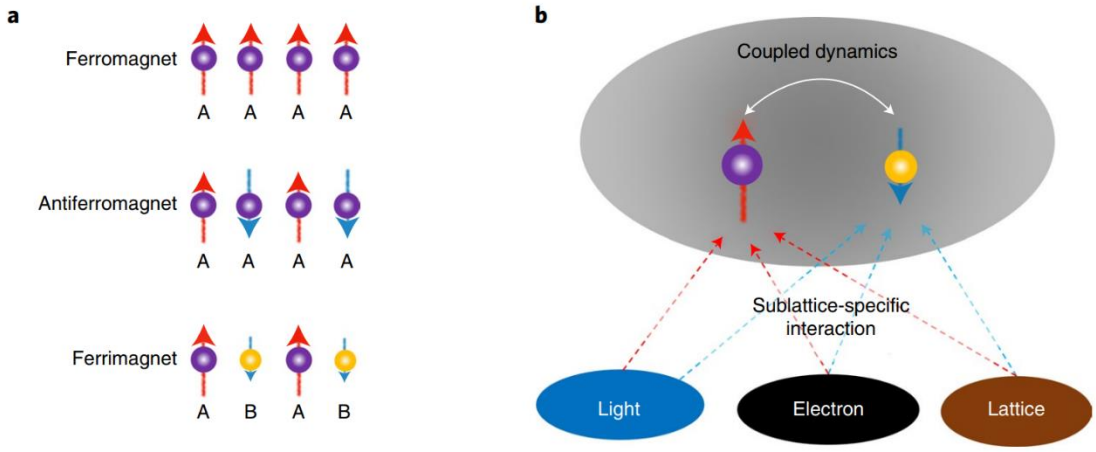

Figure 2.8 (a) Three different types of magnetic materials: Ferromagnets, Antiferromagnets, which consist of one type of atoms, and ferrimagnets, consist of two (can have more than two) atoms with inequivalent magnetic moments. (b) Schematic diagram of a coupled dynamics of two antiferromagnetic sublattices and their interactions with light, an electrons and lattice. (Figure and caption are taken from [8]).

Ferrimagnets have two main properties, which make them suitable candidate; first, antiferromagnetic coupling of sublattices allows to probe the antiferro - magnetic spin dynamics, and transport. Second, ferrimagnetic materials, such as are-earth (RE)- transition metals (TM) composed of inequivalent magnetic sublattices; TM (Fe, Co and Ni) and RE elements (Gd, Tb and Dy etc) that have distinct electronic, magnetic and optical properties and offer sublattice control and study the coupled dynamics of sublattices (shown in Fig. 2.8 b).

The magnetic properties of these alloys can be tuned by varying the chemical composition and temperature [8,9]. Such alloys also show the zero-net magnetization at certain temperature, known as magnetic compensation point (T_M). Although the net magnetization is compensated, but both sublattices remain unequal, resulting in different density of states (DOS) for the two subbands. This allows to detect the magnetic state of ferrimagnets with the same electrical and optical methods as ferromagnets. Additionally, non- zero DOS at Fermi level and net magnetization results in finite Zeeman coupling as well as spin polarization [8,9].

In this thesis, RE-TM alloys are used for detecting the spin polarized hot electron current via their impact on the magnetization of the alloy in the picosecond time scale. I have used FeGd and CoGd alloys to detect the RE 4f and the TM 3d sublattices. I will briefly introduce some key features of the RE-TM metals electronic band structures, responsible for their distinct properties.

Fe, Co and Ni are the conventional ferromagnetic materials, which possess spontaneous magnetization due to incomplete 3d electronic band. The spatial overlap of 3d band between neighboring atoms results in the strong direct 3d-3d exchange coupling (Figure 2.9 a). This direct coupling is responsible for high magnetic ordering temperature, so called Curie temperature (T_C).

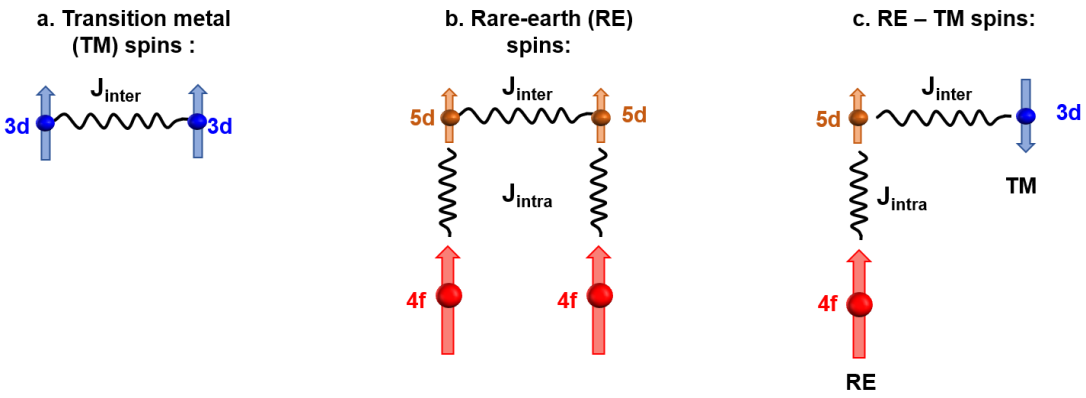

Figure 2.9: Different spin coupling responsible for long range magnetic ordering in (a) 3d transition metals (TM), (b) Rare-earth (RE) metals and (c) RE-TM alloy systems, Figure is adopted from [71].

In case of rare-earth metals (Gd, Dy and Tb), mainly localized 4f (7 μ_B for Gd) spins are responsible for magnetization and 5d moments contribution is extremely small (0.63 μ_B in case of Gd). Due to their localized band, 4f doesn't overlap with the neighboring atoms. Though, 4f moments of neighboring atoms interact through intra-atomic 4f-5d and inter-atomic 5d-5d coupling (shown in Fig. 2.9 b). Such type of indirect coupling is called RKKY type coupling [28].

The absence of direct coupling between 4f spin explains the lower T_C values for RE metals.

In RE-TM alloy system, RE metals have almost half-filled f orbitals, and TM metals have more than half filled d shells. Therefore, 5d states are above Fermi level while TM 3d states are below E_F. So, 5d majority spin bands hybridizes with the 3d minority bands, and leads to antiferromagnetic coupling through inter-atomic 3d- 5d exchange coupling between both sublattices. The localized RE 4f spins band, which lies far below Fermi level [72], couples parallel with the 5d moment of same atom through intra-atomic exchange 5d-4f coupling (Fig. 2.9 c).

The variation of magnetization with temperature is shown in Figure 2.10 for RE-TM systems (taken from thesis [56]). At low temperature, magnetization is dominant by RE sublattices and at high temperature dominant by TM sublattice. This distinct behavior arises due to the fact that both sublattices shows the different temperature dependence of magnetization, but have same Curie temperature (T_C). Since, both sublattices show the different temperature dependence of magnetization, RE magnetization decreases faster than the TM on increasing temperature. This different variation originates an intermediate temperature at which both sublattices are equal and opposite, and results in the net zero magnetization. This point is known as magnetic compensation point (T_M).

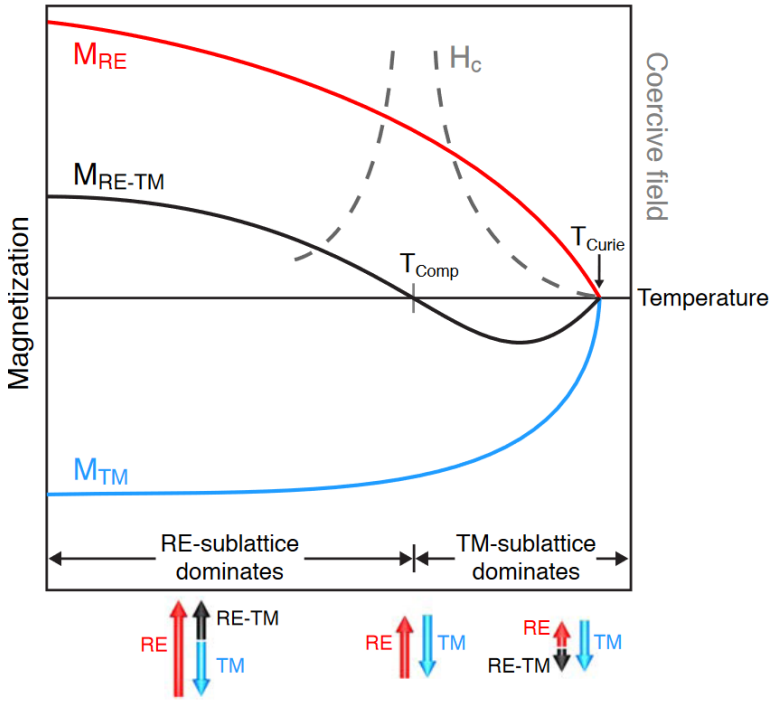

Figure 2.10: Temperature dependent magnetization of RE (red) and TM (blue) in RE-TM alloys, Figure is taken from [56].

Due to this unique features, unequal antiparallel coupled sublattices, GdFeCo ferrimagnets showed all-optical switching by femtosecond laser pulse [26,27,42,73,74].

As I mentioned at the end of the section 2.3, the motivation of studying the ultrafast spin current induced dynamics of 3d and 4f magnetic moments in ferrimagnetic RE-TM alloy. Such measurements can be possible using experimental techniques, which allows to measure the dynamics core level localized electrons. This cannot achieve using lab-based optical pump-probe methods, where energies are limited to valence band (1-3 eV) or high-harmonic generation sources (~ 1000 eV). Therefore, in this work, various element-selective measurements were performed using X-ray sources from different large-scale facilities. In the next section, I will discuss about the fundamentals of light matter interactions and different processes happens when light interact with the matter.

2.5 Light-matter interaction

When light pass through material, many phenomena takes place, among them absorption, transmission, reflection and scattering are main interactions between matter and light. Based on the energy or wavelength of incident light, electronic, magnetic and structural properties can be probed. Figure 2.11 shows the summary of different processes, takes place on interacting an electro-magnetic light within range from visible to X-rays energies.

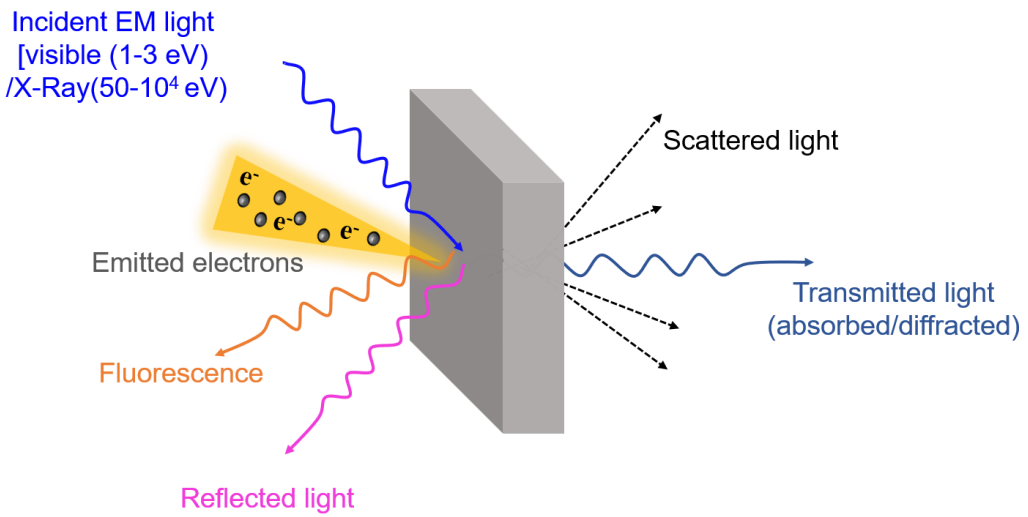

Figure 2.11: Schematic illustration of interaction of light with matter, and various phenomena occurs when light is absorbed or pass through material.

In this thesis, I mainly used two type of incident light: first – continuous laser in visible range and second soft X-rays from different synchrotron sources

and mainly, I probed the reflected intensity, transmitted intensity in absorption, and emitted photoelectrons coming out during photoemission process. All these interactions will be discussed in brief in next sections.

2.5.1 Magneto-optic effects

Light is an electromagnetic wave, when passing through the magnetic media, its polarization gets affected. It was first discovered by Faraday in 1845 in transmission geometry [75]. About 30 year, after the discovery of Faraday effect, Kerr observed the same phenomena in reflection [76], and known as Magneto Optic Kerr Effect (MOKE). Until the availability of tunable radiation in X-ray regime with polarization, magneto-optic experiments were limited to conventional optics. However, development in synchrotron sources allowed to observe the Faraday and MOKE in X-ray regime in absorption, scattering, circular and linear dichroism in core level as well as valance band photoemission, etc. (all references related to this are in ref. [77]).

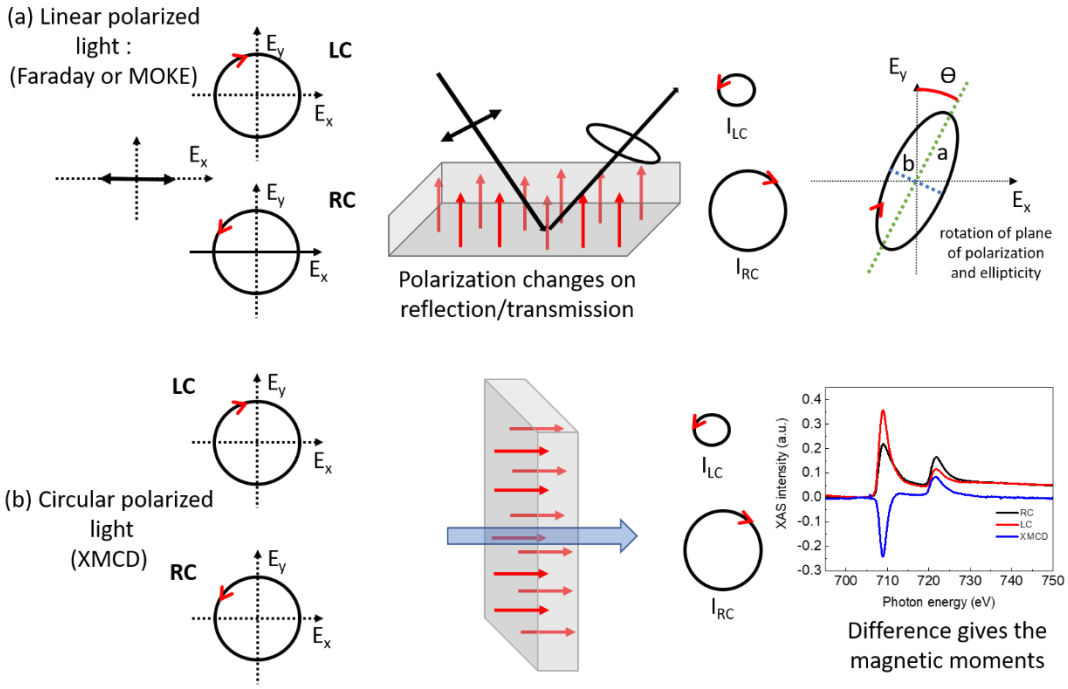

Figure 2.12: Schematic of magneto-optic effect using (a) Linear polarized light origin of Faraday or MOKE effect, (b) Circular polarized light – for XMCD.

The magneto-optic Faraday (or MOKE) can be understood by considering the linearly polarized light as a combination of right and left circular polarized component [28], as shown in Figure 2.12 (a). Upon passing (or reflecting) through magnetic media, one component of circular light is absorbed preferentially and results in change and polarization. Figure 2.12 shows the schematic representation of two magneto-optic phenomena: first

one, using linear polarized light (MOKE or Faraday) and second, using circular polarized light (XMCD) (to be discussed in section 2.5.2).

In the classical picture, the optical effects can be described in terms of refractive index. This refractive index depends on the frequency and the polarization of the EM wave. For a material, particularly near resonant frequencies, refractive index can be written as [28]:

$$n(\omega) = 1 - \delta(\omega) + i\,\beta(\omega)$$

The real part δ(ω) and the imaginary part β(ω) correspond to the refraction and the absorption of EM wave in the medium, respectively.

The polarization dependence on the absorptive part β(ω) is called as "dichroism". This term originates from the word, "dichroic", i.e., two colors. This effect comes due to the different absorption of polarized light.

According to quantum mechanical picture, the interaction of polarized photons can be expressed in the form of scattering factors. However, all the formalisms are well defined in the text books, therefore, I will not go into its detail [28]. The next section will continue the absorption.

2.5.2 X-ray absorption (XAS) and X-ray magnetic circular dichroism (XMCD)

When X-ray interact with the matter, X-ray photons can be absorbed or scattered. The electronic system gains the part of the energy upon absorbing the X-ray photon and transfer to the electrons.

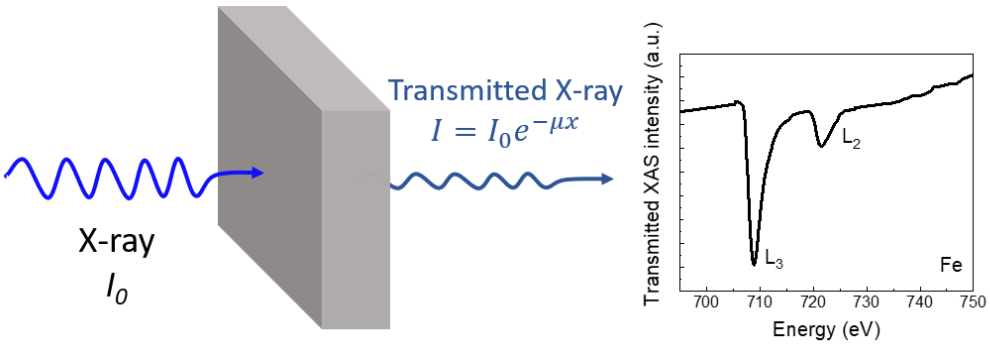

Figure 2.13: Principle of XAS: X-ray intensity attenuates exponentially upon transmitting though a material. Graph in right is an example of the absorption spectra measured in transmission mode for a thin Fe film. At the Fe core level resonance edges, L_2 and L_3 edges, the X-ray intensity drops due to resonant absorption of the X rays.

The resultant X-ray intensity attenuates on passing the materials, and the X-ray absorption intensity is given by Beer's law:

$$I(z) = I_0\, e^{-\mu z}$$

Where, μ is the absorption coefficient and I_0 is the intensity of incoming X-rays. When an EM wave enters into a medium with refractive index as explained above and with linear absorption coefficient μ. The electric field inside the material can be written as:

$$E = e^{inkz} = e^{ikz}e^{-i\delta kz}e^{-\beta kz}$$

In above equation, first term corresponds to the incident amplitude, second term $e^{-i\delta kz}$ is responsible for phase shift and $e^{-\beta kz}$ cause the attenuation of X-ray field.

Figure 2.13 shows the schematic of X-ray absorption principle and the XAS spectra measured in transmission geometry for Fe. On tuning the X-ray energies equal to the electronic core level transition, i.e., at resonance, a core shell electron excites to valence state and results in the change in X-ray intensities. Since, the core level transitions are element specific, therefore by measuring the absorption spectra at resonance provides many valuable informations. X-ray can measure the element specific properties by tuning the energies at their respective edges. Large probing depth provides the access to study deeply buried magnetic layers, most importantly, transition from core level to valance band, provides the density of final states.

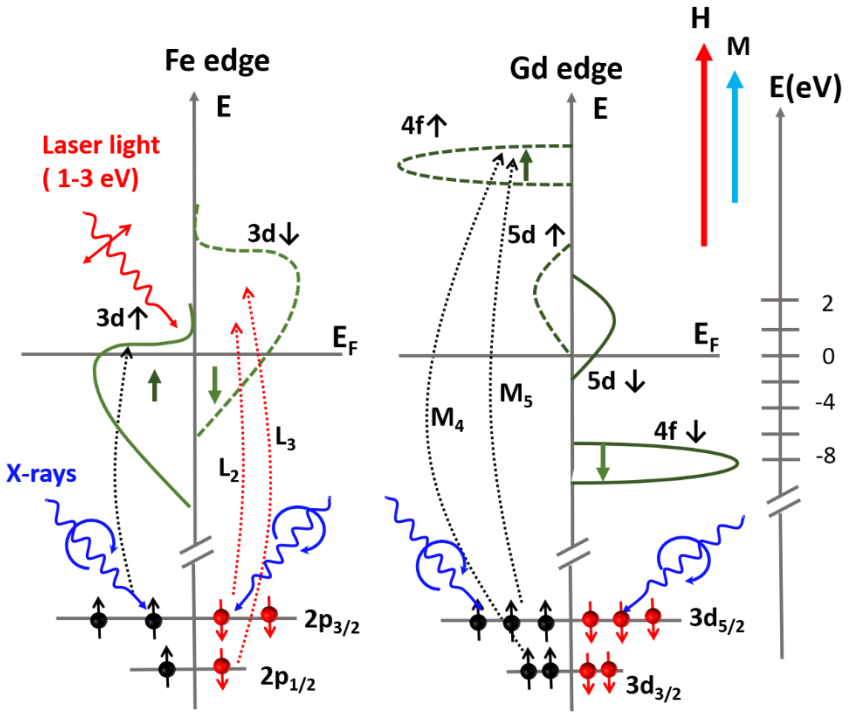

Figure 2.14: Electronic transitions following the selection rules for the dipole transitions for Fe $L_{2,3}$ into the 3d band and for Gd $M_{4,5}$ into the empty states in the 4f band.

According to the Fermi Golden rule, the transition probability for the transition from core level i to final level f can be written as:

$$\sigma_{\text{abs}} \propto \sum_f \left|\langle \phi_f | \boldsymbol{e_q}.\boldsymbol{r} | \phi_i \rangle\right|^2 \rho_f(\hbar\omega - E_i)$$

Where, e_q is light polarization vector and r is the electron position. ρ_F is density of states above Fermi level. The selection rules for the dipole transitions can be written as:

$$\Delta l = \pm 1, \qquad \Delta m_l = \begin{cases} 0\ (linear\ polarization) \\ \pm 1\ (circular\ polarization) \end{cases}, \qquad \Delta s = 0$$

Where, m_l is the magnetic orbital quantum number and ± 1 is used of X-ray helicities. As shown in the above equation, the transition probability not only depends on the initial state but also on the final state.

In magnetic materials, the available density of states is different for majority and minority spins, and according to the selection rule, results in the different absorption for the left or right circular polarized light.

Figure 2.14 shows schematic illustration of the core level transitions:

- $2p_{3/2} \rightarrow 3d$ (L_3) and $2p_{1/2} \rightarrow 3d$ (L_2) edge for TM (Fe, Co and Ni)
- $3d_{5/2} \rightarrow 4f$ (M_5) and $3d_{3/2} \rightarrow 4f$ (M_4) edge for RE (Gd, Dy and Tb)

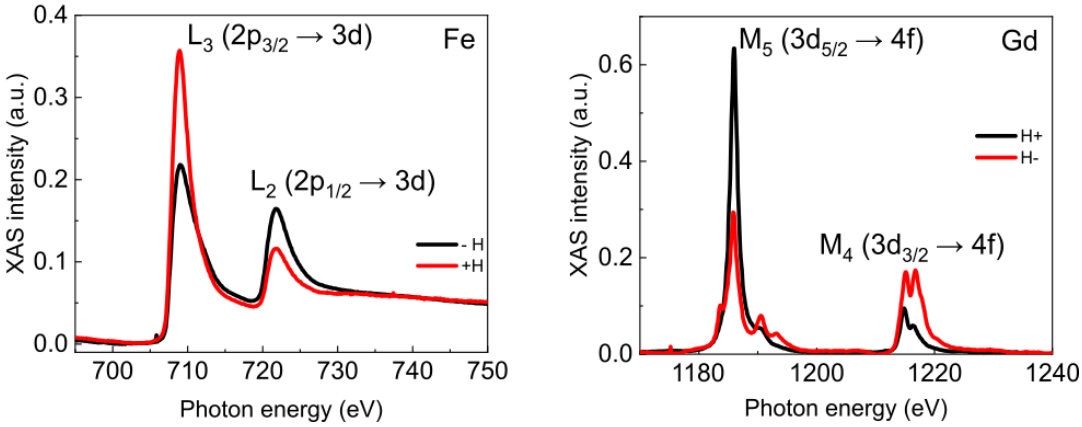

Figure 2.15: XAS spectra measured at Fe $L_{2,3}$ and Gd $M_{4,5}$ edge in FeGd alloy.

This effect can be observed by changing the direction of magnetization with the fixed circular polarization of X-rays. In this work, we measured the XMCD using this configuration. The difference of both XAS curve for two opposite magnetic field gives the XMCD and its directly proportional to the magnetization of the materials.

$$\Delta\mu = \mu_+ - \mu_- \propto M$$

Where, μ- and μ+ are the absorption intensity on applying -H and +H magnetic field. The XMCD contrast arises due two different absorption cross

sections of circularly polarized light. When photon spin and photoelectron spin are parallel, we observe the maximum absorption, and if both are antiparallel, then we get minimum absorption. This transition probability depends upon the number of states available above the Fermi level.

The XMCD effect can be explained by a two-step model [28]. In the first step, circular polarized light carries an angular momentum. Upon exciting a photo electron, it can transfer its angular momentum to the excited electron for angular momentum conservation. This transfer of angular momentum depends on the spin orbit level splitting. In case of TM L edge transitions, i.e., $2p_{3/2}$ (L3) and $2p_{1/2}$ (L_2) has opposite spin orbit coupling (L+S, L-S, respectively). Therefore, when the photon spin and photoelectron spin is parallel or antiparallel, it leads to different absorption. In the second step, exchanged split 3d valence shell acts as detector for the excited photoelectrons. One example of measured spectra for Fe and Gd for two opposite magnetic field ± H is shown in Figure 2.15. One of the important application of XMCD lies in the resolving the spin and orbital moment calculation by using sum rule calculations [78,79].

Chapter 3 Experimental techniques

In this chapter, I will provide a brief overview of the experimental methods Two main techniques were utilized to investigate the static magnetic properties: Magneto-optic Kerr magnetometry (MOKE) experimental set-up at IPCMS and element selective X-ray magnetic circular dichroism spectroscopy at PM3 beamline, BESSY II, results discussed in Chapter 4. Ultrafast magnetization dynamics were studied using Time-resolved XMCD experimental set-up at FemtoSpeX beamline at BESSYII, Berlin, results discussed in Chapter 5 and Chapter 6. Additionally, X-ray photoemission spectroscopy (XPS) at TEMPO beamline, SOLEIL synchrotron in Paris, was used to examine the alloy inhomogeneity on the surface of thin film, as detailed in Chapter 6.

3.1 Experimental set-ups

Since my work aims at investigating the ultrafast spin dynamics in multi-lattices ferrimagnets, I used element-selective TR-XMCD set-up on the FemtoSpex beamline at BESSYII, Berlin. However, due to the limited access to the beamline and the time-consuming data acquisition, these measurements require an extensive preparation to optimize the beamtimes. Especially, I dedicated a significant part of my work to characterize the static magnetic, electronic and structural properties of my samples to identify the best candidate for pump-probe experiments. In the next paragraph, I will describe the specifications of the experimental set-ups used to perform the characterization of static properties and the measurements of spin dynamics.

3.1.1 Static characterization

3.1.1.1 Magneto-optic Kerr magnetometry

Magneto Optical Kerr Effect is a table-top experiment which allows characterizing the magnetic properties of thin films, including magnetic anisotropy, coercive field, and exchange coupling. In this technique, the deviation of light's polarization is measured after reflecting from the surface of a magnetic sample. Indeed, it is well known that a magnetic media induces a rotation of the polarization axis as well as a modification of the ellipticity. These changes are proportional to the magnetization of the magnetic materials.

There are three types of MOKE geometries, that depend on the orientation of the magnetization and the plane of incidence of the incoming light as shown in Figure 3.1.

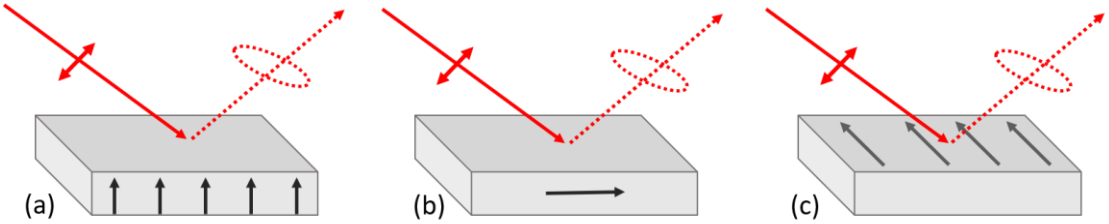

Figure 3.1: MOKE experimental geometries: (a) Polar, (b) Longitudinal, and (c) Transversal MOKE. Black solid arrows represent the magnetization direction and red arrow shows the propagation of laser beam.

(a) Polar MOKE, where the magnetization lies out of plane to sample and parallel with the plane of incidence (b) Longitudinal MOKE, with the magnetization is in plane and in the plane of incidence, (c) Transversal MOKE, the magnetization is in-plane to the same surface and orthogonal to the plane of incidence.

We used the MOKE magnetometry in polar and longitudinal geometries to measure the hysteresis loops of samples with out-of-plane and in-plane magnetic anisotropy axis, respectively. The scheme of the experimental MOKE set-up at room temperature (a) and low temperature with UHV experimental chamber (b) at IPCMS is shown in Figure 3.2.

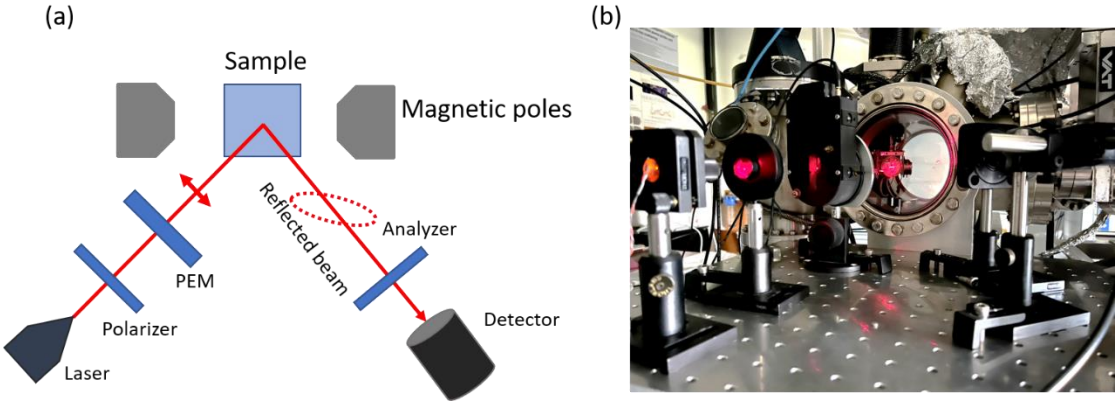

Figure 3.2: Schematic (a) and set-up picture (b) of MOKE magnetometry set-up in longitudinal geometry with the optical elements.

The setup is composed of a continuous laser beam (~632 nm) which passes through a polarizer to obtain high degree of linear polarization for the beam. A photoelastic modulator (PEM) allows to modulate the signal at 50 kHz for synchronous detection using a lock-in amplifier. The beam impinges the

magnetic sample at an angle of 45° and it is reflected. The magnetization of the sample is controlled by applying an external magnetic field. After reflection on the sample, the beam passes through the analyzer (which is a second polarizer), whose axis is tilted by 90° with respect to first polarizer. This crossed configuration for both polarizers allows for reaching the almost total extinction of the signal on the photodetector. As the magnetic field will modify the orientation of the sample's magnetization, a slight modification of the polarization will be seen as a change in the transmitted light and detected by the lock-in. The magnetic properties of my samples are determined by recording hysteresis loops which are recorded by sweeping the magnetic field using an electromagnet.

As shown in Figure 3.2, I have used two sample environments during my set-up, namely the "ex-situ" and "in-situ" environments. In the first one, the sample is mounted "ex-situ" on the optical table which allows fast acquisitions. Experiment can be performed PMOKE or LMOKE geometry by rotating the magnetic coil or angle of incidence. Additionally, the sample can be rotated in order to identify easy and hard magnetic anisotropy axis. The drawbacks reside in the weak amplitude of the magnetic field and experiments are carried out at room temperature. In the second set-up, the sample is under UHV condition which allows decreasing the temperature upto 170 K. Two magnetic coils are available to apply in-plane (up to 25 mT) or out of plane (up to 50 mT) magnetic fields. However, the geometry of the UHV chamber restrict the sample rotation during measurement.

In the context of my thesis, MOKE magnetometry offers a very efficient and versatile solution to obtain most of the magnetic properties of the magnetic layers such coercive fields, magnetic anisotropy axis or magnetic decoupling of magnetic layers. These parameters are of essential to prepare the pump-probe measurements. However, this technique is sensitive to the electrons in the conduction band at the vicinity of Fermi level. In case of RE-TM alloys, it will then be mainly sensitive to the TM 3d electrons whose magneto-optical response is order of magnitude larger than that of the RE 5d [80,81]. Furthermore, in case of TM alloys or multilayers, MOKE gives an averaged magnetization since it is not element-selective. Therefore, complementary element-selective X-ray Magnetic Circular Dichroism spectroscopy is needed to fulfill the sample characterization, especially to obtain the amplitude of XMCD signal.

3.1.1.2 XMCD at large scale facility

Besides Hc and anisotropy axis, the other requested parameters are the amplitude of XMCD signal at the RE M_5 and TM L_3 edges and their temperature dependence which cannot be assessed from MOKE measurements. Therefore, we have performed X-ray Absorption Spectroscopy in transmission mode (Fig. 3.3) within the ALICE chamber, located at the PM3 beamline in BESSYII [82]

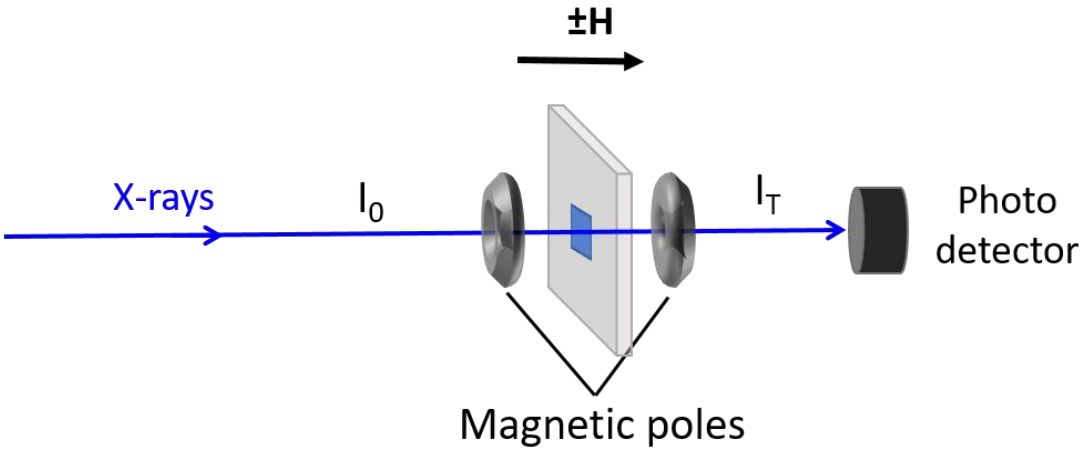

Figure 3.3: Experimental geometry for the X-ray absorption spectroscopy (XAS) in transmission mode. Electromagnets provide the alternating magnetic field to measure the magnetic contrast. Transmitted signal is then measured by an avalanche photodetector.

The ALICE chamber provides a sample holder under UHV and equipped with a cryostat which enabling temperature control down to 80 K using liquid Nitrogen (LN2) under a vacuum of 10^{-8} mbar. In lab-based low temperature MOKE setup, temperature can be reached upto 170 K, this limits the probing magnetic properties below 170K. A magnetic field of 0.7 T can be applied in any direction of the incidence plane which allows saturating samples with in-plane or out of plane magnetic anisotropy. The XAS measurements are performed by using variable polarized light (circular or linear) with the energy resolution ($E/\Delta E$) of 32000 at 64 eV and an optimum photon flux of 10^9 – 10^{10} ph/sec. The X-ray energy range spans from 20 eV to 1900 eV, covering the resonance edges of most of the ferromagnetic transition metals Fe, Co, Ni ($L_{2,3}$) and Rare-earth metals Gd, Tb, Dy ($M_{4,5}$).

The XAS spectrum is obtained by sweeping the photon energy and recording the dependence of the transmitted X-ray intensity on the photon energy via a photodetector. The XMCD spectrum is then obtained by subtracting XAS spectra obtained for two opposite orientations of the external

magnetic field (one example of measured spectra at Fe $L_{2,3}$ and Gd $M_{4,5}$ edges for FeGd alloy is shown in Figure 2.15)

The sample holder allows mounting 3 samples at a time while it takes only 2 to 3 hours to introduce new samples. Therefore, these specifications allow to measure a lot of samples within a week beamtime.

3.1.1.3 XPS at synchrotron SOLEIL

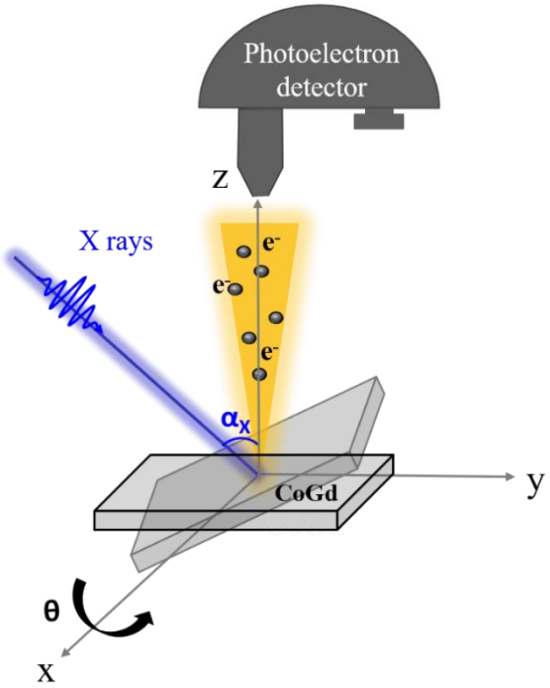

Figure 3.4 XPS Experimental geometry with photoelectron detector. a_x = 44° is the angle between incident X-ray and the detector. θ represents the emission angle of the photoelectrons and is obtained by a rotation around the x axis, as illustrated by rotated plane. At θ=0 the surface normal is aligned with the entrance of analyzer.

The ultrahigh vacuum (UHV) Photoemission station at the TEMPO beamline is designed to perform the static and time resolved studies of surface sensitive electronic and magnetic properties using photoelectron spectroscopy. X-Ray photon energy can be varied from 50 – 1500 eV with the energy resolution (E/ΔE) more than 10,000. The main experiment chamber is equipped with the Scienta SES 2002 hemispherical photoelectron analyzer and an adjacent preparation chamber with a sample transfer system, Ar^- sputtering gun to clean the surface before performing XPS. The sample temperature can be changed between 80 – 350 K at the pressure of 10^{-10} mbar. A horseshoe-shaped electromagnet can generate a constant in-plane magnetic field of magnitude 10 mT to measure the dichroism in photoemission mode. Figure 3.4 shows the experimental setup used for measuring the photoemission spectra

for CoGd alloy systems (Section 6.2). The sample's normal was aligned with the entrance of the photoelectron analyzer while the X-ray beam impinged the samples at an angle of $\alpha_X = 44°$ in respect with the sample's normal.

3.1.2 Time-Resolved XMCD (TR-XMCD)

3.1.2.1 Sources of ultrashort X-ray pulses

In section 3.1.1.2, I have described the advantage of XMCD spectroscopy in characterizing the magnetic properties of thin layers. TR-XMCD using soft X-ray pulses offers the similar advantages with the possibility to investigate the characteristic of spin dynamics and unique possibility to study the spin dynamics of core level 4f electrons in Rare-earth elements, which is not accessible using Tr-MOKE set-ups. Therefore, to investigate the SPHE induced demagnetization in FeGd alloys, I utilized circularly polarized soft X-ray pulses with 100 fs pulse duration. These pulses can be found at large scale facilities or table-top HHG sources.

The generation of ultrashort pulses in X-ray regime is not only limited to synchrotrons. In the past few years, there have been many developments in different sources for generating ultrashort pulses of duration 10-100 fs. Among them, the most exciting advances are the emergence of X-ray free-electron lasers (XFELs), which generates coherent, high brilliance photons with photon flux 10^{25} ph/sec compare to synchrotron sources 10^{10} - 10^{15} ph/sec. However, absence of circular polarization restricts to measure the XMCD.

Apart from large scale facilities, table-top high harmonic generation (HHG) sources provides an alternative to XFEL, which are able to generate pulses even upto attosecond durations in extreme ultraviolet (XUV) to soft X-ray range, but complicated for circular polarization.

Despite of very short pulses and high brilliance sources, limitation of suitable energy range and light polarization doesn't provide optimum experimental conditions to perform Tr-XMCD until now.

The synchrotron sources generate soft X-ray pulses whose duration is about 100 ps. They can be compressed down to 10 ps in the low-alpha operation mode [83,84]. In first approximation, the pulse duration is given by the "size" of the electron bunches in the storage ring used to generate the X-ray pulses. However, because of the stability of the electron bunch in the storage ring, the reduction has a natural limit around 5-7 ps. Therefore, a further reduction of X-ray pulses duration down to 100 fs request another technique, the so-called femtoslicing (fs-slicing) operation mode. I will describe it in the next paragraph along with the experimental set-up.

3.1.2.2 TR-XMCD at the "fs-slicing" operation mode

Development of short X-ray pulses (100 fs) at synchrotron provided the access of magnetization dynamics of core level electrons such as 3d TM, 4f RE electrons. However, these pulses cannot be used to study the dynamics at femtosecond timescale.

A method to generate ultrashort circularly polarized soft X-ray pulses at synchrotron is the fs-slicing method, first proposed by Zholents and Zolotorevand demonstrated at the Advanced Light Source (ALS) in Berkley, USA [85]. The principle of fs-slicing is to utilize the fs laser pulse to modulate the energy of electron bunch and these modulated electron bunches thus can generate the short pulses of X-rays. Since, these resultant X-ray pulses generates from a small part of an electron bunch so it cost the loss of significant decrease in photon intensity by order of 10^5 compare to normal ps-X ray (hybrid mode) pulses. As a consequence, it provides limited photon flux around 10^6 ph/sec. Therefore, depending on the type of experiments, sample thickness and XMCD value, it takes several days to acquire enough statistics on the data.

However, despite the limited photon flux, fs-slicing facility at BESSYII is the unique X-ray base experiment set-up, which provides the ultrashort pulses of ~100 fs resolution in soft X-ray range with circular polarization [86]. This allows to measure the transient magnetization dynamics of 3d and 4f systems.

The schematic of FemtoSpeX facility at BESSYII is shown in Figure 3.5. The whole beamline set-up is around 50 meters long horizontally.

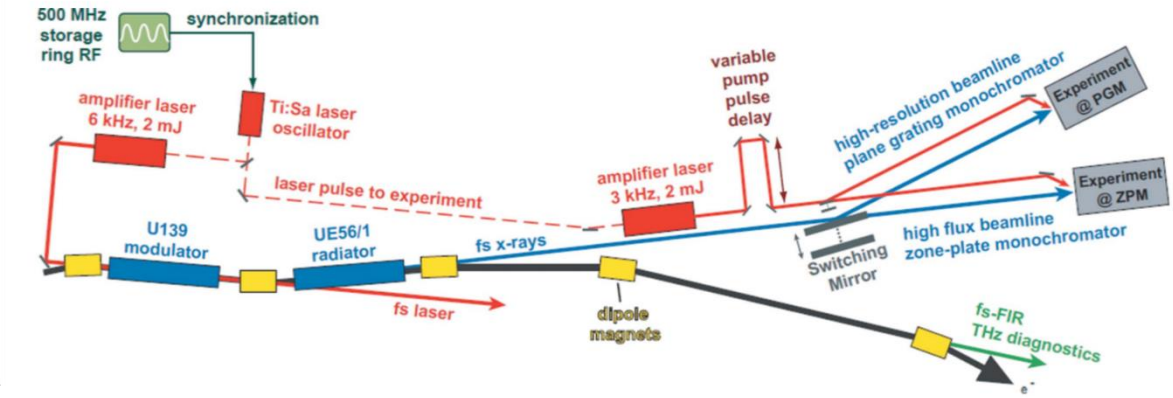

Figure 3.5: Femtoslicing beamline schematic at BESSYII. Single Ti:Sa oscillator is coupled with two amplifiers, one, which run at the 6kHz repetition rate is used to generate fs X-ray pulses and the other at the 3 kHz is used as a pump laser. This repetition rate provides to probe the pumped and unpumped signal in same delay scans. The main oscillator is synchronized with the master clock of the storage ring. Whole setup has 50-meter-long dimension horizontally, Figure taken from [86].

The laser systems consist of two coupled Ti: Sa amplifiers feed by the same oscillator. The first amplifier is used for the femtoslicing operation and operates at 6 kHz repetition rate. The second amplifier is used as the pump source and operates at 3 kHz. Since, both amplifiers are fed with the same oscillator, this scheme provides the natural synchronization and a jitter free pump-probe experiment. The oscillator is further synchronized with the synchrotron storage ring master clock, so that the fs laser pulses always hit the maximum of the electron bunch (~50 ps (FWHM)).

Fs-slicing process

The generation of the fs X-ray pulses takes place in the planar wiggler (U139), called as modulator, a bending dipole magnet and an elliptical undulator (UE156) of APPPLE II type to generate elliptical polarized x-rays. Figure 3.6 shows the working principle of femtoslicing process.

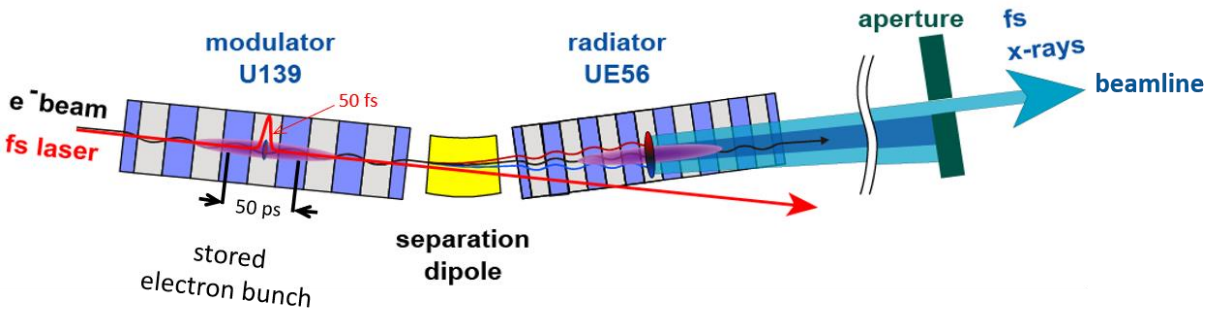

Figure 3.6: The femtoslicing process. A fs IR laser overlaps and co-propagates with the electron bunch in the planar wiggler (U139) marks as modulator, and then separate the path of energy modulated electrons from the main bunch in dipole bending magnet. Later, they emit short-pulses of elliptically polarized synchrotron radiations in the elliptical undulator (UE56) of the APPLE II type. Only fs X-rays allows to pass through the aperture and other radiations are blocked. [Image courtesy – Niko Pontius]

The electron bunch and a fs laser pulse of duration ~50 fs co-propagate in a wiggler which is tuned to resonance, i.e., at the emit undulator radiation at the laser wavelength of 800 nm. The electrons modulated in energy on overlapping with the laser field, either accelerated or decelerated depending on the optical phase. Due to different energies, the modulated electrons and main bunch follows different trajectory in the bending dipole magnets and radiate separately in the radiator. The energy difference is only 1%, which lead to the separation of only 1 mrad. Subsequently, both main (hybrid) of 50 ps duration and 100 fs electron bunches propagates together into an elliptical undulator (or radiator) UE56 of APPLE II type, in which elliptically polarized x-ray pulses generates. Although the femtoslicing produced the 100 fs soft X-ray pulses, it is

at the cost of a dramatic reduction of the photon flux. First, the soft X-ray pulses are generated from 0.1% electron of the bunches which already costs 3 orders of magnitude. Then, the laser – electron interaction requires high intensity (~1 mJ per pulses) fs laser pulses. To reach such intensities, the available technical solution at that time was limited to amplified Ti:Sa lasers as described in Figure 3.5. The frequency of the femtosecond laser is 6 kHz, much lower than the frequency of the synchrotron (380 MHz) which means that only a fraction of the electron bunches is actually sliced. It costs 2 other orders of magnitude in photon flux. This consequence the reduction in the intensity by factor of 10^5. Therefore, it's very important to separate it from background radiation. This separation is achieved by two ways: the first one called femtobump, in which the electron orbit of modulated electron is locally adjusted within the radiator axis, and main electron bunches kick away from the axis. With the use of this setting, it's very easy to switch to the regular mode using 50 ps time resolution or 100 fs sliced X-ray pulses. Another is the utilization of sequence mode [86].

During the slicing process, additional THz radiations are also generated. The modulated 'sliced' electrons create a dip in main electron bunch profile, and it leads to the emission of synchrotron radiation in THz range at a bending dipole magnet downstream of the f-slicing. These THz radiations last in the storage ring upto many turns. Since, these THz generates from the same sliced electrons, hence they provide the diagnostic tool for the temporal and spatial overlap of the laser and electron beam as well as magnitude of modulated electrons energy.

Additionally, a Zone plate monochromator (ZPM) is used to select the photon energy and to focus the X-ray beam on the sample. Using a single optical element for both purposes allow limiting the photon losses in the transmission line. Optics in the ZPM are Reflecting Zone Plates (RZP). ZPM consists of 11 RZPs and each of 11 RZPs of the ZPM is designed for a specific photon energy band and cover an energy range from 410 to 1300 eV. Furthermore, the ZPM displays a moderate energy resolution ($\lambda/\Delta\lambda$ ~ 500 or 2000), but sufficient enough to apply the sum rule analysis [78] by measuring dynamics on $L_{2,3}$ ($M_{4,5}$) edges [87,88].

Experimental end station

I have presented XAS and XMCD spectroscopy in transmission mode on PM3 beamline. The experimental end-statio is so called Dynamax endstation (a scattering chamber equipped with a cryostat) at the fs-slicing beamline, consists of a UHV chamber. The magnetic field is given by a superconducting 3 D vector magnet which allows applying magnetic field up to 1.5 T in all three spatial dimensions. The transmitted X-ray intensity is recorded by an Avalanche Photo Diode (APD) detector. Due to the low X-ray flux, the signal

coming from the APD passes through a preamplifier and an **Aquiris** fast ADC-board (for slicing) and a 4 GHz Lecroy Oscilloscope (mainly for ps pump-probe). Since, APD is sensitive to visible wavelength as well, its window is covered by Al foil so that only X-rays can pass though and all stray light (mainly coming from the IR laser pump pulses) in the chamber can be blocked. It is worth noticing that although I worked in the transmission mode, the APD can rotate to perform diffraction and scattering measurements. A cryostat equipped with a heat controller allows to adjust accurately the temperature of the sample from 80K to 400K (with liquid nitrogen). A fast-entry lock allows introducing samples without opening the main UHV chambers.

The ultrashort soft X-ray probe pulses (~100 fs) and the IR pump pulses (~50 fs) are (almost) colinear when they reach the sample. The X-ray spot size is 50 × 100 μm^2, therefore, in most of the experiment, we kept the laser spot size around 500 × 400 μm^2 (H × V) to ensure homogenous pumping. The laser spot size is adjusted by a telescope made of two pairs of cylindrical lenses. They allow changing the vertical and horizontal spot size separately. Since, the oscillator beam for seeding the pump amplifier travels through a 40-meter-long transfer line under vacuum, temperature and air pressure differences from day to night time can cause the drift of the spatial and the temporal overlaps. However, this drift can be 200-400 fs due to temperature difference from day to night time. A fluorescent screen of YAG crystal and a Mo-Si multilayer film [89] are mounted on the sample holder to check regularly the spatial and temporal overlap during the measurements. The thermal changes along the day also cause a drift of the photon energy, which is corrected by measuring the XAS and XMCD spectra every few hours. As explained previously, the laser amplifiers are seeded by the same oscillator which allows synchronizing the IR pump and X-ray probe pulses without jitters. An optical delay line is inserted in the optical path of the pump laser which allows to introduce and to adjust finely a delay between the pump and the probe to record the spin dynamics before and after the laser excitation. The combined temporal resolution of the IR pump (~50 fs) and X-ray probe after stretching by optics is around ~130 fs. The repetition rate of 3kHz and 6 kHz for the IR pump and X-ray probe pulses respectively allow to record the pumped and unpumped signal simultaneously. Since the pump-probe scheme relies on a stroboscopic measurement to cope with the low photon flux, it shows that the system relaxes to its initial state between two successive pump pulses.

Since, the photon flux does not allow to measure the XAS spectra on an extended energy range, therefore the XMCD is recorded by measuring the transmitted intensity at the photon energy to match the resonance of the TM L_3

or RE M_5 edges (at which XMCD is the maximum) for two opposite helicities of the magnetic. The laser induced spin dynamics is then recorded by measuring the XMCD as a function of the delay between the pump and the probe.

Due to limited photon flux, single measurement is not conclusive. Therefore, to improve the statistics, each measurement was repeated several times and then averaged them. However, to avoid any artifact due to shift in overlap or time zero, we measured both the configuration alternatively and compared the data from each day before averaging them all together.

3.1.3 Data processing and XMCD calculation

We recorded the change in the transmitted XAS intensity (I) as a function of pump-probe delay for the alternating magnetic field (H+ and H-) values. As, explained earlier, we can probe pumped and unpumped signal in same data scan and it provides a good normalization for each scan. We calculate the XMCD by subtracting the intensity measured for two magnetic field values and normalize the data from unpumped XMCD as follows:

$$XMCD_{pumped} = I^{+}_{Pumped} - I^{-}_{Pumped}$$

$$XMCD_{unpumped} = I^{+}_{unpumped} - I^{-}_{unpumped}$$

$$XMCD_{normalized} = \frac{XMCD_{pumped}}{XMCD_{unpumped}}$$

Where, $I^{+}_{Pumped/unpumped}$ and $I^{-}_{Pumped/unpumped}$ are the pumped and unpumped XAS intensity measured with positive (H+) and negative (H-) magnetic field values.

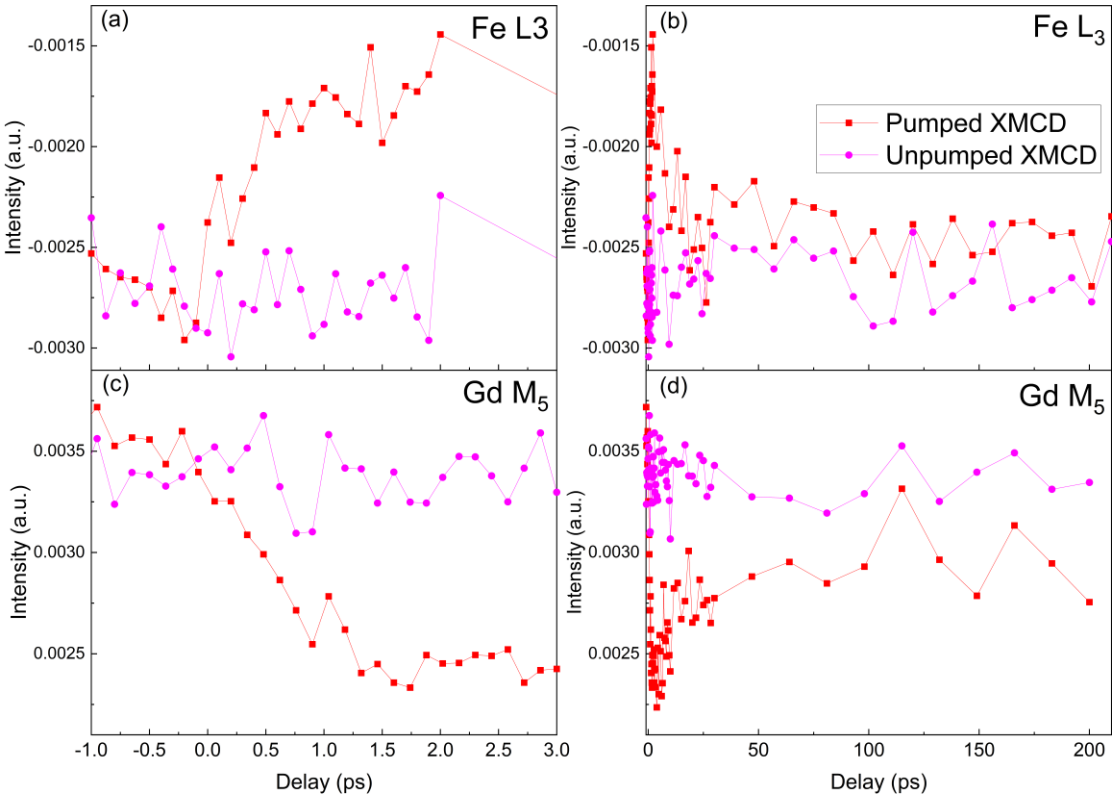

Figure 3.7: Time-resolved measurements of FeL_3 and Gd M_5 XMCD at incidence laser fluence of 40 mJ/cm² and at T= 140 ± 20 K working temperature. (a, b) XMCD calculated from the pumped and unpumped data for single delay at the Fe L_3 edge (Top panel) and Gd M_5 edge (Bottom panel) respectively. On the left side we represent the short time scale and at the right side longer time scales up to 80 ps delay. Here, $XMCD_{pumped}$ is represented by red dots. $XMCD_{unpumped}$ is represented by magenta (AP) showing "constant" intensities.

Figure 3.7 shows the change in pumped and unpumped XMCD with the pump-probe delay at the Fe L_3 and at the Gd M_5. To improve the statistics, we measured approximately 15-19 hours for each case to get reasonable statistics.

Chapter 4 Spin valve structure for spin-polarized hot electron induced dynamic

The main objective of my thesis is studying the ultrafast dynamics of 3d and 4f spins in RE-TM metal-based alloy systems induced by ultrashort spin-polarized hot-electrons (SPHE). The sample structure to achieve this goal should be composed of three parts:

1. the capping layer for the generation of hot-electron pulses,
2. the polarization layer (labeled FM_1) for spin-polarizing the hot-electron pulses,
3. the RE-TM detection layer (FM_2) in which the demagnetization will be investigated [41,45].

The adequate capping layer was already known from previous works [39,40]. Therefore, a major part of this work was to characterize the magnetic, electronic, and structural properties of magnetic layers and multilayers to identify the suitable materials for the polarization and detection layers. To identify the samples that comply with all these conditions, I combined different characterization techniques: XPS for electronic properties, SEM for the structural properties as well as MOKE, and XMCD for the magnetic properties. This chapter presents these studies and sample structures selected for my thesis work.

4.1 Sample structure

The sample structure used to study the spin-polarized hot electron (SPHE) effect consists of the following stack: Si_3N_4/Ta (5)/Cu (20)/Ta (5)/FM_2 (15)/Cu (t)/FM_1(t)/Cu (60)/Pt (6), as shown in Figure 4.1 (a). The numerical values in brackets are the thickness of each layer in nanometers. The top Pt (6)/Cu (60) layer is excited by an intense IR (800 nm) pump laser to generate the ultrashort Hot Electron (HE) pulses. Previous works have shown that most of the HE is generated in the Pt layer, and the conversion efficiency is optimized for a Pt thickness of around 6 nm [40]. The HEs are injected in the Cu (60) layer to be transported towards the buried FM_1 layer. Despite limited efficiency for the photoexcitation of HE, the Cu (60) layer has two fundamental functions: first, it absorbs the IR pulse to avoid direct IR excitation of the FM1 layer (see Section 4.1.1), and second, Cu (60) ensures the ballistic transport (i.e. minimum energy loss) [39].

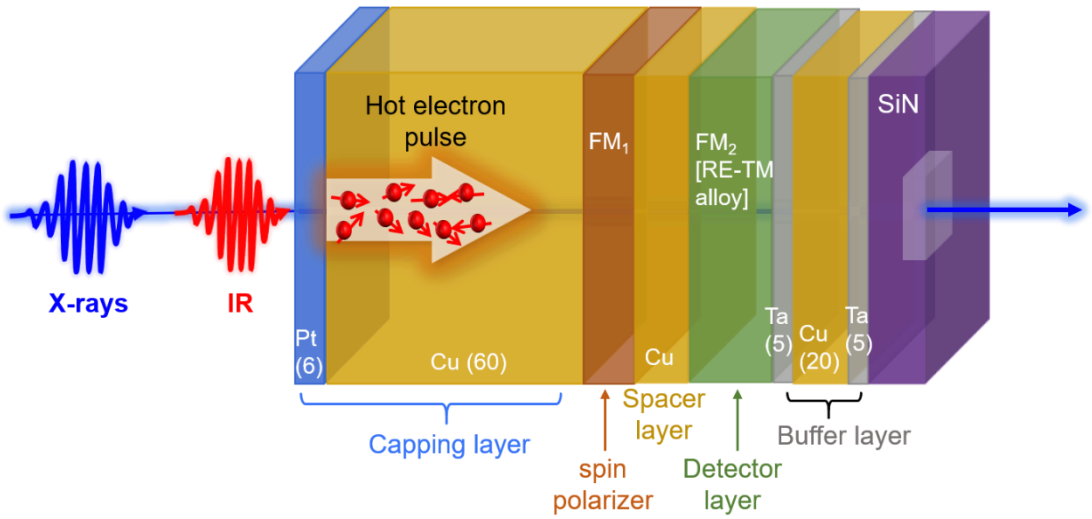

Figure 4.1: Schematic of sample structure: The sample structure used to study spin-polarized hot electrons (SPHE) induced dynamics consists of the following stack from right to left: SiN/ Ta (5) / Cu (20) / Ta (5) / FM_2 (15) / Cu (t) / FM_1/Cu (60) / Pt (6). The thicknesses of each layer in brackets are in nm. The large arrow in Cu(60) represents the direction of hot electrons flow, and inside it, the short red dots with red arrows represent the unpolarized hot electrons with their spins.

The unpolarized HE pulses, on passing through the first magnetic layer FM_1, generate the spin current (SC). Two main mechanisms play a role in SC generation: The first is when unpolarized HE passes through the polarizer magnetic layer, the spin parallel to the spin orientation of the magnetic layer (majority spins) has a higher probability of transmitting through the FM without being scattered than the minority spins. In contrast, minority spins are scattered at the interface, leading to one type of spins passing to adjacent layers. We get net spins polarized current due to the spin filtering effect [66]. The second is the generation of spin current by the hot electron-induced demagnetization of the FM_1 layer [32,39,40]. Later, these spin polarized hot electrons (SPHE), on passing through the Cu spacer layer, interact with the detector magnetic layer FM_2. Since these spin currents are absorbed by FM_2 within a few nanometer thicknesses (spin diffusion length (SDL) in Fe ~7 nm [90]) the excitation by SPHE is dominant in the first nanometers of the FM_2 film. Therefore, the thickness of FM_2 should be of the order of one or a maximum of two times the SDL. However, measurements at the very thin film below 10 nm are not possible at the femtoslicing beamline; therefore, the choice of 15 nm thick film is a tradeoff between such studies and experimental conditions. The Cu(t) layer is used as a spacer layer to magnetically decouple the FM_1 and FM_2 layers. The thickness of the Cu should be thick enough to magnetically decouple both layers (FM_1 and FM_2) but below the range of spin diffusion length in Cu (~13 nm) [5] to avoid large depolarization of the currents due to spin-flip scattering. Finally, a buffer layer of one Ta(5)/Cu(20)/Ta(5)

multilayer is needed for flat and homogenous growth and some heat dissipation.

Two main restrictions have to be considered while optimizing the sample structure. The first one comes from the experimental setup itself. Since the element selectivity and 4f sensitivity of time-resolved soft X-ray Magnetic Circular Dichroism (XMCD) spectroscopy is required, the measurements were carried out in the FEMTOSPEX chamber at the femtoslicing facility (BESSYII-Berlin) in the transmission mode. Therefore, the thin films were deposited on membranes transparent in the soft X-ray range. This experimental protocol further imposes the use of limited thickness of metallic layers to get enough transmitted X-ray, but a minimum thickness of detector layer is required to obtain sizable XMCD asymmetry. The second one was to select the magnetic layers in the spin valve structure, i.e., the spin polarizer and detector layer. Both the magnetic layers must have distinct coercive and saturation fields on an extended temperature range, and their saturation field values must be lower than the available magnetic field in the experimental chamber which is at a maximum 1.5 Tesla. Furthermore, the two layers FM1 and FM2 are magnetically decoupled, i.e., to align both relative magnetizations independently, corresponding to spin-valve structures.

4.1.1 Choice of capping layer Pt (6) /Cu (60)

As discussed previously, the choice of the top Pt(6) capping layer aims to i) maximize the intensity of the photoexcited hot electron pulses, which increases with the number of Pt layers, ii) minimize the re-absorbing of the hot electron current by electron scattering [40].

The Cu (60) layer is used to avoid the direct IR excitation of the FM1 and FM2 layers while ensuring their ballistic transport at the Fermi velocity of ~1 × 10^6 nm/fs [55]. In a previous work, Bergeard et al. claimed that 60 nm of Cu layer is the minimum thickness at which approximately 99% of the IR light is blocked [39]. Ideally, Cu thickness higher than 60 nm should be used to ensure the absence of residual excitation, since they have shown that the HE transports is ballistic upto Cu thickness of 150 nm. However, in our case, Cu thickness was determined by the specification of XMCD spectroscopy in transmission mode, which is restricted to a maximum thickness of 60 nm to get a reasonable signal-to-noise ratio.

To estimate the IR absorption in each layer and make sure that 60 nm is enough to block the IR laser, the absorption profile was simulated by using the Transfer matrix method (TMM) [91].

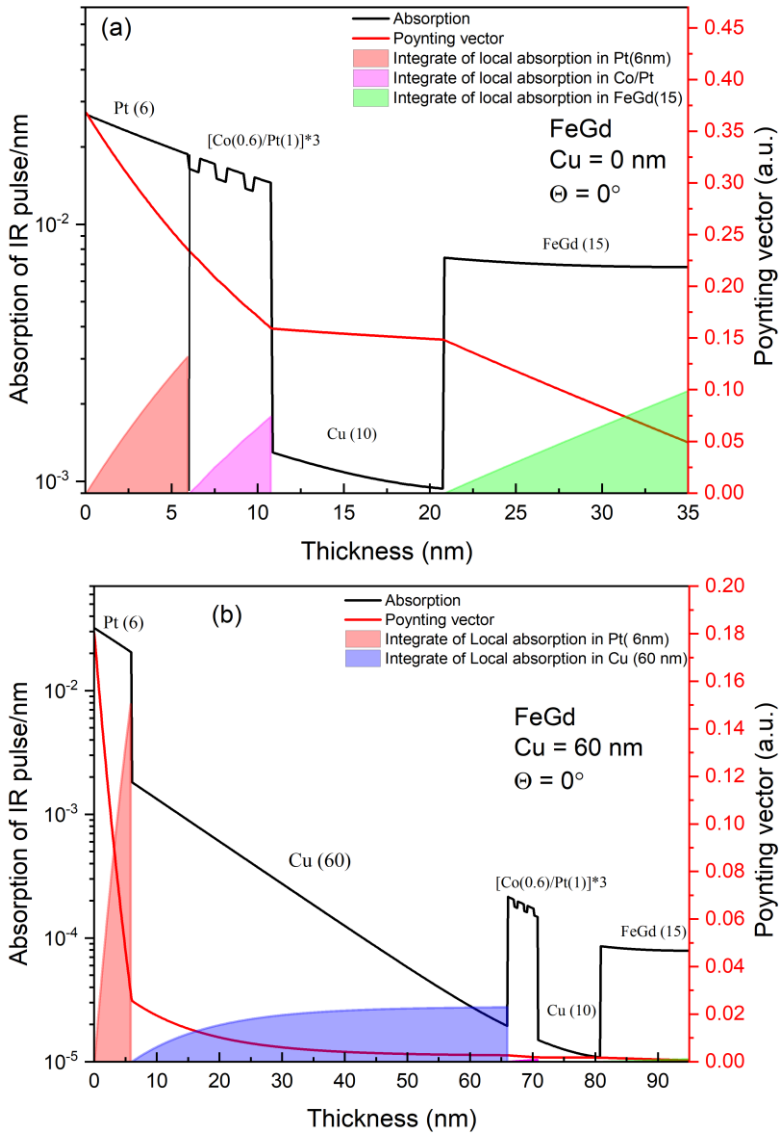

Figure 4.2: The calculated IR absorption profile for the whole sample structure for two thicknesses of Cu grown between Pt(6) and Co/Pt (a) Cu = 0 nm and (b) 60 nm using the TMM method [91] at normal incidence (θ = 0°). The black curve shows the IR absorption as a function of sample thickness (left Y-axis), and the red solid line is the resultant pointing vector (right Y-axis). The shaded area under the curve is the integral over the thickness of each layer to estimate the amount of IR absorption in whole thickness. Note that the left Y-axis shows a logarithm scale.

This method allows the calculation of the propagation of electromagnetic field through the sample. The parameters used to calculate the absorption profile are summarized in Appendix. In Figure 4.2, I simulated the IR (800 nm) absorption profile for the whole sample structure for two thicknesses of Cu located between the Pt(6) and Co/Pt films. I show the results for Cu (a) = 0 nm and (b) = 60 nm at a normal incidence angle θ = 0. The simulations show the

Poynting vector, depth-dependent absorption, and integral over the thickness of each layer in both cases (absorption is given per nanometer).

Therefore, to evaluate the total absorption in each layer, I integrated the area of each layer (shown in filled color), and I estimated the amount. Additionally, we also calculated the reflectivity of the sample. These values helped in calculating the amount of energy given to the system during IR excitation. Table 1 shows the results for different thicknesses and 0 ° incidence angles.

Samples	Absorption				Reflectivity
	Pt	Cu	FM1	FM2	
Pt(6)/Cu(0)/{Co/Pt}*3/Cu(10)/FeGd(15)	0.132	-	0.074	0.104	0.63
Pt(6)/Cu(60)/{Co/Pt}*3/Cu(10)/FeGd(15)	0.15	0.023	0.0008	0.0012	0.82

Table 4.I: Result of absorption profile for Cu thickness of 0 and 60 nm at incidence angle θ = 0°. Note that using Cu (60), the IR reflectivity is 82%, so only 18 % of the incident IR light is absorbed by the sample.

The results in Table 1 show that in the absence of Cu, both the magnetic layers are strongly excited by IR. However, with 60 nm of Cu, absorption at the bottom spin valve structure could be completely avoided. We also notice that at the Co/Pt ultrathin multilayer, a 10^{-3} residual IR laser light is present. However, this contribution is extremely small, so no IR-induced demagnetization is expected at the Co/Pt film, avoiding any influence on the SPHE-induced demagnetization in the bottom RE-TM alloy.

4.1.2 Spin valve structure

This work aims at studying the impact of spin-polarized hot electrons (SPHE) on the demagnetization dynamics. Therefore, we used a spin valve structure consisting of two magnetic layers: FM_1 (15)/Cu (t)/FM_2(t).

Here, FM_1, the first hard magnetic layer, acts as a spin polarizer (fixed layer), which is used to generate SPHE pulses. FM_2 is the layer of interest (detector layer) on which the SPHE-induced ultrafast demagnetization dynamics are studied. The Cu (t nm) layer ensures that FM_1 and FM_2 are magnetically decoupled.

This work focuses on studying the SPHE effect on ferrimagnetic systems; therefore, we chose RE-TM alloys for the FM_2. Since they are ferrimagnetic, both 3d and 4f moments can be studied in the same experiment using the same pump-probe parameters.

Based on previous work of the group [22,84,92] where IR laser induced demagnetization was studied in different CoGd alloys, we extend to SPHE

induced study on similar CoGd alloys. Since CoGd shows in-plane anisotropy, we selected a thin CoPt alloy film showing an in-plane anisotropy, as the spin polarizer (FM_1).

The second FM2 system was chosen to show faster demagnetization dynamics and have a different TM element than the FM1 layer, so that we could measure at the TM L_3 edge, which cannot be achieved with the CoGd film. We chose the following alloys: FeGd and FeCoGd. The FeCoGd alloys are well known for their all-optical switching (AOS) [26,27] and show fast IR-induced demagnetization dynamics [23] for Gd 4f compared to that of CoGd [92]. The FeGd alloys have been recently extensively studied and characterized for their magnetic properties as a function of concentration by Hintermayr et al. [49]. Both alloys comply with the required characteristics in the spin valve structures and for the FEMTOSPEX experimental station. These alloys show out-of-plane anisotropy, providing better experimental conditions at slicing due to normal incidence instead of measuring with an angle (in case of in-plane magnetization) with respect to X-ray direction. In order to match the out-of-plane anisotropy of FM_2, we chose a thin {Co/Pt} multilayer for FM_1.

Finally, we have optimized the following structures for both types of spin-valve structures:

1 - Si_3N_4/Co_xGd_{100-x} (15)/Cu (4)/Co_xPt_{1-x}(t)/Cu (60)/Pt (6) (In-plane)
2 - $Si_3N_4/(Co_yFe_{1-y})_xGd_{100-x}$ (15)/Cu (10)/{Co (0.6)/Pt (1)}*3 /Cu (60)/Pt (6) (Out-of plane)

Where subscripts show the atomic concentration in alloys, t is the thickness in nm. The magnetic properties can be tuned by varying the concentration, thicknesses, and number of repetitions in the case of the Co/Pt multilayers. In this work, Co/Pt layer repartitions were kept fixed.

All the element selective measurements, static XMCD at the PM3 beamline and tr-XMCD at the femotslicing beamline, were performed in transmission geometry. Therefore, to measure the transmitted XAS intensity, all the thin films were deposited on a 200 nm thick freestanding Si_3N_4 membrane (0.5 × 0.5 mm^2) on a Si frame (7.5 × 7.5 mm^2), which is nearly transparent for soft X-rays (Si-Si_3N_4 substrates were purchased by Silson Ltd.).

Due to limited photon flux in slicing, at 700 - 1300 eV (~1000 photons per pulse), the thickness of FM_2 was always 15 nm to get the optimum XAS intensity. This was optimized by previous studies [39,41,45], particularly for the measurement at slicing.

4.2 Sample preparation

All the samples used in this thesis were grown by magnetron sputtering by Michel Hehn at IJL Nancy. During deposition, base pressure was less than 2 × 10^{-8} mbar, which ensures no impurity while deposition. The different layers of RE-TM alloys, such as FeGd, CoGd, and CoPt, were deposited at the pressure of 3 × 10^{-3} mbar. The deposition rate was adjusted by the power on the deposing targets to get the desired composition of each alloy.

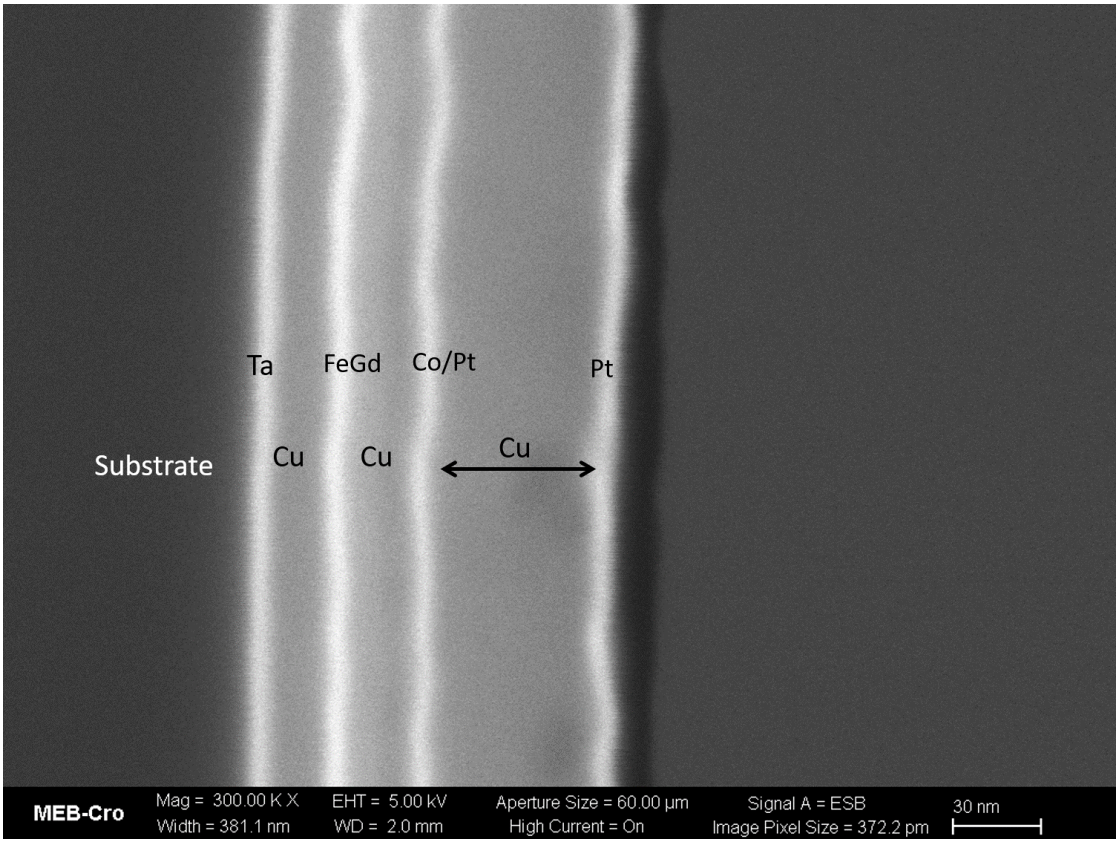

Figure 4.3: Cross-sectional SEM image of the deposited multilayer structure. We notice the homogenous layers and smooth interface throughout the film. The spacer layers and the top Cu(60) capping layer do not show any local "holes" or "reduced thicknesses," so one can assume homogenous IR absorption and HE propagation towards the bottom magnetic layers.

Figure 4.3 shows the cross-section image measured by scanning electron microscopy (SEM) by Zeiss Gemini SEM 500. Imaging was done by using an electron beam energy of 5 kV and measured the backscattered electrons. SEM image shows the uniform interfaces across the sample, and the capping layer (60 nm) does not have any inhomogeneity in thickness. This ensures the homogenous IR absorption and HE propagations through each layer. In the

next section, I discuss optimizing each layer using different characterization techniques.

4.3 Optimization and characterization

The main challenge was to identify suitable samples for the SPHE study. Therefore, we optimized spin valve structures by characterizing the magnetic properties of different RE-TM alloys, such as CoGd, FeGd for FM_2 and CoPt alloys (IP) and Co/Pt multilayers (OP) for FM_2, as explained in the previous section. To optimize the composition and thickness of each layer, the characterizations were performed using MOKE at IPCMS and X-ray spectroscopies at large-scale facilities such as X-ray absorption spectroscopy (XAS) and X-ray photoemission (XPS) as a function of temperature.

4.3.1 Magnetic properties of {Co/Pt}*3/Cu(10)/$Gd_x(Co_{1-y}Fe_y)_{1-x}$(15) spin valve structure

This section discusses the magnetic properties of four different FeGd alloy systems. In order to avoid crossing the compensation temperature (T_M) during the pump-probe measurements, we choose alloys with Gd concentrations that have compensation either below 80 K or above 300 K because the temperature range available at the femtospex chamber lies between 80 and 300 K in case of cooling down by liquid nitrogen (LN2). All the pump-probe measurements are performed at 80 K. Since, no balance between heater and liquid N2 flow is needed, therefore, this temperature provides best possible temperature stability during the measurement.

According to [49], Gd with the concentrations of Gd21% and Gd22% exhibit no compensation temperature (T_M) and are both Fe dominant (i.e. Fe shows a larger magnetic moment than Gd). In the theoretical work of Chimata et al. [50], they calculated the variation of T_M and Tc as a function of Gd concentration using the LLG model. They compared it with the experimental work [93]. They observed Gd concentration above 25% have T_M > 350 K, and T_C ~ 500K. Finally, we chose the following four alloy compositions and studied their properties as a function of temperature by MOKE and static XMCD before the pump-probe experiment:

S 1 - $Fe_{69}Co_9Gd_{22}$ (15)/Cu (10)/ {Co (0.6)/Pt (1)}*3
S 2 – $Fe_{67}Co_9Gd_{24}$ (15)/Cu (10)/ {Co (0.6)/Pt (1)}*3
S 3 - $FeGd_{20.9}$(15)/Cu (10)/ {Co (0.6)/Pt (1)}*3
S 4 - $FeGd_{26}$(15)/Cu (10)/ {Co (0.6)/Pt (1)}*3

The Gd(FeCo) alloys have been studied extensively for ultrafast magnetism due to their strong out-of-plane anisotropy and stability on laser excitation. Therefore, samples S1 and S2 were Co-doped with 9% of Co to increase the out-of-plane magnetic anisotropy.

In order to get larger coercive fields in the polarizer {Co (0.6)/Pt (1)}*n than in the ferrimagnetic FeGd and FeCoGd alloys, we had to select the following multilayer {Co (0.6)/Pt (1)}*3 (optimized by M. Hehn). In Co/Pt multilayer structures, out-of-plane anisotropy originates from interfacial anisotropy due to the induced magnetization in Pt by adjacent Co layers. Therefore, Pt (1 nm) is generally used to provide good (111) texture and is sufficiently thin to couple both the Co layers. Co (0.6 nm) was used to get the desired magnetic properties for the spin valve structure, such as Curie temperature (T_C) and Coercive field (H_C) of the Co/Pt multilayer structures. Cu (10 nm) was used to decouple both magnetic layers. Since both layers have out-of-plane anisotropy, to avoid the interaction of stray magnetic fields of both layers, it was important to use a thin layer, which is not only thick enough to magnetically decouple them but also considering the limited spin diffusion length so that spin-polarized hot electron can travel ballistically through. Therefore, Cu (10 nm) was chosen to provide the best spacer layer for PMA-based spin valve structures [94].

4.3.1.1 Hysteresis as a function of temperature by MOKE measurements

We performed the MOKE measurements in polar geometry (as shown in sec. 3.1.1.1) as a function of temperature ranging from 170 -300 K. We cooled down our cryostat with liquid nitrogen and could achieve the lowest temperature around 170 K. Figure 4.4 shows the hysteresis of all four compositions for two temperatures, T = 300 K (Fig 4.4(a)) and T = 173 K (Fig 4.4 (b)).

The hysteresis of all alloys shows that the sample has an out-of-plane anisotropy easy axis. The shape of hysteresis shows that both magnetic layers have distinct coercive fields (H_C). The MOKE is sensitive to 3d elements only, so we get the contribution of TM sublattices from both the layers, i.e., Fe and Co from FeGd and Co/Pt.

In order to estimate the coercive field (H_C) values of the FeGd and Co/Pt layer, we also measured the minor loop. These minor loops were recorded by sweeping the very small field values (lower than H_C of a hard layer) so that the hard layer would not be disturbed, and we get the contribution of the soft layer

only. These minor loops are shown by solid light color lines of their respective hysteresis in Figure 4.4.

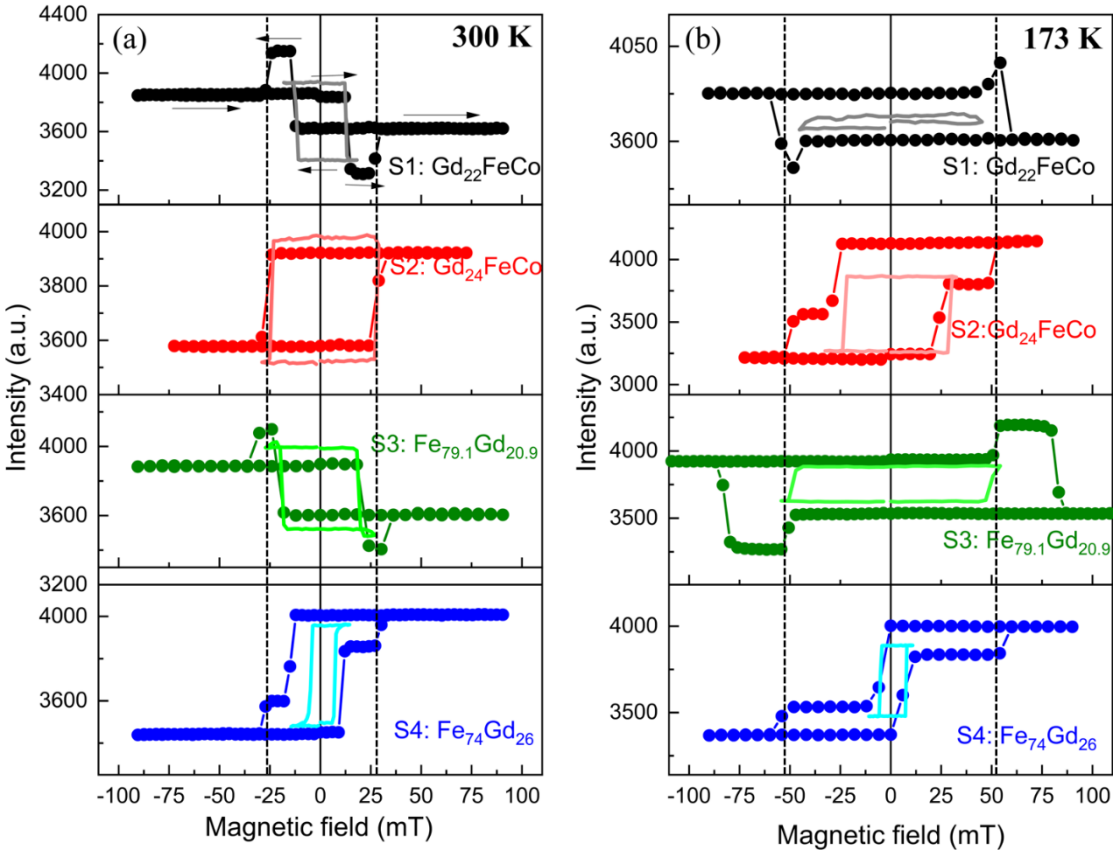

Figure 4.4: Hysteresis measured by MOKE at (a) T = 300 K and (b) 173 K for four different compositions: S1 – S4 (top to bottom). All the samples have the same color code in both graphs and the whole chapter. Solid circles represent the full hysteresis of each bilayer structure. Light color solid lines show the minor loop measured by sweeping magnetic field values lower than H_C of the larger loop of Co/Pt. Vertical dashed lines denote the H_C of the Co/Pt layer in each bilayer, which doesn't change when the composition of the RE-TM alloys changes.

Since Co/Pt has the same thickness in all the samples, we do not expect any change in H_C of Co/Pt when changing the concentration. Therefore, we drew a vertical line crossing all the hysteresis. This dashed vertical line represents the H_C of the Co/Pt layer. Due to the strong temperature dependence of magnetization, these bilayers showed different hysteresis at 170 K. It's clear from the full hysteresis that the H_C increased from 25 mT to 50 mT when decreasing the temperature from 300 K to 173 K. However, the minor loop showed distinct behavior with temperature. In the case of S2 and S4, H_C did not change on changing the temperature. However, it increased in the case of S3. A minor loop of S1 at 173 K shows non-magnetic behavior, but it's difficult

to say whether this is due to the absence of enough magnetic field to saturate the soft layer or if we are at the T_M of this alloy.

From the MOKE measurements, we could see the evolution of Hc with temperature. The MOKE is sensitive to probe 3d electrons; therefore, in the MOKE signal, we get the contributions of both 3d elements (Fe and Co) from the two magnetic layers. We notice that sample S4 shows reasonably small Hc (minor loops) in the 170-300 K temperature range compared to that of the Co/Pt and could be compatible with the pump-probe experiments at low temperatures. However, our experimental set-up doesn't allow to measure below 170 K. Therefore, in order to characterize all the essential parameters of the samples in a more definitive way, we performed element-selective XMCD measurements at PM3 -HZB BESSY at the CoL_3, GdM_5, and FeL_3 edges from 80 K to 300 K. The results are discussed in the following sections.

4.3.1.2 XMCD measurements

As discussed in the previous section, a detailed XMCD analysis at the Fe (and Co) L_3 and Gd M_5 edge is required to figure out the H_C of each magnetic layer on the whole temperature range covered on the femtoslicing endstation. It's also necessary to quantify the XMCD amplitudes at both edges at the selected temperature to ensure that these values are large enough to record time-dependent XMCD with the low energy resolution of the zone plates during the slicing experiments.

The element-specific XAS-XMCD measurements were performed at Alice chamber, PM3 beamline, HZB-BESSYII, Berlin [95]. We recorded the XAS and XMCD spectra at $L_{2,3}$ edges of Fe and Co and Gd $M_{4,5}$ edges at temperatures ranging from 80 K to 300 K in transmission geometry. Since our samples have out-of-plane anisotropy, all the measurements were carried out in normal incidence, so the X-ray and magnetization directions are collinear (experimental geometry in section 3.1.1.2).

We measured the XAS spectra along two opposite magnetic fields, H+ and H-, to observe the magnetic contrast. We calculated magnetic XMCD by subtracting the XAS intensity measured at H+ and H-. Figure 4.5, and 4.6 shows the XAS and XMCD spectra measured at the Fe $L_{2,3}$ and Gd $M_{4,5}$ edges at two extreme temperatures reached during our measurements, T=80 K and 300 K, for all four compositions. The XMCD signal at the Fe L3 edge shows only a small reduction of 15 % in XMCD on increasing the temperature from 80 K to 300 K. This shows that the magnetic properties for Fe don't change. However, in the case of Gd M_5, the XMCD decreased by 30% on approaching 300 K.

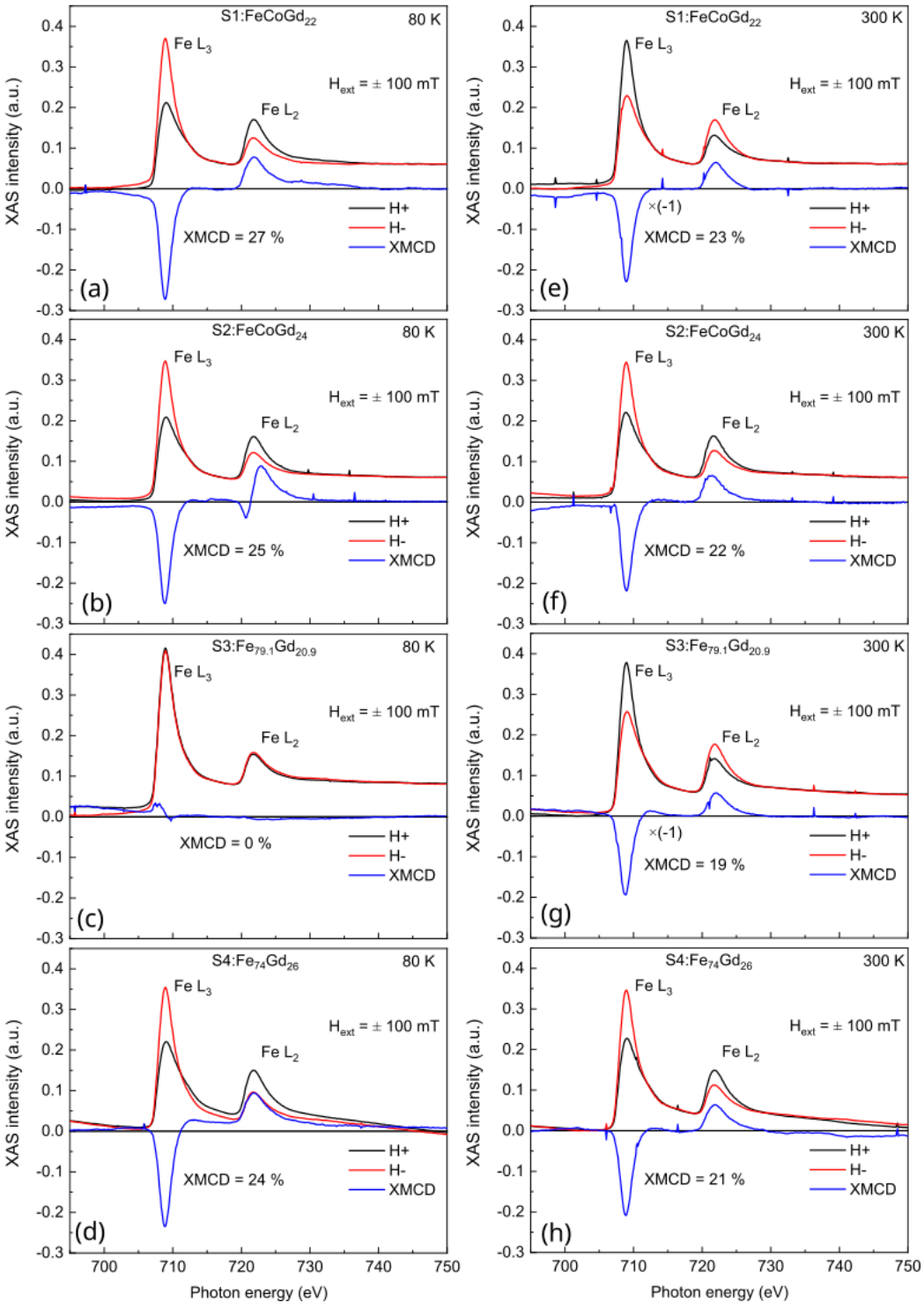

Figure 4.5: XAS and XMCD (blue) spectra at Fe $L_{2,3}$ edges measured by applying two opposite magnetic fields H+ (black) and H-(red) normal to the sample at T = 80 K (left) and 300 K (right) for four compositions S1: $FeCoGd_{22}$(row1), S2: $FeCoGd_{24}$ (row2), S3: $FeGd_{20.9}$(row3), S4: $FeGd_{26}$(row4). In some cases, change in XAS and XMCD sign shows that sample temperature is above T_M. Multiplication of (-1) to XMCD depicts the positive XMCD, and magnetization is dominant by Fe sublattices.

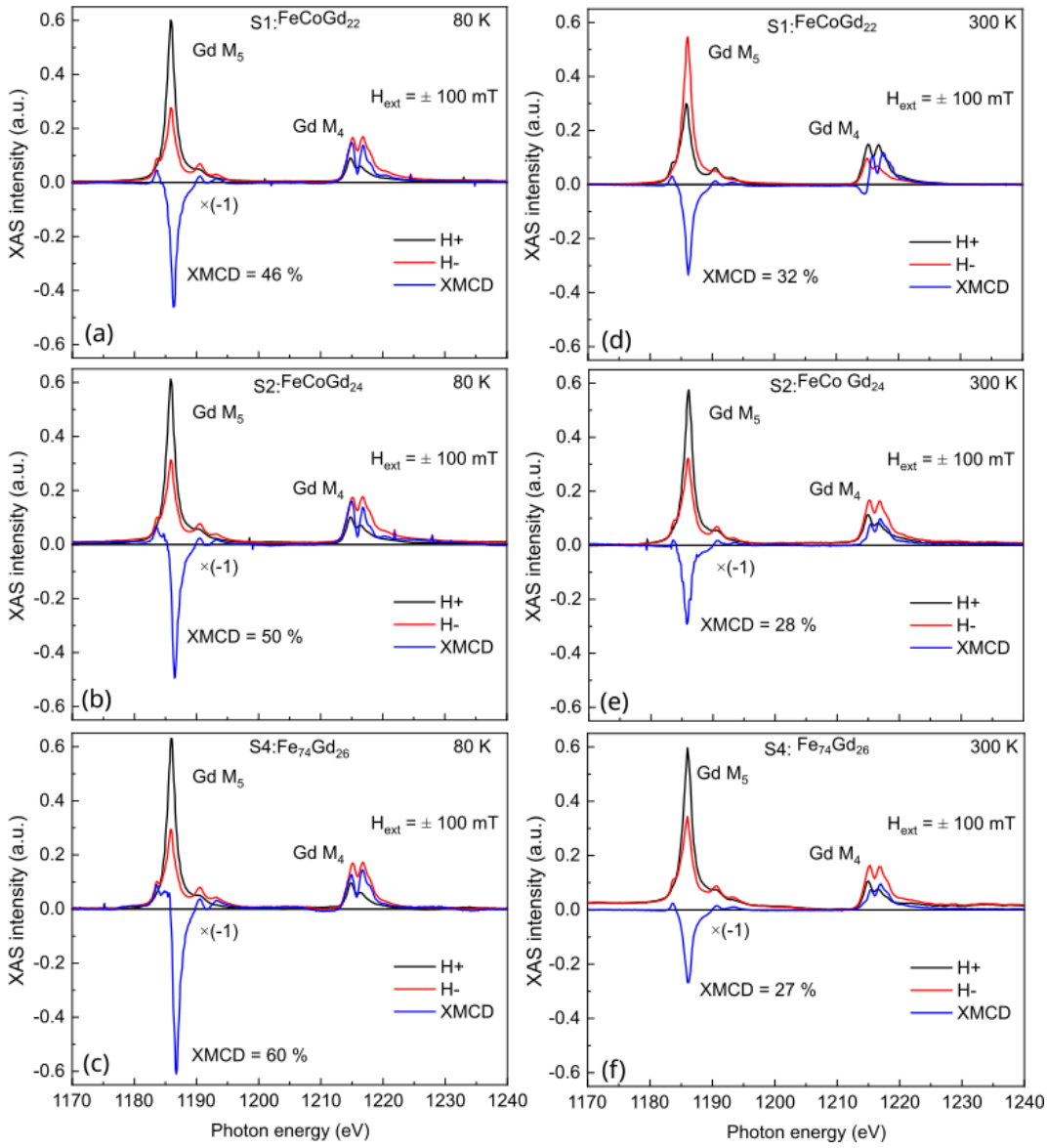

Figure 4.6 XAS and XMCD (blue) spectra at Gd $M_{4,5}$ edges measured by applying two opposite magnetic fields H+ (black) and H-(red) normal to the sample at T = 80 K (left) and 300 K (right) for four compositions S1: $FeCoGd_{22}$(row1), S2: $FeCoGd_{24}$ (row2), and S4: $Fe_{74}Gd_{26}$(row4). In the case of Gd, in the majority of cases, we are below T_M. Therefore, the XMCD value is always positive, and magnetization is dominant by Gd sublattices. Multiplication of (-1) to XMCD depicts the positive XMCD.

For S3 and S4 samples, the data quality and background were reasonable, so we extracted the m_S and m_L values for Fe and Gd in these alloys using sum rule calculations [28,78,79], given in Table 4.2. The calculated values were in good agreement with the literature [23]. I calculated these values in order to give as an input for modelling.

Sample	Fe (μB/atom)	Gd(μB/atom)
$FeGd_{20.9}$(15) (80K)	m_S= 2.62 ± 0.5 m_L = 0.197 ± 0.2	ms = - 5.84 ± 1.0 m_L = 0 ± 0.5
$FeGd_{26}$(15) (80K)	m_S = 2.86 ± 0.5 m_L = 0.266 ± 0.2	ms = - 4.92 ± 1.0 m_L = 0 ± 0.5

Table 4.II: Calculated ms and mL for the FeGd alloys by applying the sum rule on XMCD data at 80 K.

We also recorded the hysteresis at the L3 edge of Co and Fe, and M_5 edge of Gd at temperature from 80 K to 300 K for the same samples as above. We set the photon energy at the maximum of the XMCD signal, i.e., 779.5 eV (Co L_3), 709 eV (Fe L_3), and 1186 eV (Gd M_5), respectively. Figure 4.7 (a,b,c) shows the element selective hysteresis graphs for the Co, Fe, and Gd at 80 K (black), 170 K (red), and 300 K (blue) for all four samples (S 1-4).

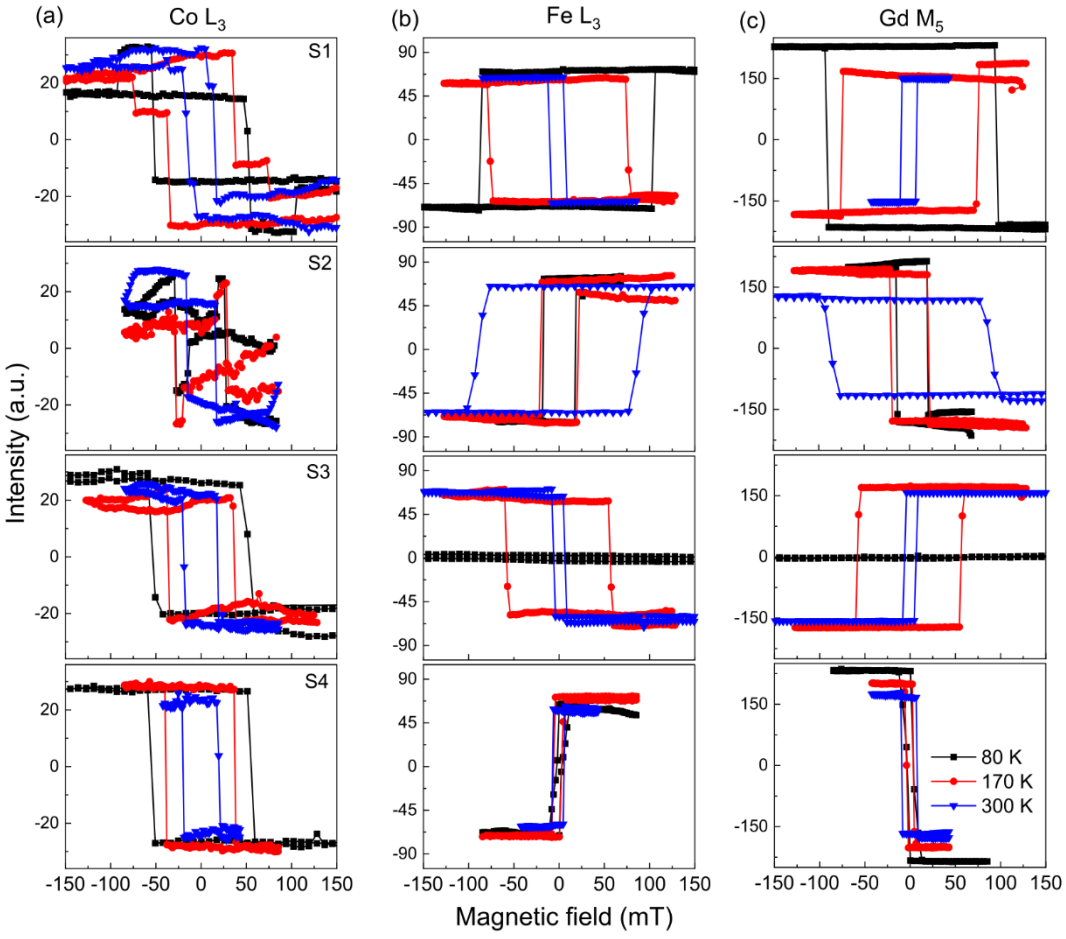

Figure 4.7: (a,b,c) Element selective hysteresis loops plotted at (a) Co L_3 (779.4 eV) (column1), (b) Fe L_3 (709 eV) (column2), and (c) Gd M_5 (1186 eV) (column3) at T =

80 K (black), 170 K (red) and 300 K (blue) for all four compositions. All samples are arranged in rows, i.e., rows 1-4 for all four compositions. (a) The hysteresis at Co L_3 shows the change in H_C of the Co/Pt layer with temperature. It decreases on approaching 300 K and becomes approximately equal to the bottom FeGd layer. (b,c) The hysteresis at Fe and Gd shows the exact opposite sign of hysteresis, representing the antiferromagnetic coupling of both sublattices. In the case of S2 and S4, Co and Fe loops are opposites; it shows that T_M is above 300 K, and magnetization in those alloys is dominant by Gd moments.

By examining the hysteresis as a function of temperature, we could estimate the T_M of each composition if it exists within the temperature range. The XAS and hysteresis of $FeCoGd_{22}$ show the opposite sign at 80 K and 170 K, i.e., T_M lies within this range; we estimated it to be 100K. In the case of S3, XMCD is zero at 80 K, which reflects that the TM is equal to 80 K. Both values agree with the literature [50]. In the case of $FeCoGd_{24}$ and $FeGd_{26}$(both are nearly equal concentration with 2% change), hysteresis shows no reversal in the sign until 300 K. It shows that T_M is above 300 K and magnetization in these alloys' dominant by Gd moment, which can be seen from the hysteresis of Fe and Co in Figure 4.7, which are antiparallel to each other, vice versa in case of Gd.

Figure 4.8 (a) shows the variation of H_C with temperature of both magnetic layers in the spin-valve structure. It's evident that Co/Pt (open triangles) has the same H_C in all samples at a given temperature. The temperature variation at CoL3 shows a slight decrease from 55 mT (T= 80K) to 20 mT (T=300K). However, the FeGd alloys show very distinct behavior with temperature. Among all four compositions, S4 ($FeGd_{26}$– blue data) has a very low value for H_C, well below the one for Co/Pt in the whole temperature range as well as this alloy has a T_M value larger than 300 K. Figure 4.8 (b) shows the variation of TM and TC of FeGd alloys with Gd concentration (10 – 35 %). In this Figure, data is plotted from the different literatures [49,50,93] (solid points) and compared with our experimental result (green open circle). The error bar on the green circle shows the uncertainty in T_M for all alloys. Figure 4.8 b (blue squares) shows that T_C remains constant within the given range of Gd concentration.

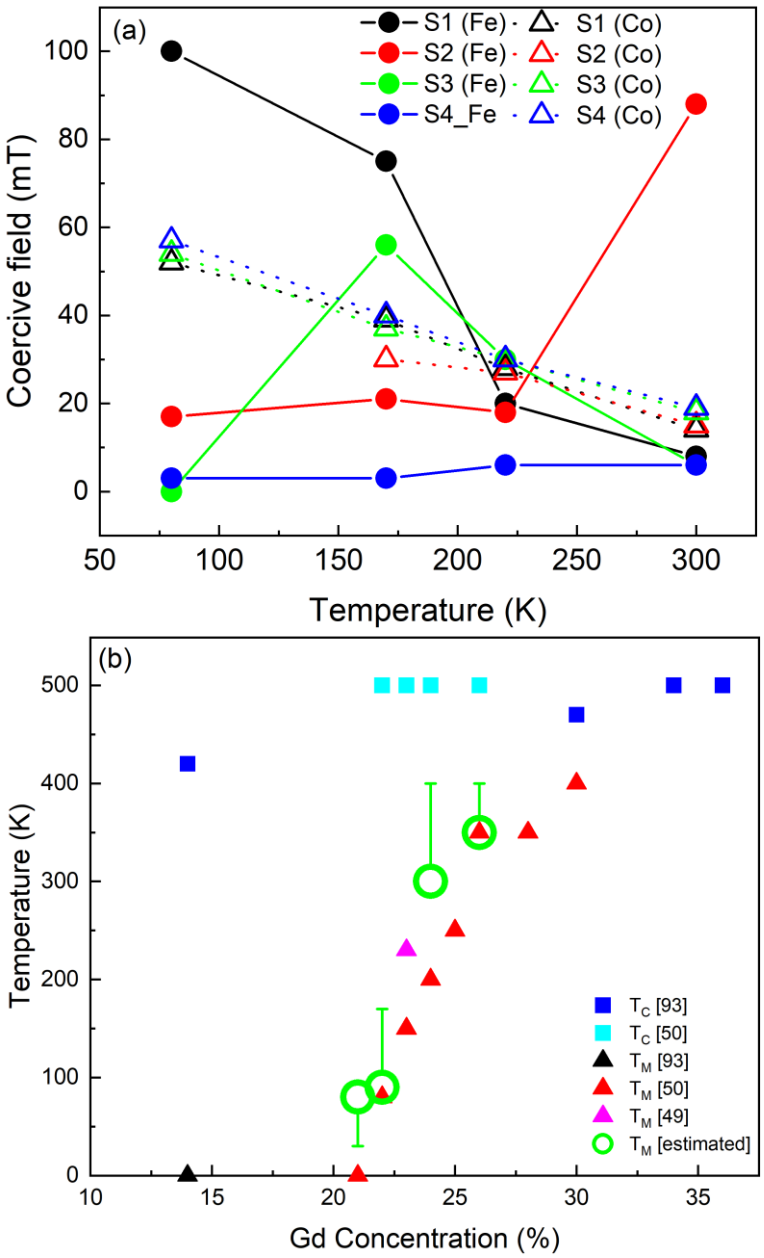

Figure 4.8: (a) Variation of H_C as a function of T at Fe and Co L_3 edges. Solid circles represent the Fe, and an open triangle represents the Co for all four samples. (b) magnetic compensation temperature (T_M) and Curie temperature (T_C) as a function of Gd concentration in the FeGd alloy system. Solid squares and triangles represent the T_C and T_M, respectively, from the literature [49,50,93]. Large green open circles are the estimated data for T_M for S1, S2, S3, and S4 using the XMCD experiment, and the error bar corresponds to uncertainty in the determination of T_M.

The combined XAS and hysteresis at their respective edges provided a detailed overview of each bilayer sample's magnetic properties, which is crucial before performing TR-XMCD measurements. The key points of each bilayer can be summarized as follows:

S 1: In the case of $FeCoGd_{22}$, the reversal of XAS spectra (300K) (Fig 4.5 (S1)) and hysteresis (Fig 4.6 (b)S1) (170 K) shows that T_M lies between 80 K and 170 K. Due to limited data points, we estimated it to be 100 K, which is close to the reported value in the literature [50]. H_C of $FeCoGd_{22}$ is larger than Co/Pt until 170 K and then becomes equal to Co/Pt at higher T (Fig 4.8 (a) – black solid and open data points).

S 2: For $FeCoGd_{24}$, we did not observe the change in sign with T. However, the broadening of hysteresis at 300 K shows that we approach to T_M and H_C becomes larger than Co/Pt at 300 K. Additionally, the opposite sign of hysteresis of Fe ad Co is because below T_M, magnetization is dominant by RE sublattice. Therefore, Gd moments are aligned to magnetic field orientation.

S 3: $FeGd_{20.9}$ exhibits non-magnetic behavior (0 % XMCD) at 80 K, which depicts that the temperature is close to T_M and the applied magnetic field is not enough to saturate the sample.

S 4 $FeGd_{26}$ shows no T_M until 300 K, and the H_C of this alloy is always lower than Co/Pt (Fig 4.8(a) blue solid and open data points). This sample shows perfect pre-conditions for our slicing pump-probe experiments.

Due to limited time during femtoslicing beamtime, we need to ensure our sample and experimental parameters are optimized before the experiment. Therefore, all these measurements helped to understand all the bilayers in detail. We observed that $Fe_{74}Gd_{26}$ alloy showed the best characteristics for studying the spin-polarized hot electron effect.

4.3.2 Magnetic properties of $Co_{75}Pt_{25}(t)/Cu(t)/Co_xGd_{100-x}(15)$ spin valve structure

The previous work done by Tom Ferté et al. [92] showed that Gd with x = 21% has T_M around 270 K; above this concentration, they didn't observe any reversal in hysteresis or XAS [92]. According to work by Tao et al. [96], all alloys with Gd concentration between 16 - 25 % show a compensation temperature T_M. Therefore, for the study of the Co_xGd_{100-x} alloy system, we chose two compositions of Gd, i.e., x = 31.7 and 39 %. Based on the mentioned studies, these alloys should not have T_M between 80 K and 300 K, and their T_C is approximately 460 K and 350 K [71].

In order to comprehensive study before Tr-XMCD measurements, the magnetic properties of these alloys and their bilayers with $Co_{75}Pt_{25}$ (t) were examined by MOKE and element sensitive XMCD spectroscopy as a function of temperature ranging from 80 K to 300 K.

4.3.2.1 Magnetic properties of Co_xGd_{100-x} alloys: XMCD study

To study the element specific properties of both the alloys, XAS and XMCD spectra were recorded in transmission geometry as a function of temperature.

All the measurements were performed by tilting the sample at an angle of 35 ° with respect to the incidence angle of the X-rays. In such a geometry, we are sensitive to the in-plane magnetization of the sample. We measured the XAS spectra at two opposite magnetic field values (± H) at Co $L_{2,3}$ and Gd $M_{4,5}$ edges. We also recorded the hysteresis at the Co L_3 (779.5 eV) and Gd M_5 (1186 eV) resonant edges, respectively. We note that the XAS of Co L_3 is averaging the contribution of both thin films, CoPt and CoGd. However, using the parallel and antiparallel configurations in the spin valve, we can extract both XMCD contributions.

Figure 4.9 shows the XAS-XMCD (a-d) and hysteresis (e,f) of Co and Gd sublattices at T = 80 K and 300 K for $Co_{61}Gd_{39}$ (XAS represented by solid lines and hysteresis by solid circles) and $Co_{68.3}Gd_{31.7}$(XAS by dash lines and hysteresis by open circles) alloy thin films, respectively. The positive sign of XMCD at the Gd edge shows that both the alloys are below $T_{M,}$ and magnetization is dominant by Gd moments. Despite very different TC, both alloys showed approximately similar characteristics due to the localized nature of 4f. $Co_{68.3}Gd_{31.7}$ showed only 2% larger XMCD than $Co_{61}Gd_{39}$. H_C of both alloys is less than 5mT at 80 K.

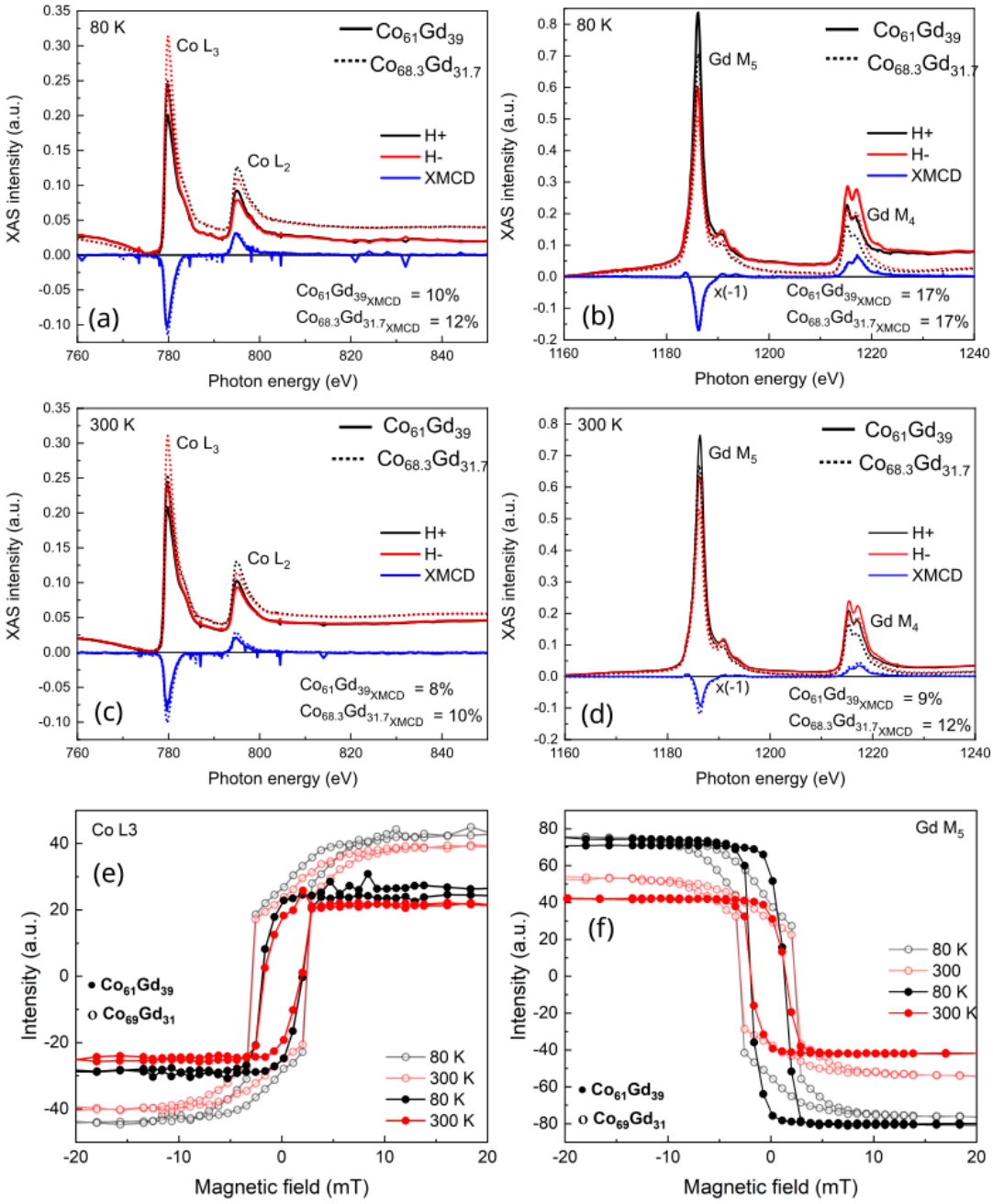

Figure 4.9: XAS and XMCD (blue) spectra measured for two different alloys, $Co_{61}Gd_{39}$ (solid lines) and $Co_{68.3}Gd_{31.7}$ (dashed lines), at two opposite magnetic fields H+ (black solid lines) and H-(red solid lines) at an angle of 35 ° with respect to X-ray direction to measure in-plane magnetization. (a, c) XAS-XMCD spectra at Co $L_{2,3}$ edges and (b,d) Gd $M_{4,5}$ edges at T = 80 K and 300 K, respectively. (e, f) Represents the hysteresis of $Co_{61}Gd_{39}$ (solid circles), and $Co_{68.3}Gd_{31.7}$ (open circles) at Co L_3 and Gd M_5, respectively.

4.3.2.2 Optimization of spin polarizer

We used the Co_xPt_{100-x} alloy as a hard magnetic layer (spin polarizer). In the work by Aboaf et al. [97], they observed very large coercivity at 75% of Co (~170 mT) with in-plane anisotropy. Therefore, we chose CoPt alloy with 75% of Co concentration.

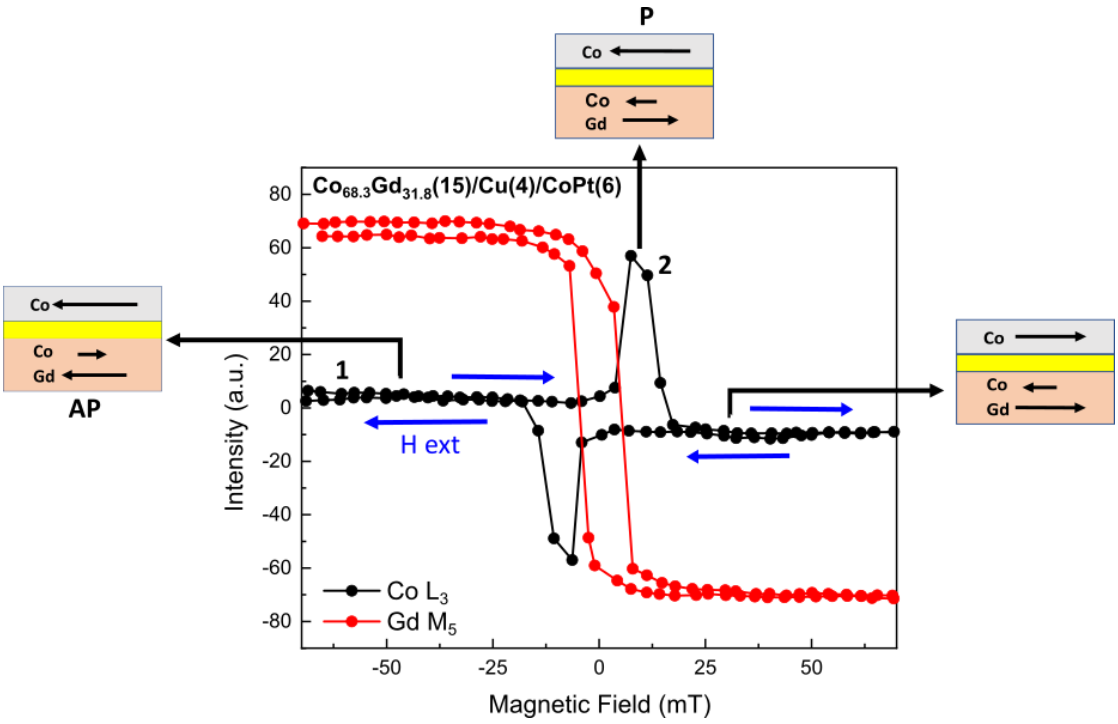

Figure 4.10: Hysteresis recorded at Co L_3 (black) and Gd M_5 (red) for bilayer $Co_{68.3}Gd_{31.7}$ (15)/Cu(4)/$Co_{75}Pt_{25}$(6) at 300 K. Blue arrow marked with H_{ext} shows the field sweep direction. Since, in CoGd, the magnetization is dominant by Gd moments and follows the applied magnetic field, Co shows opposite hysteresis (Fig 4.9(e)). Therefore, at a large magnetic field value (marked 1), i.e., at saturation, Co in both layers are antiparallel to each other (illustrated by the schematic in the box), and the resultant XMCD becomes zero. At point 2, the field value is large enough to switch the CoGd but not the CoPt layer; in this case, both Co align parallel and increase the intensities. Hysteresis at Gd M_5 shows that the H_C of CoGd is 5 mT.

To optimize the $Co_{75}Pt_{25}$ layer, we studied the variation of magnetic properties with the $Co_{75}Pt_{25}$ thicknesses by XMCD measurements as a function of temperature. Since both CoGd alloys show approximately similar properties (sec.4.3.2), therefore, in this section, I only discuss the results of $Co_{68.3}Gd_{31.7}$ (15 nm)/Cu (4 nm)/$Co_{75}Pt_{25}$ (t = 1.5, 3, 6 nm) bilayer structures.

We used Cu (4nm) as a spacer layer in all the bilayer structures. In this case, both magnetic layers have in-plane magnetic anisotropy, and the demagnetizing field in magnetic film with an in-plane easy axis is almost zero.

Therefore, a 4nm thickness of Cu is sufficient to decouple both magnetic layers. This has been verified using XMCD. The symmetric hysteresis at the Gd M_5 edge ensures no coupling between both magnetic layers.

Figure 4.10 shows the hysteresis at 300 K at Co L_3 (black) and Gd M_5 (red) edges, respectively. Since Co is present in both layers, hysteresis at the Co edge shows the contribution from both layers. This combined contribution of Co from both layers can be explained in the following manner:

- As marked 1 in the hysteresis, in the saturation state, i.e., at H = -50 mT, both the magnetic layers are aligned in the applied field direction (the black arrow shows the external field direction). Though $Co_{68.3}Gd_{31.7}$ has T_M above 300 K, magnetization is dominant by Gd and follows the magnetic field. In this case, Co moments in CoGd are antiparallel (AP) to the CoPt layer and compensate each other, resulting in zero net magnetization at the Co edge.
- If the field value is equal to the switching field of the bottom CoGd layer (~5 mT from Fig 4.9 (e,f)), then the CoGd layer switches to the field direction, but CoPt remains unchanged due to large H_C (~10 mT). In this case, Co in both layers are parallel (P) (as shown in the schematic in Fig 4.10), and their moments add up, resulting in a larger XMCD signal.

At the Gd M_5 edge, the situation is more straightforward. CoGd has T_M above 300 K, and magnetization in the alloy is dominant by Gd moments; therefore, Gd follows the magnetic field.

Additionally, we recorded the XAS spectra at positions 1 and 2 (as marked in Fig 4.10 at Co hysteresis) at Co $L_{2,3}$ and Gd $M_{4,5}$ edges. Figure 4.11 (a) shows the XAS and XMCD measured at the Co edge at H = ± 100 mT. Both layers are aligned in the applied field direction. XAS spectra show no magnetic signal, and XMCD is zero, as observed at Co hysteresis, the intensity at high magnetic field value becomes zero due to antiparallel orientation of Co. XAS spectra at position 2 (Fig. 4.11 b) shows the non-zero XMCD. We measured this XAS by applying a magnetic field in the following order:

- Hext = ∓ 100 mT (to saturate CoPt layer) → ± 7 mT (to flip the bottom CoGd layer) and measure the XAS spectra. In both cases, Co in both the layers is always parallel to each other.

The CoPt layer is ferromagnetic and always aligns in the applied field direction, which results in the positive XMCD at the Co edge (Fig. 4.11 b), unlike the Co in CoGd alloy systems.

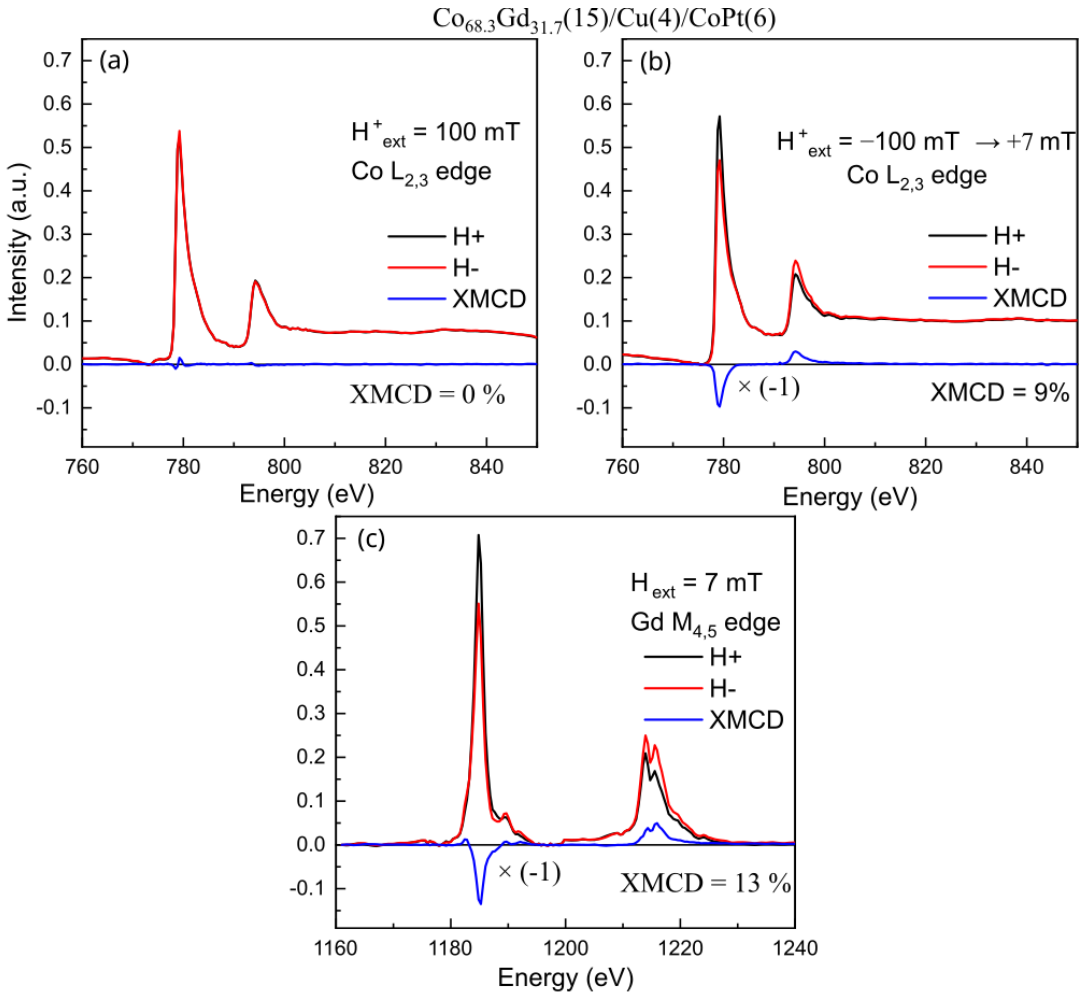

Figure 4.11: XAS and XMCD measured at the magnetic field values equal to points 1 and 2 in Figure 4.10 at Co $L_{2,3}$ and Gd $M_{4,5}$ edges at 300 K. (a) XAS measured in saturation (H = ± 100 mT), and Co in both layers compensate each other and results in zero net magnetization at Co edge (XMCD – 0%). (b) XAS was measured by flipping small field value after application of large H to saturate CoPt (∓ H (100 mT) → ± H(7mT)). (c) XAS and XMCD at Gd $M_{4,5}$ edge.

Figure 4.11 (c) shows the XAS and XMCD at Gd $M_{4,5}$ edges measured at H = ± 7 mT. The XMCD value at the Gd edge in the bilayer sample matches the pure CoGd layer (Fig. 8 (d)), which shows that the magnetic properties of the CoGd layer do not change in the bilayer structure. Therefore, we examined the change in properties of the CoPt layer with a variation of thicknesses from t = 1.5 nm to 6 nm, keeping the CoGd layer fixed.

Figure 4.12 shows the variation of hysteresis with CoPt thickness at 80 K (left) and 300 K (right) for $Co_{68.3}Gd_{31.7}$ (15)/Cu(4)/CoPt(t) bilayers. CoGd concentration and thickness were the same in all the samples, and only the CoPt layer varied from 0 – 6 nm (bottom to top). All the hysteresis were recorded at Co L_3 edge. In the hysteresis, the inner loop shows the hysteresis of the CoGd layer, and the outer loop shows the CoPt. It's clear that when the thickness

increases, the H_C of CoPt increases, but CoGd remains the same, as expected. Also, the number of Co atoms increases with the thickness, which leads to an increase in intensity at the magnetic field value where Co is in both layers (point 2 in Fig. 4.10). Hysteresis at 80 K showed a further increase in H_C from 5 mT to 10 mT for the CoPt layer.

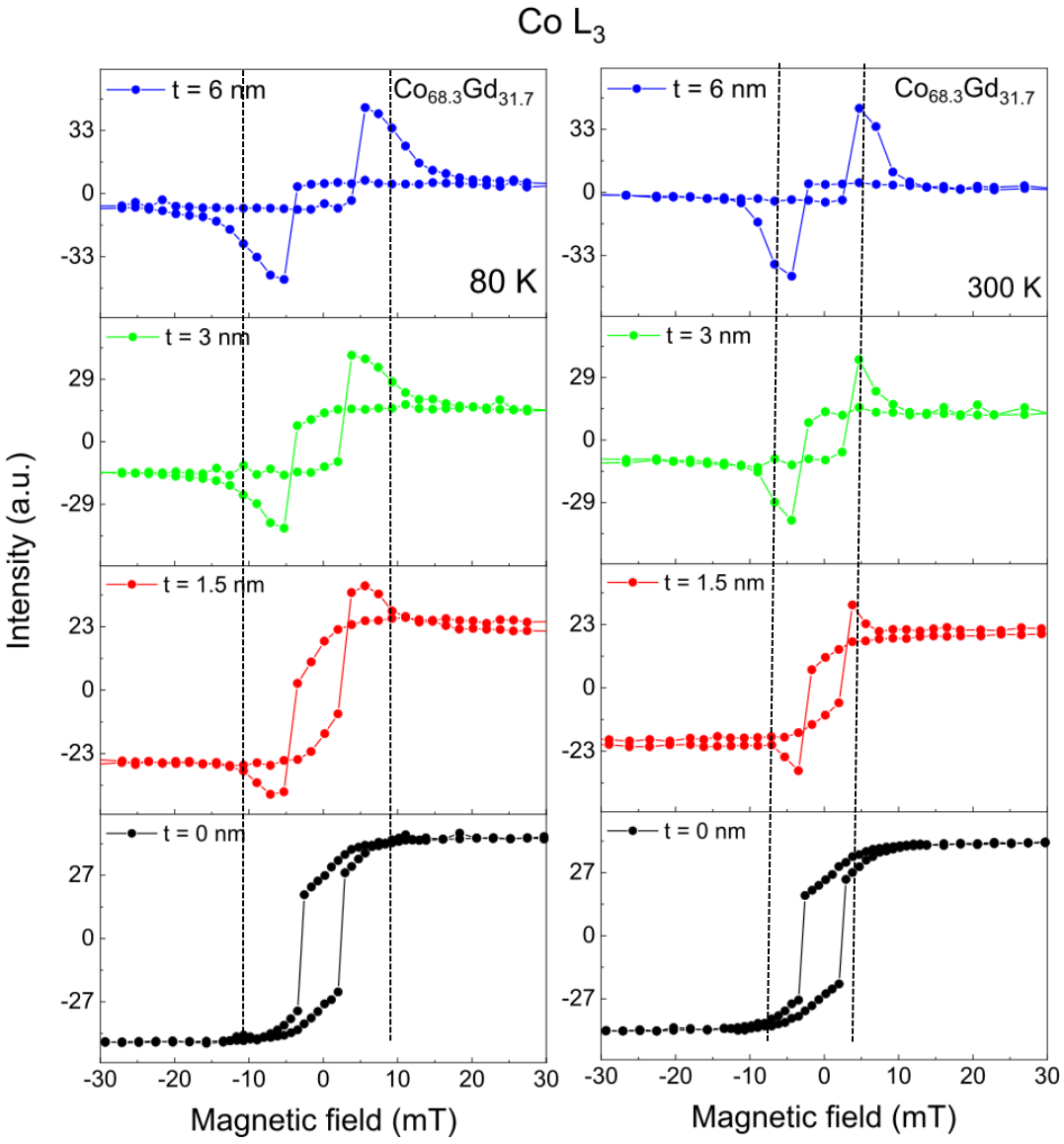

Figure 4.12: Co L_3 XMCD extracted hysteresis as a function of $Co_{75}Pt_{25}$ layer thickness (t) from 0 nm to 6 nm (Bottom to top) at 80 K (left) and 300 K (right). The outer hysteresis, which represents the CoPt (hard magnetic layer), increases by increasing the thickness, but the inner hysteresis, which shows the bottom soft CoGd layer, remains constant. The number of Co atoms increases with the thickness and results in an increase in intensity when both layers are parallel.

In Figure 4.13, I summarize the variation of HC as a function of temperature for all three thicknesses of $Co_{75}Pt_{25}$ and Co_xGd_{100-x} alloys

with x = 39 and 31.7%, respectively. It's clear that CoGd alloy always shows H_C lower than the CoPt layer. However, the H_C of CoPt (1.5 nm) is close to the CoGd alloy system. We finally decided to select the CoPt (3 nm) film as a polarizer so that its thickness stays reasonably thin, limiting the scattering of the HE current.

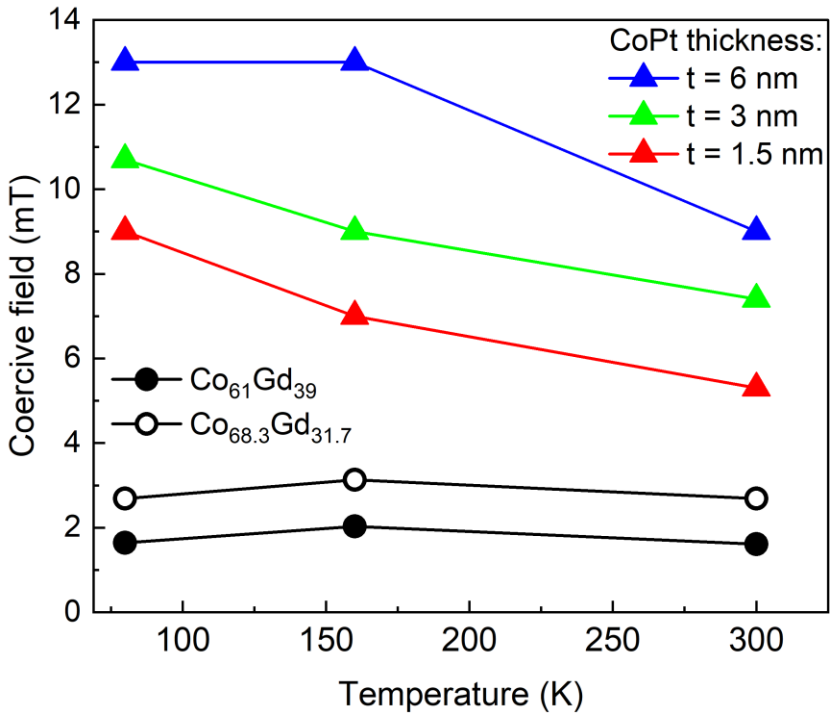

Figure 4.13: Variation of H_C as a function of temperature for different CoPt thicknesses (t = 1.5 nm (red), 3 nm (green), 6 nm (blue) and Co_xGd_{100-x} alloy ($Co_{61}Gd_{39}$ (solid circle), $Co_{68.3}Gd_{31.7}$ (open circles)).

Therefore, all the above XMCD measurements helped to identify the suitable sample for the SPHE study based on CoGd alloy systems. Both CoGd alloys seemed appropriate at this stage of preparation, so we favored both concentration alloys for our first slicing experiments with 3 nm of CoPt film.

4.3.2.3 Identification of anisotropy axis

In the SPHE study, we aim to study the response of spin current on the bottom magnetic layer, i.e., CoGd alloys. To distinguish the spin current contribution from conventional thermal dynamics, we measure the pump-probe experiment in P and AP configuration (as explained in the section 4.3.2) by saturating the CoGd layer by applying magnetic field value, which is sufficient enough to saturate the CoGd layer without changing CoPt.

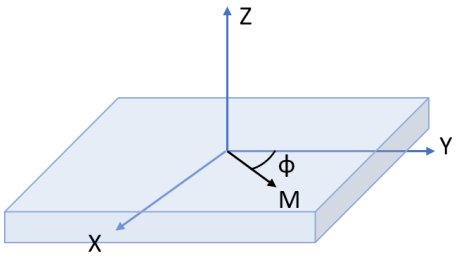

Figure 4.14: Schematic of sample geometry for MOKE. ϕ is the angle defining the direction of the applied magnetic field.

It is known that CoGd alloys display in-plane uni-axial magnetic anisotropy [98]. Therefore, we have to identify this easy axis and to align it with the magnetic field to ensure magnetic saturation during the pump-probe experiments.

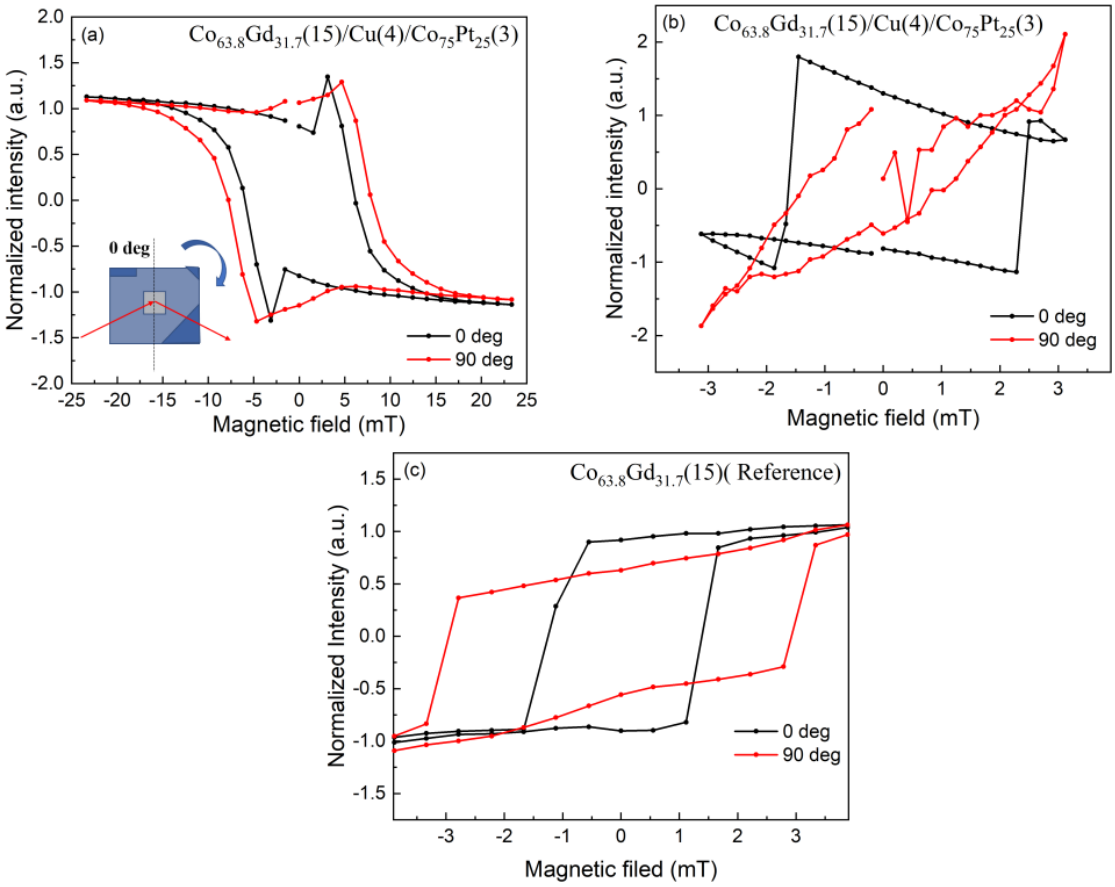

Figure 4.15: Angle dependence MOKE to identify in-plane anisotropy axis. (a) shows the full hysteresis (± 25 mT) of CoGd (15)/Cu (4)/CoPt (3 nm) at angles 0 ° (black) and 90 °(red). (b) Minor loop recorded by sweeping magnetic field (± 3 mT) shows the hysteresis of CoGd (soft magnetic layer). (c) Hysteresis loop of the reference sample (only CoGd layer) to compare with Figure b.

We performed the MOKE measurement by rotating the sample by an angle ϕ (as shown in Fig 4.14) with respect to the magnetic field direction. Figure 4.15 shows the hysteresis at two angles ϕ = 0° (black) and 90 ° (red) for two samples (a,b) CoGd/Cu(4)/CoPt(3) and (c) CoGd (15 nm) reference layer. Figure 4.15 (a) shows the full hysteresis of bilayers at angles 0 and 90 °. Similar to XMCD, the MOKE signal also showed the contribution of both magnetic layers. We observed the broadening of hysteresis at 90 °. To confirm the anisotropy in CoGd, the minor loop was also recorded to see the hysteresis only of the bottom CoGd layer. Furthermore, to compare the minor loop and ensure that CoGd exhibits uniaxial anisotropy, we recorded the hysteresis as a function of angle for the reference sample without CoPt (Fig. 4.15 (c)). The square hysteresis loop at 0 ° shows lower H_C = 2 mT. However, at 90 ° H_C, it is very large and reaches saturation only after 3.5 mT. The existence of this uniaxial anisotropy is not clear in our case, but it has been reported previously in many works [99,100]. They interpreted the presence of magnetic anisotropy to the deposition geometry [101]. However, in our case, the substrate holder was rotating during deposition, therefore, we didn't expect the existence of any in-plane anisotropic axis. So, the origin of in-plane anisotropy is not known so far.

4.4 Conclusion

This chapter showed the sample optimization for spin-polarized hot electron study. To measure the SPHE-induced ultrafast dynamics at the femtoslicing beamline as described in section 3.1.2. A limited time period of each beamtime and experimental condition at slicing doesn't allow to try different samples. Therefore, optimizing the sample and finding the experimental conditions beforehand, such as compensation temperature (TM), anisotropy axis, and coercive field, is crucial.

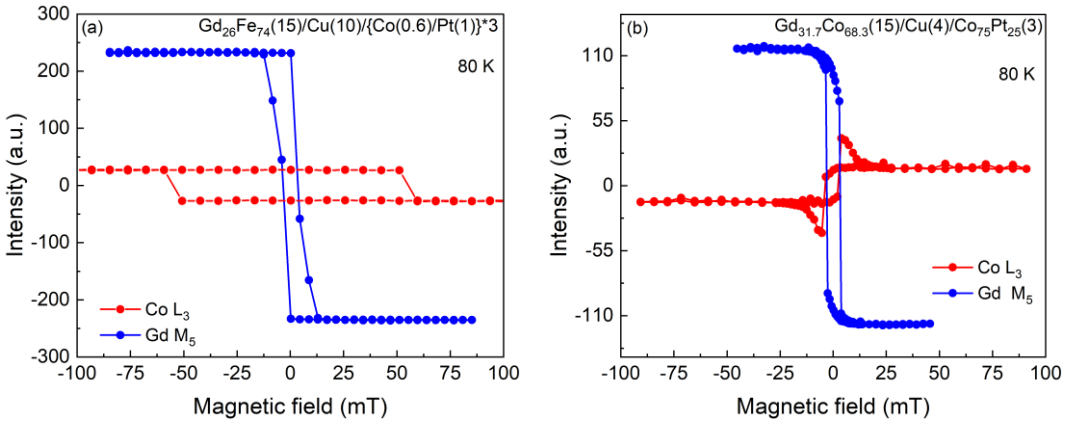

*Figure 4.16: Hysteresis of composition and thickness used for SPHE study. (a) S4: $Gd_{26}Fe_{74}$(15)/Cu(10)/{Co(0.6)/Pt(1)}*3 (b) $Co_{68.3}Gd_{31.7}$(15)/Cu(4)/$Co_{75}Pt_{25}$(3) at Co L_3 (red) and Gd M_5 (blue) edge at T = 80 K.*

$FeGd_{26}$(15)/Cu (10)/ {Co (0.6)/Pt (1)}*3 (S4) is used to study the SPHE effect a Fe L_3 and Gd M_5 edge at T_{cryo} = 80 K. This sample structure allowed to probe the dynamics of iterant 3d Fe electrons as well as localized 4f electrons of Gd. The hysteresis at Co L_3 and Gd M_5 (Fig. 4.16 (a)) shows that the bottom layer (FeGd) can be switched by applying a very small magnetic field (~15mT) without flipping the Co/Pt layer. Similarly, $Co_{68.3(61)}Gd_{31.8(39)}$ (15)/Cu(4)/$Co_{75}Pt_{25}$ (3) is used (Fig. 4.16(b)) for SPHE study.

Chapter 5 Spin-Polarized hot-electron induced dynamics in FeGd alloy system

This chapter will discuss the hot electron (HE) and the spin-polarized hot electron (SPHE) induced ultrafast 3d and 4f spin dynamics in a ferrimagnetic FeGd alloy layer. My main objective is to evidence the impact of spin polarization of the hot-electron currents used as a pump to excite the alloy. This work combines experimental results obtained utilizing time-resolved XMCD and cutting-edge theoretical description-based Atomic spin dynamics simulations. The TR-XMCD measurements presented in this chapter were all performed using the pump-probe experimental set-up at the femtoslicing beamline at BESSY II, Berlin (explained in section 3.1.2), while the numerical simulation performed by Maryna Pankratova from O. Eriksson's group at Uppsala University, Sweden. The combined experimental and theoretical outcomes allowed us to estimate many parameters, such as the duration of the HE pulses, the demagnetization time(s), and the degree of spin polarization.

In this chapter, I discuss the SPHE-induced effect on the out-of-plane $Fe_{74}Gd_{26}$ /Cu/(Co/Pt) based spin valve structure. As explained in the previous chapter (Sec.4.1), the experimental identification of SPHE-induced 3d and 4f spin dynamics requires measuring the transient XMCD at the Fe L_3 and Gd M_5 edges in two different magnetic configurations of the spin valve. So, the 4 sets of pump-probe delay scans are required to get the desired information. Due to the limited photon flux at the femtoslicing beamline, long accumulation times are needed to obtain satisfying statistics. Therefore, it was very important to have optimal experimental conditions before conducting dynamics measurement. Experimental parameters were set by characterizing and optimizing the spin valve structure, using MOKE and element-selective XMCD measurements as a function of temperature and composition (discussed in section 4.3.1). Another crucial point consisted of finding the optimal pump-probe conditions: cryostat temperature, magnetic field intensity, laser fluence, and the best delay scan ranges, which were unknown.

This chapter will start with a brief review of the main magnetic properties of the selected sample. I will be focusing only on a few characterization results in section 5.1, mainly related to the $Fe_{74}Gd_{26}$ (15) / Cu (10)/ {Co (0.6)/Pt (1)*3} spin valve structure. Time-resolved experimental data are explained in section 5.2, followed by the description of the theoretical model and the result in section 5.3.

5.1 Experimental details

This section will begin with the sample structure used in this work. I will describe the magnetic properties of the sample during the pump-probe experiments. Subsequently, the optimization of experimental conditions for time-resolved experiments will be discussed, which were made initially by using the ps mode before switching to the femtoslicing operation mode.

5.1.1 Sample structure

We used the following sample: SiN/Ta (5) /Cu (20)/Ta (5) / $Fe_{74}Gd_{26}$ (15) /Cu (10) / {Co (0.6)/Pt (1)*3}/Cu (60) /Pt (6), having out of plane anisotropy axis (Fig. 5.1(a)). This sample structure is optimized to generate hot electrons (HE) in the top Pt capping layer. Subsequently, these HEs get polarized upon passing through the first magnetic layer, Co/Pt (the spin polarizer). The resulting spin-polarized hot electrons (SPHE) interact with the underlying magnetic layer, $Fe_{74}Gd_{26}$ (detector layer). Figure 5.1 (b) shows the hysteresis measured at Co and Fe L_3 edges, and it illustrates that the Hc of Co/Pt is 5 times higher than the $Fe_{74}Gd_{26}$ layer, as needed to stabilize both magnetic configurations in the spin valve (parallel and antiparallel). Since at T=80K, we get the largest difference between Hc (Co/Pt) and Hc ($Fe_{74}Gd_{26}$), the pump-probe TR-XMCD experiments were performed at low temperature of T = 80K. At high fields (H > Hc(CoPt)), the magnetization of the Co/Pt is antiparallel to that of the Fe sublattice of $Fe_{74}Gd_{26}$, and this configuration is labeled as the anti-parallel (AP, Fig. 5.1 c). The magnetization of the Fe sublattice can alternatively be aligned parallel to Co/Pt by applying a moderate field (Hc ($Fe_{74}Gd_{26}$) < H < Hc (CoPt)) and labeled this configuration as parallel (P, Fig. 5.1 c).

To distinguish the SPHE effect from the general thermal demagnetization curve, we measured the transient XMCD in P and AP two configurations (as explained in previous paragraph) (Fig. 5.1 (c)).

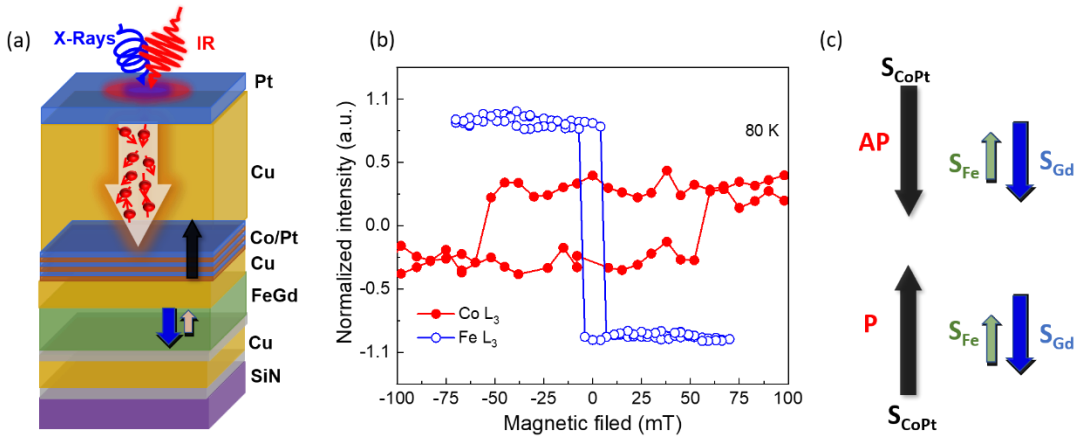

*Figure 5.1: (a) Sample structure used to study the spin-polarized hot electron (SPHE) induced dynamics: SiN/Ta (5) /Cu (20)/Ta (5) / $Fe_{74}Gd_{26}$ (15) /Cu (10) / {Co (0.6)/Pt (1)*3}/Cu (60) /Pt (6). The thickness of each layer in the bracket is in nm. Here, the red pulse represents the IR laser (800 nm) of 60 fs duration acting as a pump, and the blue pulse represents the circularly polarized X-ray pulses of 100 fs duration as a probe. Both pulses are separated by 1°. The large arrow represents the direction of hot electrons flow, and inside, the short red arrow with a circle represents the non-polarized hot electrons. Cu (60) ensures the complete absorption of the IR pulse; therefore, the bottom Co/Pt layer is excited through HE pulses only. Consequently, those HE pulses generate spin-polarized current (SPHE) from Co/Pt. After crossing the spacer layer, the spin current interacts with the FeGd layer, on which the response of SPHEs is recorded. (b) Hysteresis measured at Co L_3 and Fe L_3 edges at t = 80 K, and it shows that the Hc of Co/Pt (50 mT) is larger than FeGd (~ 10 mT). (c) Parallel (P) and Antiparallel (AP) experimental scheme: The green and blue arrows represent the Fe and Gd spin moment orientation. AP and P define the relative orientations of the magnetization between Co and Fe spin moments in {Co (0.6)/Pt (1)*3} and $Fe_{74}Gd_{26}$, respectively.*

5.1.2 Optimization of Laser fluence

At the femtoslicing beamline, we can utilize both the "normal" X-ray pulses in hybrid mode (~60 ps) and the ultrashort X-ray pulses in femtoslicing mode (~100 fs) (Sec. 3.1.2). Since the former provides high photon flux (~10^9 - 10^{10} photons/sec) compared to the latter (~10^5 – 10^6 photons/sec), the optimization of experimental conditions has been performed by using the hybrid mode to get fast data acquisition and reasonable signal-to-noise ratio.

Therefore, we have recorded the transient XMCD as a function of the pump-probe delay in the ps mode for various IR laser fluences at T=80K. The objective was to estimate the demagnetization amplitude as a function of laser fluence since we need to measure TR-XMCD for the P and AP configurations both in the low- and high-excitation regimes for comparison with the

theoretical model. It also consists of determining the sample's damage threshold under laser irradiation. The data are displayed in Figure 5.2(a). During the pump-probe experiments, the IR laser spot size was 460 × 375 μm² (H×V), and the X-ray spot was 100×50 μm² (H×V). This ensures the homogenous pump effect during the measurement. The un-pumped XMCD (not shown) and the substantial recovery observed at a longer time scale for all fluences ensure the full recovery of the magnetization between two successive IR pump pulses.

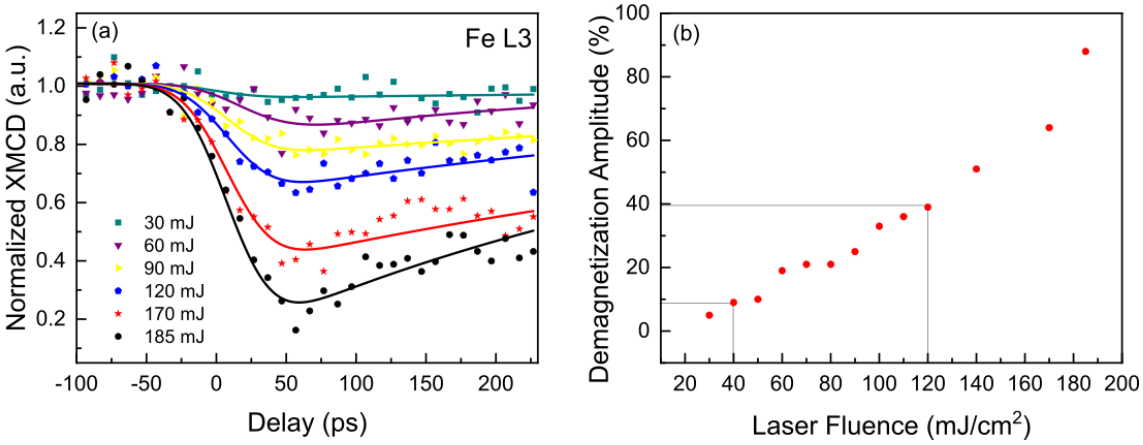

Figure 5.2: (a) Demagnetization dynamics measured at Fe L3 edges as a function of fluence at T=80 K, using hybrid mode (picosecond (ps) mode) with 60 ps time resolution. The solid lines represent the double exponential fit with Gaussian convolution, considering the 60 ps pulse shape. (b) Variation of demagnetization amplitude with the incidence laser fluence. Demag. Amplitude is obtained by the fitted values, and it exhibits a linear trend up to 180 mJ/cm² incidence fluence. Note: Demagnetization amplitude in ps mode is lower than the femtosecond resolution dynamics.

We estimated the demagnetization amplitude by fitting the TR-XMCD curves with a double exponential function convolves with a Gaussian. Figure 5.2 (b) displays the demagnetization amplitude's dependence on fluence. This graph shows a linear variation of demagnetization up to 180 mJ/cm², for which a demagnetization of ~65% is reached. We know that in hybrid mode, the demagnetization amplitude is largely underestimated compared with the slicing mode because of the different time resolutions in both modes. Therefore, we can reach almost full demagnetization in the explored fluence range.

However, above 140 mJ/cm², the membrane which contained the sample was broken after only 2-3 hours. We finally select two fluences well below the damage threshold for the TR-XMCD in femtoslicing mode, 40 mJ/cm² (low excitation regime) and 120 mJ/cm² (high excitation regime), for which demagnetization amplitude of 15 % and 38 % respectively in hybrid mode.

5.1.3 Estimation of sample temperature during pump-probe experiment

Time-resolved XMCD measurements were performed at the cryostat temperature of 80 K. Due to limited photon flux during slicing mode, it's not possible to measure the hysteresis as a function of pump-probe delay. Therefore, in order to examine the sample temperature during the pump-probe experiment, we measured the time-resolved hysteresis using X-ray pulses of duration ~50 ps in the normal synchrotron mode, before switching to the femto-slicing mode. Figure 5.3 (a) shows the hysteresis measured with Laser off and Laser on at t = 50 picoseconds (ps).

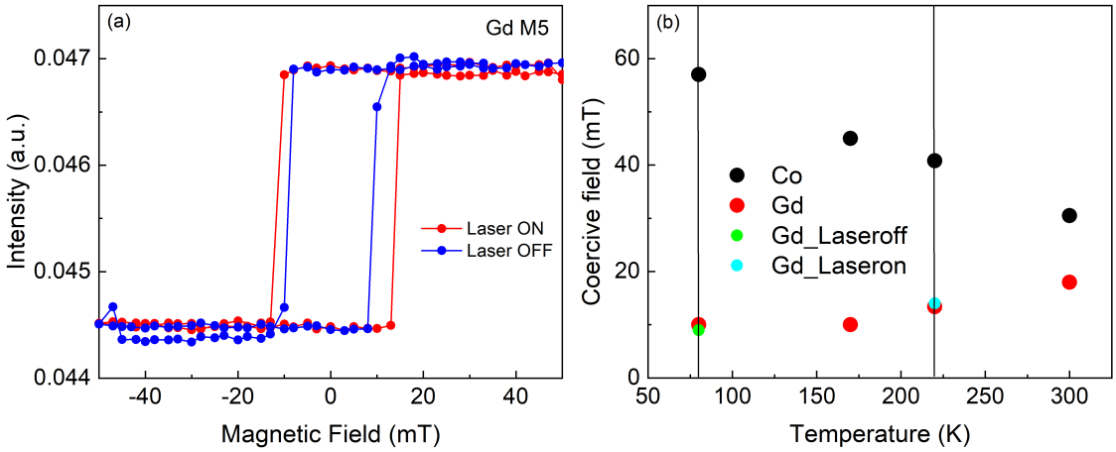

Figure 5.3: (a) Hysteresis recorded at the Gd M_5 edge with (fl = 40 mJ/cm²) and without the laser at a delay of t = +50 ps. (b) Coercive field (black and red points) as a function of temperature at the Co L3 and Gd M_5 edges. Green and cyan points show the coercive field measured at the Gd M_5 edges without and with laser (at the delay of t = +50 ps). It shows that the coercive field at Gd M_5 with laser matches the static coercive field at T = 220 K. This temperature is equivalent to lattice temperature after thermal equilibrium.

By comparing the coercive field values from the static measurement data (as explained in section 4.3.1) at Co L_3 (black squares) and Gd M_5 (Red dots) edges in Figure 5.3 (b), the temperature at the delay, t = 50 ps, is equal to 220 K (represented by the cyan color dot in Figure 5.3 (b)). This temperature is equivalent to the transient lattice temperature after thermal equilibration.

After finding the optimal experimental conditions, we switched to femto-slicing mode. The time-resolved XMCD measurements in femtoslicing mode will be given in the next section.

5.2 Study of spin-polarized hot electron (SPHE) induced dynamics by Tr-XMCD: Experiment

To investigate the impact of spin-polarized hot electrons (SPHEs) on $Fe_{74}Gd_{26}$, we performed the Tr-XMCD measurements at Fe L_3 and Gd M_5 edges using femto-slicing mode at T_{cryo} = 80K for laser fluences of 40 and 120 mJ/cm² with sub-picosecond temporal resolution [86]. All the pump-probe measurements were performed at Cryostat temperature (T_{cryo}) = 80 K so that Hc(Co/Pt) >> Hc($Fe_{74}Gd_{26}$) (Fig. 5.3 b).

The protocol to measure the TR-XMCD in the AP configuration is straightforward since it is sufficient to apply a magnetic field H > Hc(Co/Pt) and record the transient transmission for +H and -H.

For the P configuration, we first set the Co/Pt magnetization direction by applying a strong magnetic field +H which is then switched off. Then, we used a weak magnetic field -H < Hc (Co/Pt) sufficient to align the magnetization of the $Fe_{74}Gd_{26}$ layer. We record the transient transmission. Then, we repeat the measurement with -H and +H to get TR-XMCD in the P configuration.

5.2.1 Dynamics at incident IR fluence 40 mJ/cm²

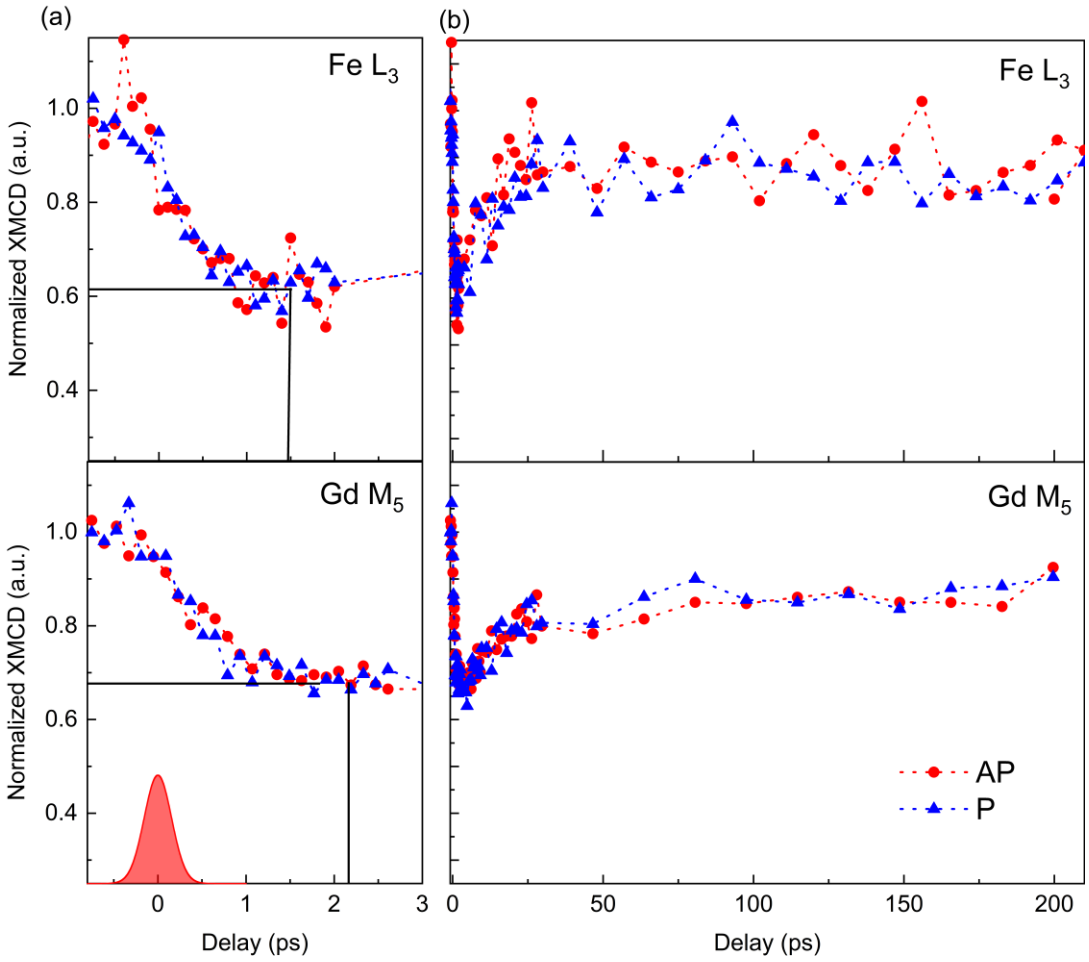

Figure 5.4: The measurements are done in two configurations: Magnetization of Co is parallel (P) (blue curve) and Antiparallel (AP) (red curve) to Fe magnetization at incidence Laser fluence = 40 mJ/cm² at Tcryo = 80 K. (a) shows the dynamics measured at Fe L_3 and Gd M_5 for short delay range, and (b) for the long delay range. Vertical and horizontal solid lines are drawn to illustrate the maximum demagnetization time and amplitude in the case of Fe 3d and Gd 4f. XMCD at negative delay is normalized to 1. The red Gaussian curve represents the hot electron pulse duration.

In Figure 5.4, we show the Tr-XMCD measurement at the Fe L_3 and Gd M_5 edges in the P (blue) and AP (red) configuration (as explained in section 5.1) for IR incidence fluence 40mJ/cm² at cryostat temperature of 80K. All data are normalized at a negative delay to 1 by using the method described in section 3.1.3.

We observe That the TR-XMCD curves are identical in the P and AP configurations, which rule out any signature of SPHE effects. This can be due to the experimental noise level, which is too large to visualize such small effects. Indeed, previous experiments have reported on SPHE effects in the order of a few % [6]. It can also be due to the low-excitation regime as predicted by the theoretical model developed by M. Pankratova, discussed further in section 5.3.

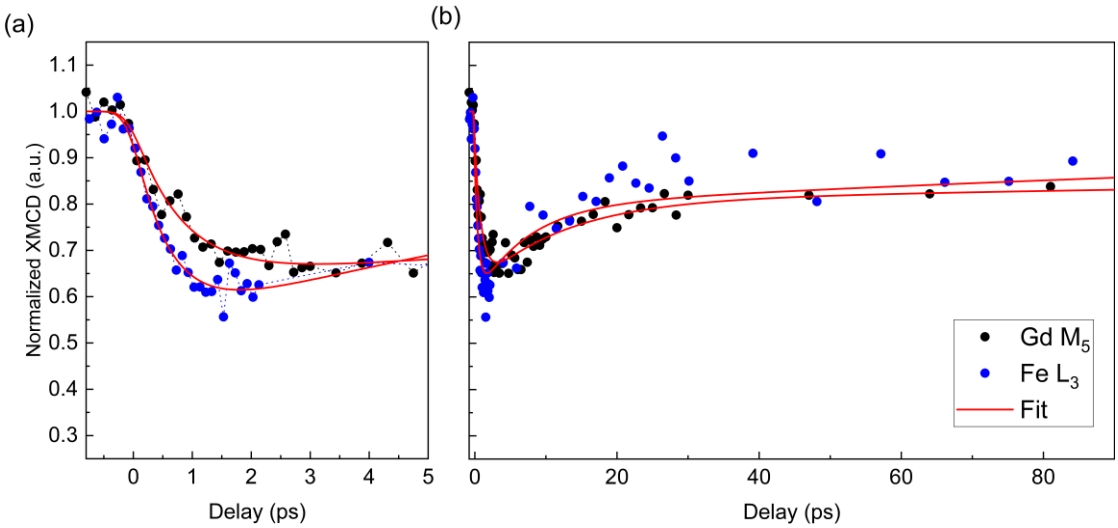

Figure 5.5: Hot electron induced dynamics at the Fe L_3(blue) and Gd M_5 (black) edges at incidence Laser fluence of 40 mJ/cm² at T_{cryo}=80 K (a) short delay upto 5 ps, (b) long delay range upto 100 ps. These graphs were obtained from Figure 5.4 by averaging the data for P and AP. Solid lines are double exponential fits with Gaussian convolution.

Although we could not observe any SPHE-induced spin dynamics for this fluence, the investigation of the hot-electron induced demagnetization of the Fe and Gd sublattices allows for extracting valuable information regarding the SPHE pulses themselves. The HE-induced demagnetization is obtained by averaging the data for P and AP at both edges (Fig. 5.5).

The fitted parameters for Fe and Gd are summarized in this table:

Parameters	Fe	Gd
HE Pulse duration (G(t)) (fs)	424 ± 80	424
Demag. Amplitude (A) (%)	47 ± 1	37 ± 0.9
Characteristic time (τ_d) (fs)	628 ± 12 [175] *	892 ± 63 [550] *
Recovery (t_{r1}) (ps)	12 ± 0.62	36 ± 4.56
Recovery (t_{r2}) (ps)	279 ± 75.8	814 ± 365.44

*Table 5.1: Fitted parameters obtained by using the equation (in appendix) for the average dynamics of P and AP configuration measured at Fe L_3 and Gd M_5 edges. *Compared with the demagnetization time measured from direct IR excitation of $Fe_{66}Co_9Gd_{25}$ alloy (~40 % demagnetization) in square bracket (taken from ref. [23]).*

These curves are fitted with a double exponential function convolved by a Gaussian to consider the pulse duration (solid lines). All the fix and free parameters of the fitting function are listed in table 5.1. We kept t_0 and y_0 fixed to minimize the number of free fitting parameters. The Gaussian accounts for the experimental time-resolution. However, although in direct IR induced demagnetization, the Gaussian width is set to 130 fs, we cannot use it in the case

of HE induced demagnetization [41,45]. Therefore, we have considered the width of the Gaussian convolution G(t) as a free parameter.

From the fitting procedure, we evidence a slightly larger demagnetization amplitude for the Fe sublattice (~47%) compared to that of the Gd sublattice (~37%). The Gd sublattice shows a slower dynamic compared to that of the Fe sublattice. These characteristics for the relative demagnetization amplitudes and demagnetization times are qualitatively consistent, as reported by Radu et al. in a similar $Fe_{66}Co_9Gd_{25}$ alloy system by direct IR excitation in [23]. However, we obtained characteristic demagnetization times of 628 fs and 892 fs for the Fe and Gd sublattices, respectively, instead of the 175 fs and 550 fs characteristic times they have reported in case of approximatively 40% demagnetization of the Fe and Gd sublattices. We note that their alloy contains 9% Co, which may probably change the spin dynamics compared to our $Fe_{74}Gd_{26}$ alloy. However, it will be shown in the next chapter that the Gd 4f spin-dynamics is slower in CoGd than in FeGd alloys. Therefore, we rule out the adjunction of Co to explain the much slower dynamics we have reported.

Instead, we infer that the longer demagnetization times can be explained by considering the width of 424 fs for the Gaussian convolution (detail of Gaussian pulse estimation is given in appendix). This large value, obtained by the fitting of our data, can be interpreted as a stretching of the HE pulses caused by the transport through several layers. Although Bergeard et al. have shown that the elongation of the HE pulses generated in a Pt(6)/Cu(60) bi-layer shouldn't be more than 30 fs with respect to the IR pulse duration [39,40]. Ferté et al. have shown that inserting [Co/Ni](3.5) [41] or Pt(10) [45] layers in the HE path led to dramatic elongation of the characteristic demagnetization times. Indeed, the thermalization of HE in these layers drastically slowdown the electron by passing from ballistic (~1 nm/fs) to diffusive (~0.01 nm/fs) propagation regimes. Vodungbo et al. also obtained identical results [38]. In our spin valve, we suppose that the Gaussian width of 424 fs comes from the HE pulse elongation caused by the propagation through the [Co(0.6)/Pt(1)]*3 layers. We believe this layer is thick enough to thermalize the HE distribution [41,45]. Future measurements with thinner spin-polarizer layers are needed to verify our claims. We also wonder whether the thermalization of HE pulses affects the degree of SP, which could explain the absence of SPHE effects in our measurements. To conclude, the "long" demagnetization times we have reported for both Fe and Gd sublattices are caused by the stretching of the HE electron pulses and their diffusive transport through the FeGd alloys in line with Ferté et al. [41,45].

5.2.2 Dynamics at incidence fluence of 120 mJ/cm²

We performed the same measurements at a higher fluence of 120 mJ/cm² using similar experimental conditions. Due to technical issues during the beamtime, we couldn't measure the dynamics at both edges using the very same experimental conditions. Therefore, our results are limited to only Fe L_3 edge for P and AP cases. We recorded the change in XMCD at the Fe L_3 edge in P (blue) and AP (red) configurations, shown in Figure 5.6. The values at negative delays are normalized to 1.

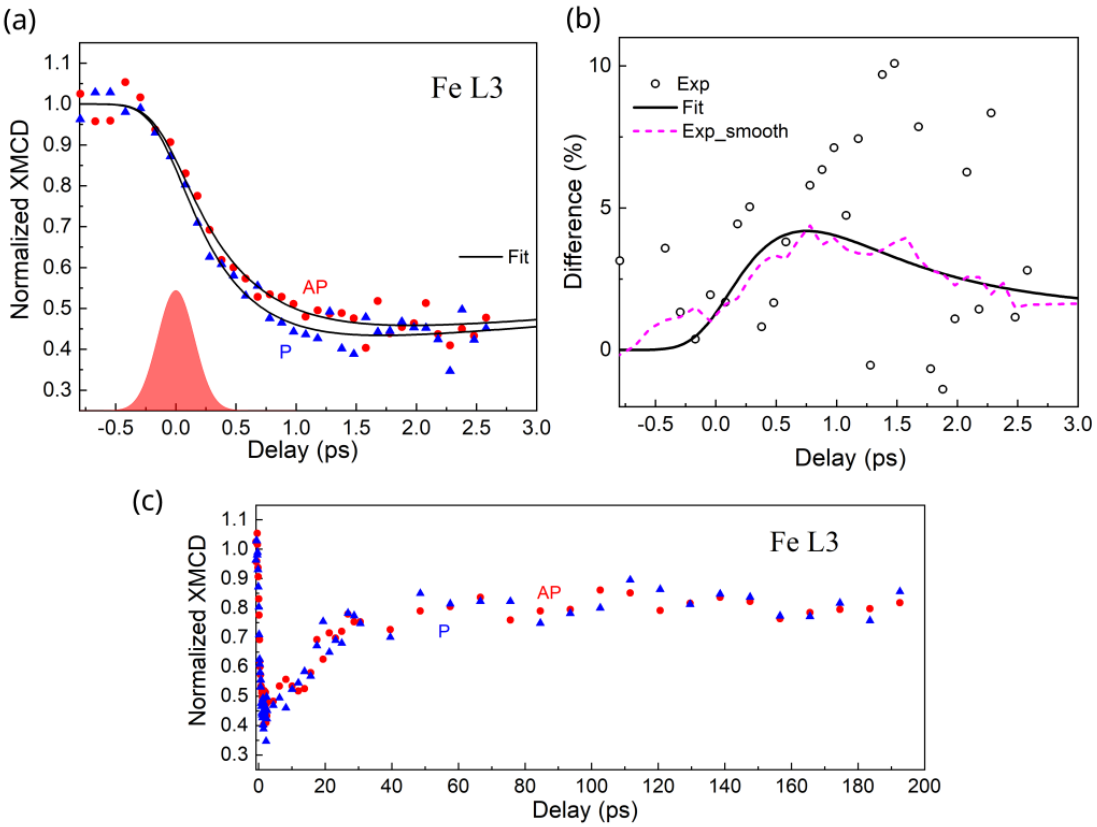

Figure 5.6: TR- XMCD as a function of pump-probe delay at Fe L_3 at the incidence Laser fluence of 120 mJ/cm² at T cryo = 80K for two configurations: P (blue) and AP (red). (a) represents the dynamics at a short time scale up to 3 ps, and solid lines are the exponential fits. The red Gaussian curve represents the SPHE pulse shape arriving at FeGd. (b) Normalized difference of the demagnetization dynamics obtained at P and AP configuration (by open dots) and superposed with the smoothed data (Magenta dash lines). The solid black line is the difference of fitted data. (c) Dynamics at a long time scale. SP effect vanishes below the detection limit defined by a large signal to noise ratio after 2 ps, and both dynamics converge and recover at the same level at 100 ps.

Figure 5.6 (a) shows the dynamics at a short time scale up to 3 ps. We observed that dynamics in the case of the P configuration is faster and slightly larger in amplitude than the AP configuration. This means that experimentally, we have accelerated demagnetization dynamics in the case of parallel

magnetization directions of Co and Fe (P case) and decelerated demagnetization dynamics in the case AP. The dynamics obtained in case P and AP are fitted by double exponential with Gaussian convolution and represented by the solid lines.
The fitted parameters for both the configurations are summarized in this table:

Parameters	P configuration	AP configuration
HE Pulse duration (G(t)) (fs)	424 ± 80	424 ± 0
Demag. Amplitude (A) (%)	63 ± 4	60 ± 3
Characteristic time (τ_d) (fs)	473 ± 80	550 ± 50
Recovery (t_r) (ps)	23 ± 11	21.81 ± 10

Table 5.2: Fitted parameters were obtained from the fitting equation given in the appendix for the P and AP configuration measured at the Fe L_3 edge.

From the fits, we obtained demagnetization times of 473 ± 80 fs and 550 ± 50 fs for P and AP cases, respectively, as well as demagnetization amplitudes of 63 ± 4 % and 60 ± 3 %. Even if these parameters extracted from the fit functions seem close when considering the large error bars, the systematic separation of our data point along the dynamics up to 2 ps ensures that the difference is real. This observation is strengthened by the fact that both TR-XMCD curves merge at delay t > 5 ps, and both TR-XMCD shows identical recoveries (Fig. 5.6 (c)). To highlight the difference between the Fe 3d spin dynamics in P and AP configurations, we show the normalized differences between the experimental TR-XMCD curves and the fitting function in Figure 5.6 (b).

We claim that this difference between the P and AP configuration observed in the TR-XMCD curves corresponds to the signature of the SPHE-induced Fe 3d spin dynamics in ferrimagnetic $Fe_{74}Gd_{26}$.

Indeed, in Figure 5.6 (b), we notice that these effects start as soon as the HE pulses excite the film at t=0 and that the maximum of the SPHE induced effect (~ t= 0.6 ps) corresponds to the ending of the HE pulses. By comparing the duration of the SPHE effects with the HE pulses duration (424 fs), we highlight that the spin-induced effects last up to t = 2.5 ps, i.e., much longer than the temporal. This duration reflects the mean free path and lifetime of these SPHE pulses in the FeGd film[12]. These experimental observations confirm that spin currents are generated through the HE induced excitation of the ferromagnetic Co/Pt layer and propagated towards $Fe_{74}Gd_{26}$. Lichtenberg et al. has shown that the amplitude of photoexcited spin currents depends on the laser fluence and the time derivative of laser-induced demagnetization (dM/dt) [102]. By speculating that in our case, the spin currents are mainly generated by the HE induced demagnetization of the CoPt layers (and not by

the spin-filtering effect), and based on Lichtenberg's claims, we can explain the absence of SPHE effects in the case of a low-excitation regime (Section 5.2.1).

However, the most striking outcome of our experimental observation is that the larger demagnetization is observed for the P configuration, i.e., when the magnetization of the Fe and Co sublattices are aligned in the same direction which is in apparent contradiction with previous works done on ferromagnetic 3d TM based spin valve structures, i.e., CoPt/Ru/CoPt [3] and Fe/Ru/Ni [6]. In both cases, they observed larger demagnetization in the case, when the magnetization of the 3d magnetic layers is antiparallel. We hint with the fact that the measurements were performed below the temperature of magnetic compensation could be responsible for such discrepancy, even if it is counter-intuitive because of the localization of Gd 4f spins (which are not directly excited by the SPHE pulses) and of the conduction band (which is directly excited by SPHE pulses) mainly occupied with Fe 3d electrons. It is worth noticing that Igarashi et al. have recently shown another similar counter-intuitive spin-induced effect [7]. They started from a spin-valve with two aligned ferromagnetic Co/Pt layers. By photoexciting an fs spin current in the top Co/Pt layers, they were able to switch the magnetization in the bottom layer to end up with an antiparallel configuration of the magnetization. We infer that our experimental observations could be related to their observation.

To go further in analysis, theoretical modeling is definitively mandatory. In this direction, our collaborator, Maryna Pankratova from the O. Eriksson group (Uppsala University), has developed a theoretical model based on atomistic spin dynamics simulation [51]. A brief description of the model and the comparison with our experimental observations are given in the next section.

5.3 Study of spin-polarized hot electron induced dynamics by atomistic spin dynamics: Theoretical approach

5.3.1 Atomistic spin dynamic

To study the ultrafast demagnetization dynamics of $Fe_{74}Gd_{26}$, atomistic spin dynamic simulations [51] were performed*. To model the experimental results for $Fe_{74}Gd_{26}$, a heterogenous simulation cell consisting of 1600 atoms was created. Experimentally, it was shown that the concentration of Fe and Gd varies in an amorphous FeGdCo alloy system [103]. By considering this chemical inhomogeneity in such alloys, the amorphous $Fe_{74}Gd_{26}$ alloy was created with the average concentration of $Fe_{74}Gd_{26}$ with some area of 6% rich in Fe and some with 6 % rich in Gd [50].

In these simulations, the increase in electronic temperature is taken into account by using the 3TM model [19], which allows heat to flow among three thermalized reservoirs coupled by electron-spin (G_{es}), electron-lattice (G_{ep}), and spin-lattice (G_{sp}) coupling coefficients. Here, HE pulses are used to excite the system. Therefore, a rise in electronic temperature by HE pulses results in the increase of the spin and lattice temperature by these coupling constants.

In their simulations, they combine the 3TM model with the Landau-Lifshits-Gilbert (LLG) equation:

$$\frac{d\boldsymbol{m_i}}{dt} = -\frac{\gamma}{1+\alpha^2}\boldsymbol{m_i} \times (\boldsymbol{B_i} + \boldsymbol{B_i^{fl}}) - \frac{\gamma}{(1+\alpha^2)}\frac{\alpha}{m_i}\boldsymbol{m_i} \times (\boldsymbol{m_i} \times (\boldsymbol{B_i} + \boldsymbol{B_i^{fl}}))$$

Where m_i represents the atomic magnetic moment, γ is the gyromagnetic ratio. $B_i^{fl}(t)$ is a stochastic field with the Gaussian distribution, whose magnitude is related to the Gilbert damping parameter α, and brings the system into thermal equilibrium. The effective field $\vec{B}_i$, experience by each atom is calculated by the partial derivative of the Hamiltonian $\mathcal{H}$ with respect to the magnetic moment m_i,

$$B_i = -\frac{\partial \mathcal{H}^{eff}}{\partial m_i}$$

Where H^{eff} is an effective spin Hamiltonian that contains contributions from all the interactions:

$$\mathcal{H}^{eff} = H_{iex} + H_{ani} + H_{ext} + \cdots$$

H_{iex} is the interatomic exchange interaction determined for our $Fe_{74}Gd_{26}$ disordered alloy, H_{ani} is the anisotropy energy, and H_{ext} is the applied external field.

In this simulation, no external field is applied, and the anisotropy of Fe and Gd is neglected. Therefore, B_i is obtained by considering the exchange interaction:

$$H_{iex} = -\frac{1}{2}\sum_{ij} J_{ij}\, \boldsymbol{m_i}.\boldsymbol{m_j}$$

Where J_{ij} is the exchange tensor and strength of the exchange interaction, i and j are the atomic indices.

To implement the effect of spin polarization from Co/Pt, spin transfer torque term [104] was accounted to the LLG equation by adding the following field:

$$\boldsymbol{B}_{STT} = B_{PT}^{STT}(\boldsymbol{p} - \alpha \boldsymbol{m} \times \boldsymbol{p}) + B_{RT}^{STT}(\boldsymbol{m} \times \boldsymbol{p} - \alpha \boldsymbol{p})$$

This field consists of both the precession B_{PT}^{STT} , and relaxation component B_{RT}^{STT}. $\vec{p}$ is the spin polarization vector. The strength of the STT term depends on the injected current density j_e (A/m^2) [104].

For simplicity, in the STT equation, only relaxation component was considered, since, we are interested in the dynamics at fast time scale. Therefore, the simplified STT equation is,

$$\boldsymbol{B_{STT}} = B_{RT}^{STT}(\boldsymbol{m} \times \boldsymbol{p})$$

This STT field is added to the effective field in the LLG equation and hence, finally, LLG equation can be written as:

$$\frac{d\boldsymbol{m_i}}{dt} = -\frac{\gamma}{1+\alpha^2}\boldsymbol{m_i} \times (\boldsymbol{B_i} + \boldsymbol{B_i^{fl}} + \boldsymbol{B_{STT}}) - \frac{\gamma}{(1+\alpha^2)}\frac{\alpha}{m_i}\boldsymbol{m_i} \times (\boldsymbol{m_i} \times (\boldsymbol{B_i} + \boldsymbol{B_i^{fl}} + \boldsymbol{B_{STT}}))$$

5.3.2 Results and discussion

The dynamics were studied separately for Fe and Gd in the case of $Fe_{74}Gd_{26}$ to compare with the experiment results at Fe and Gd edges. The model proposes a combination of two processes: thermal originates due to HE-induced heating of the spin system and a non-thermal spin transfer torque (STT) resulting from spin angular momentum transfer. In this simulation, a hot electron pulse increases the electron temperature in the $Fe_{74}Gd_{26}$ layer. This increase in temperature is accounted for by using the 3TM model [17]. To avoid complexity, during the simulations, all the parameters, such as HE pulses, current density, Gilbert damping (α), and coupling constants (G_{es}, G_{ep}, and G_{sp}) were taken the same for the case of Fe and Gd. Since all these parameters strongly depend on demagnetization amplitude, particularly Gilbert damping [105], this leads to an underestimation/overestimation of Fe and Gd demagnetization amplitude, respectively. Furthermore, for simulating the dynamics of each sublattice, the LLG equation was solved by considering the magnetic moments, i.e., for Fe (2.1 μ_B) and Gd (7.6 μ_B), separately. More importantly, the critical parameters of the exchange interactions used in simulations are taken from ref. [50] and is given for our disordered FeGd alloy. All the parameters, such as current density, polarization, and fluence, were optimized to get good agreement with experimental data (Fig 5.7). The best adjustments of the simulations with our experimental data are performed by considering the 100% spin polarization from the Co/Pt layer with the current density of 0.7×10^{11}A/m^2 (Fig. 5.7). Gilbert damping was taken at 0.1 for both elements.

The simulations define the STT spin current polarization of the hot electrons as "positive" for the antiparallel orientation to the Fe 3d spins. In the following

sections, we will compare our experimental data and the simulations using these definitions.

Note that the calculations include an infinite duration of the STT, whereas in our experiment, the interactions have a finite duration of ~ 1ps.

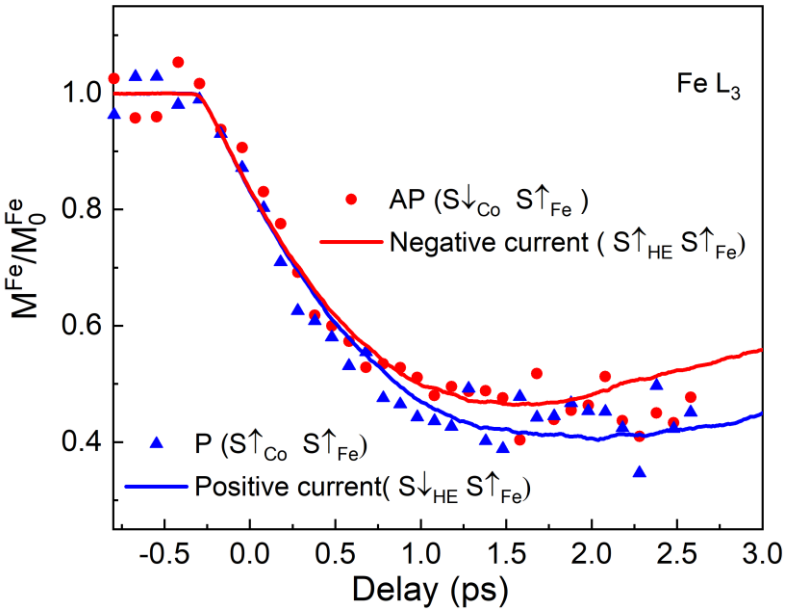

Figure 5.7 Experimental and Simulated demagnetization dynamics by TR-XMCD and atomistic spin dynamics of Fe in $Fe_{74}Gd_{26}$ for 120 mJ/ cm² incident and 3.2 mJ/cm² absorbed fluences. The laser fluence value has been adjusted to fit our experimental data. The blue (red) symbols are the experimental results for the P(AP) configurations. Solid lines in blue (red) are the positive (negative) spin current simulations for a current density J_e of amplitude 0.7 × 10^{11} A/m² and the *Gilbert damping a =0.1. In simulations, SPHE polarization is opposite to the Co moments, shown by the arrow directions in legends.*

Simulations for large IR incident fluence at Fe L_3

Figure 5.7 shows the simulated dynamics (Solid lines) for Fe moments at an absorbed fluence of 3.2 mJ/cm² (theoretical) and compared with the experimental results performed at 120 mJ/cm² (data points).

The simulated dynamics for the Fe sublattice in the case of positive and negative current configuration provide good agreement with the experimental data (Fig. 5.7) by considering the STT impact in addition to the heat-driven magnetization dynamics. We can see that the differences between the P and AP configurations are well reproduced. Simulated demagnetization dynamics match with the experimental data up to 2 ps but overestimate the effect due to the presence of STT through whole magnetization dynamics. This delay defines the time at which we have the maximum difference between P and AP for Fe (Fig. 5.6 b). By comparing the experimental and simulated curves in Figure 5.7,

we notice that the spin polarization of the SPHE shows the opposite sign to the one defined by the Co magnetization in the Co/Pt multilayer. Positive SPHE currents (blue line) are thus found to be antiparallel to the Fe spins, whereas the magnetization in Co is parallel (P) (blue points). This implies that minority spins are coming out from the Co/Pt multilayer.

5.3.2.1 Simulations for low IR incident fluence at Gd M_5

The same simulations were carried out for the Gd for P and AP configurations. Measurements at the Gd edge were performed at a lower fluence (40 mJ/cm²) than the Fe edge (120 mJ/cm²). Therefore, to match the demagnetization amplitude as the experiment, the heat of the hot electron pulse was rescaled by the ratio 0.4, which is close to the experimental measurements (0.33 = 120/40).

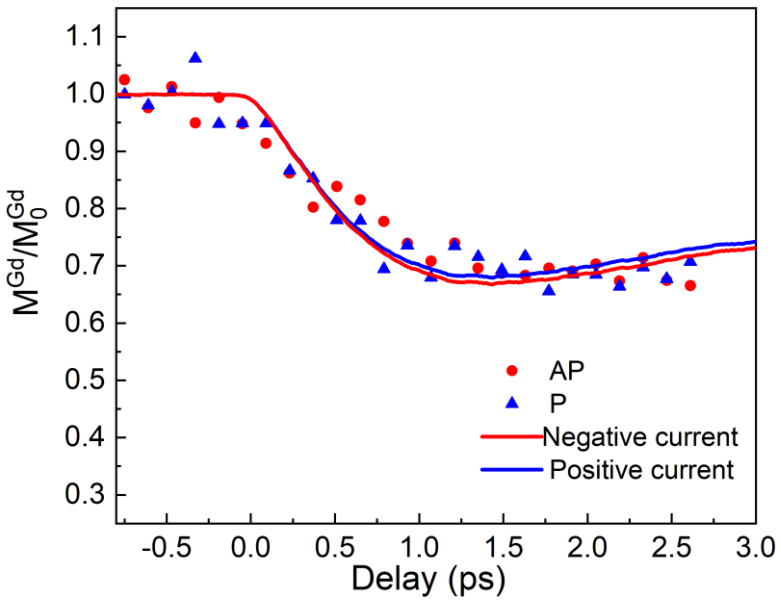

Figure 5.8: Experimental and Simulated demagnetization dynamics by TR-XMCD and atomistic spin dynamics of Gd in $Fe_{74}Gd_{26}$ for 40 mJ/ cm² incident and 1.2 mJ/cm² absorbed fluences. The last fluence has been adjusted to fit our experimental data. The blue (red) symbols and lines are the results for the P (AP) configurations. Solid lines blue (red) are the simulations for the positive (negative) spin current for a current density J_e of amplitude 0.28 × 10^{11} A/m² and the *Gilbert damping a =0.1.*

In the simulation of the GdM_5 data, the STT current density was rescaled by a factor of 0.4 with respect to the IR incident fluences (as explained above) because the theoretical current density is proportional to the spin current fluence. Here, we assume that we are in the linear regime between the incident IR fluence and the final spin currents of SPHE. However, no optimization of the related parameters in the simulations has been performed because of the absence of a spin current effect. The simulations for Gd dynamics were

performed by using a spin current density of 0.28×10^{11} A/m^2. Figure 5.8 shows the calculated dynamics at a theoretical absorbed fluence of 1.2 mJ/cm^2 and compared with the experimental results (40 mJ/cm^2 IR incidence fluence). Simulated dynamics showed good agreement with the experimental results at Gd edge. The difference in P and AP dynamics is thus expected much smaller for Gd than Fe. In order to verify if the absence of effect at GdM_5 is only due to the low fluence used for GdM_5. The simulations were extended for the absorbed fluences of 3.2 mJ/cm^2 and 1.2 mJ/cm^2 for the Fe and Gd sublattices. Figure 5.9 shows the simulated dynamics for the Fe 3d (a,c) and Gd 4f (b,d) at fluence 3.2 and 1.2 mJ/cm^2, respectively. The measurement at high fluence couldn't be performed experimentally at the Gd M5 edge, but the theory predicts that the effect can also be expected at the Gd M5 edge (Fig. 5.9 (b)). We should note that at high fluence (a, b), the predicted SPHE effect is larger in Fe (Fig 5.9 (a)) than in Gd (Fig 5.9(b)).

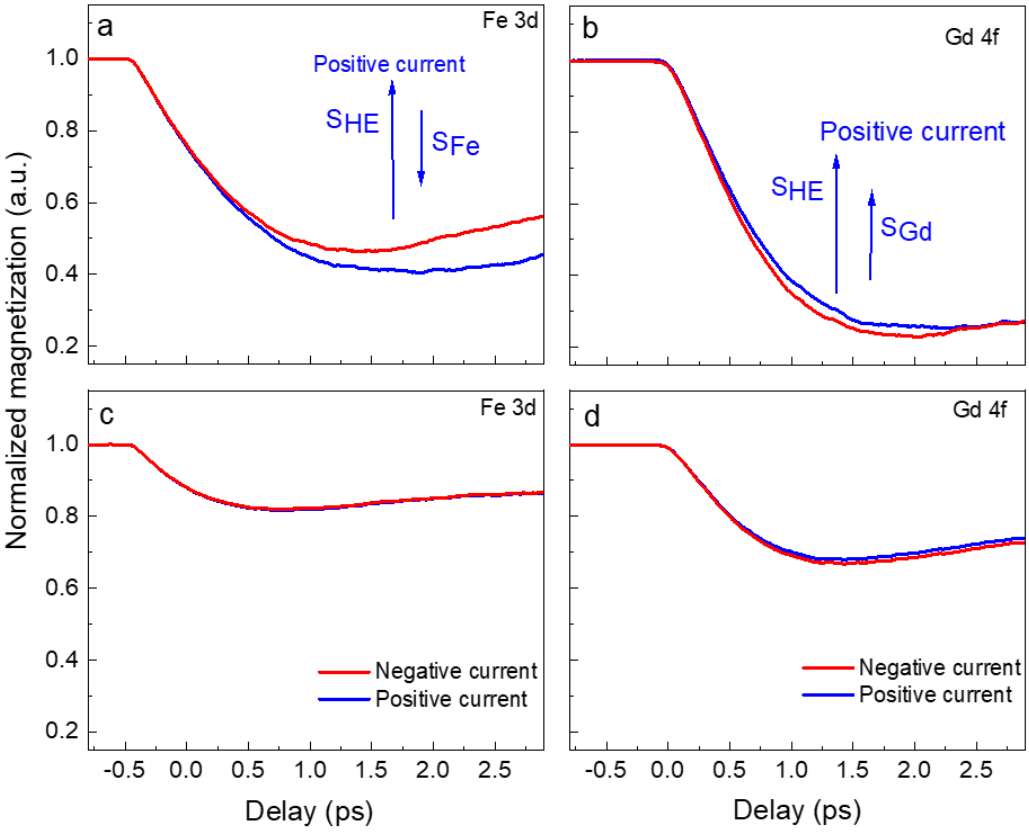

Figure 5.9 *Simulated dynamics by atomistic spin dynamics of Fe (a,c) and Gd (b,d) moments in $Fe_{74}Gd_{26}$ for the two absorbed fluence values (a,b) 3.2 mJ/cm^2 and (c,d) 1.2 mJ/cm^2. The positive SPHE currents lead to the acceleration of the 3dFe and deacceleration of the 4fGd dynamics.*

Based on the simulated dynamics, we can conclude that for Fe 3d, we observed an acceleration in the demagnetization rates when the incoming SPHE current is opposite to the Fe 3d (positive current compared to our data).

For Gd4f, we expect, using the predictions of the simulations, an acceleration in the 4f demagnetization rates when the incoming SPHE current is opposite to the Gd4f spins (negative current). In both sublattices, the STT-induced torque uses antiparallel spin current - spin atomic moment configurations.

Qualitative estimations of the relative effects of Fe and Gd in the FeGd alloy: from the energy point of view

The simulations show a very important trend considering the relative Fe versus Gd demagnetization rates. For the Fe 3d, we observed an acceleration in the demagnetization rates when the incoming SPHE current is opposite to the Fe 3d moments. It is similar for Gd4f, where opposite SPHE spins to 4f moments accelerate the demagnetization rates.

In the simulations, we propose a double contribution to the demagnetization. The first one is the heat driven by the HE energy transfer to the electronic system, whereas the second is provided by the energy transferred by the spin polarization of SPHE and is modeled by STT simulations. Such double pulse-induced dynamics have been reported recently to explain switching mechanisms [7,106,107].

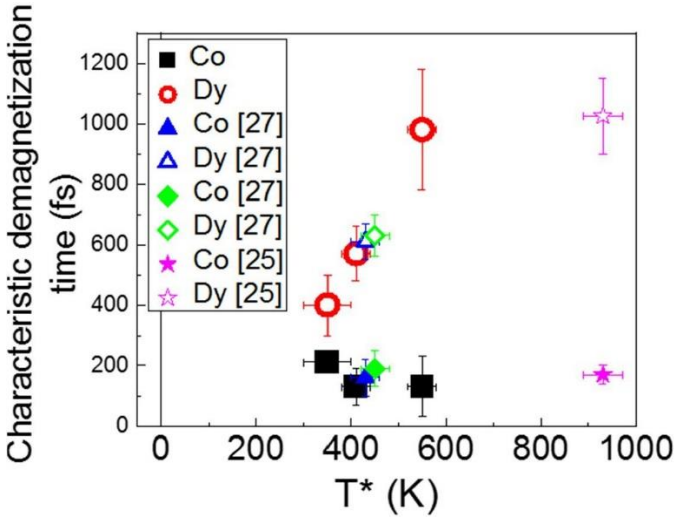

Figure 5.10 *Characteristic demagnetization times for Co 3d (filled symbols) and Dy 4f (open symbols) sublattices as a function of the proximity to* T_{Curie} *(T* =* T_{Curie} *-T). Note that the characteristic times of Dy continuously decrease (faster dynamics) when reaching higher temperatures (from T* =600 to T* =300 K). At the same time, Co3d shows smaller variations with a tendency to slower dynamics in the vicinity of T*=350K. This published result shows that even far from T=*T_C*, the variation of characteristic times is sizable for the 4f in RE. Data are from Ferté et al.* [25]

Considering previously published results from our group [25], we could expect that in RE-TM alloys, the RE and TM sublattices show opposite changes

(acceleration or deceleration of the demagnetization dynamic) when the temperature is increased towards T_C (see Fig. 5.10). The T_C of the $Fe_{74}Gd_{26}$ is 500K, which leads to Tc-T = 350 K. In FeGd, assuming that in P configuration (blue symbols in Fig. 5.7), a supplement of energy flows into the 3d Fe, compared to AP, then we could expect that the excess energy raises the electron temperatures and lead to an acceleration of 3d Fe and a deceleration of 4f Gd dynamic. This is what is observed here for FeGd. However, this is opposite to the case of CoDy (Fig 5.10), which suggests that the temperature-dependent accelerations are RE-TM alloy-dependent [25].

Amplitude of expected SPHE effects:

Finally, considering simple macroscopic arguments of angular momentum conservations in the spin valve, we estimate that a maximum of angular momentum loss in Co/Pt will provide for 2.7 μ_B out from the multilayer (0.6 nm thick Co film times 1.5 μ_B/atom), which can be transferred to the FeGd alloy (at t= t0, a15nm thick FeGd film, times 2 μ_B/at = 22.5 μ_B). We thus expect a maximum change of 12% in the angular moment of the FeGd alloy due to the spin effect in HE-induced demagnetization, assuming a complete quenching of the Co/Pt film and a 100 % transfer efficiency. It seems thus reasonable to measure at FeL_3 edge a limited P/AP effect of 4 %.

Dynamics at the longer time scale

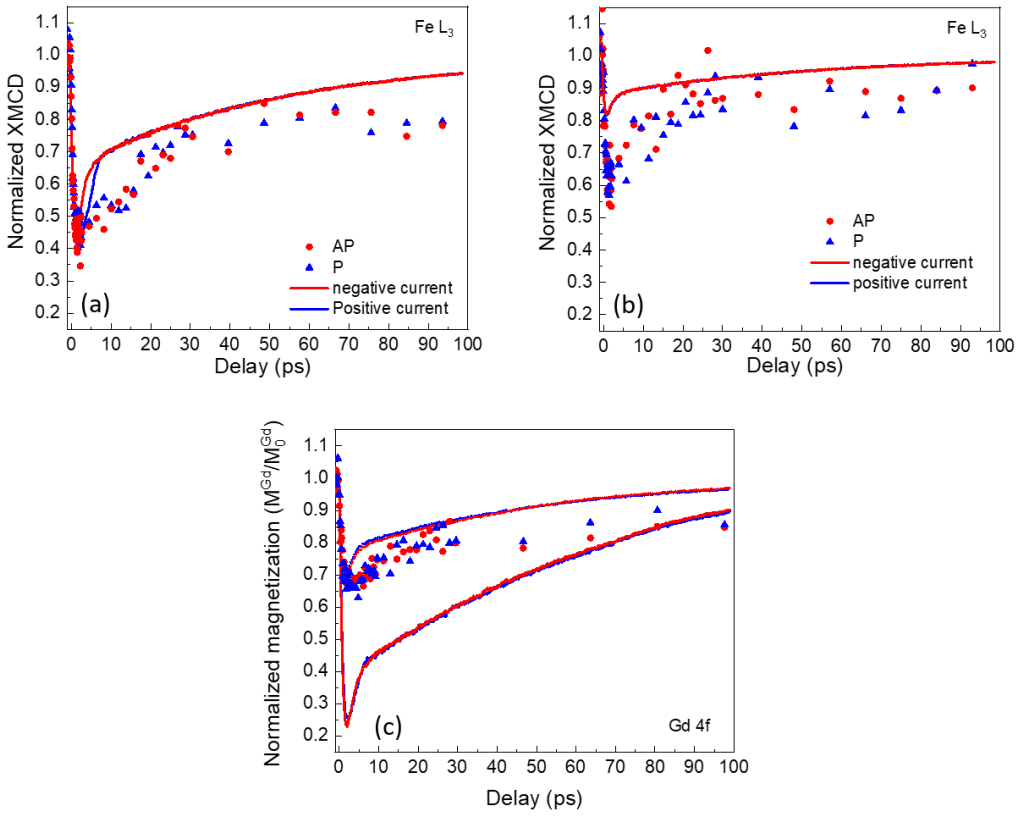

Figure 5.11: Simulated dynamics up to 100 ps for Fe and Gd at two fluences, 3.2 (120) mJ/cm², and 1.2 (40) mJ/cm². Values in brackets correspond to the experimental incidence fluence values. (a,b) Simulated (solid lines) and experiment (solid points) dynamics for Fe at 3.2(120) mJ/cm² and 1.2 (40) mJ/cm², respectively. (c) Corresponds to simulated dynamics for Gd at 3.2 and 1.2 mJ/cm² (solid lines). An experiment at high fluence for Gd was not carried out; therefore, it only compared with experimental results at 40mJ/cm² (solid point). The red curve (solid symbols) corresponds to AP in all the graphs, and the blue corresponds to the P configuration. The red (blue) solid lines represent the negative (positive) SPHE current orientation.

Figure 5.11 shows the simulated dynamics upto 100 ps. It shows both dynamics converge and recover to the same level as in the case of experimental results. Since it's not the main focus of this work to fit the dynamics at a longer time scale, the same parameters were used for both sublattices. This is why recovery until 40 ps doesn't match the experimental data points. It's because the coupling constants used to simulate thermal demagnetization are not optimized for Fe and Gd separately.

5.4 Conclusion

In this chapter, we explored the impact of the SPHE induced effect on spin valve structure consisting of $Fe_{74}Gd_{26}$/Cu/{Co/Pt}*3. We report on combined experimental and theoretical results evidencing the spin-dependent

HE-induced demagnetization in the ultrashort time scale that defines the microscopic mechanisms at work [108]. We give the first experimental results evidencing the timescales of the ultrafast quenching of the magnetization in ferrimagnetic $Fe_{74}Gd_{26}$, induced by ultrashort pulses of spin currents as produced in a collinear magnetic spin valve structure (CoPt/ Cu/ FeGd). In addition, it is reported here that, relying on experimentally defined geometry and composition as well as interatomic exchange, theoretical modeling based on atomistic spin-dynamics simulations reproduce the experimental ultrafast dynamics of $Fe_{74}Gd_{26}$, a fact that allows to identify of the microscopic process of spin angular moment transfer at the shortest time scale. The model reproduces the experimental data and reveals how SPHE excitations drive the demagnetization in both $Fe_{74}Gd_{26}$ sub-lattices. Most noteworthy, the theoretical calculations reproduce the time scales and amplitudes of the experimental results recorded at Fe L_3 and Gd M_5 edges, leading to an indirect determination of the degree of spin polarization in the SPHE current. The theoretical calculations lead to the determination of the spin polarization in the SPHE current, which is opposite to the magnetization of the Co/Pt multilayer. This finding is new and surprising but to the best of our knowledge, we do not have any indication of well-defined spin polarization out of such multilayers.

This model can further be used to predict the impact of fluence-dependent variations of the HE induced heating and of STT in both of the $Fe_{74}Gd_{26}$ sub-lattices.

Further exploration of the SPHE effect using ultrashort X-rays and the dependence on the fluence could contribute to a better understanding of this effect. For such studies, however, we plan to use ultrabright XFEL sources.

---

*All the results in this section are theoretical calculations done by our collaborators, Maryna Pankratova, from the O. Erikson group at Uppsala University.

Chapter 6 Spin-polarized hot-electron induced dynamics in CoGd alloy system

In the previous chapter, I presented experimental evidence of SPHE induced ultrafast 3d spin dynamics in a ferrimagnetic $Fe_{74}Gd_{26}$ alloy, while no SPHE effect was observed on Gd 4f spins. Theoretical calculations based on atomistic spin dynamics, including STT, have provided a satisfactory interpretation of these experimental observations. In this chapter, I will present an almost identical study, except that I have used a ferrimagnetic $Co_{61}Gd_{39}$ alloy as a detection layer. The following chapter is divided into two parts. In the first part, based on TR-XMCD measurements, I will compare the characteristics of the hot-electron and IR laser induced ultrafast Gd 4f spin dynamics and then show evidence of SPHE-induced Gd 4f spin dynamics in the ferrimagnetic $Co_{61}Gd_{39}$ alloy. I will emphasize the very different properties of HE-induced demagnetization and SPHE induced spin dynamics in CoGd compared to those observed in FeGd. In the second part, I will present a detailed characterization of the electronic properties at the surface of CoGd, which is probably the key to understand the SPHE induced Gd 4f spin dynamics in CoGd alloys. Indeed, SPHE effects are surface-sensitive effects due to the limited spin diffusion length in the magnetic layer. We have performed surface-sensitive soft X-ray photoelectron spectroscopy on the TEMPO beamline at synchrotron SOLEIL for $Co_{65}Gd_{35}$ and $Co_{80}Gd_{20}$ alloys.

Initially, there were three basic reasons for this choice. First, in TM-Gd alloys, the HE interacts with the electrons in the conduction band which is mainly occupied with TM 3d electrons. Since Co and Fe have different densities of state, CoGd and FeGd alloys are expected to have different dynamical responses to SPHE excitation. Second, the characteristics of IR laser induced ultrafast Gd 4f spin dynamics are very different in FeGd [23,109] and CoGd [92] alloys. Therefore, we also expect such differences in SPHE induced spin dynamics. Third, CoGd is an archetypical ferrimagnet in which we have intensively studied the IR laser induced ultrafast Gd 4f spin dynamics [22,84,92,110].

6.1 Time-resolved XMCD study on Gd 4f moment

6.1.1 Experimental details

For this study, we have selected the following sample structure: SiN/Ta (5) /Cu (20)/Ta (5) / $Co_{61}Gd_{39}$ (15) /Cu (4) /$Co_{75}Pt_{25}$(3) /Cu (60) /Pt (6). Figure 6.1 (a) shows the schematic of the spin valve structure. The role of each layer, the choice of the specific compositions, and the thicknesses are detailed in section 4.1. In brief, the $Co_{75}Pt_{25}$ alloy acts as a spin polarizer, and the $Co_{61}Gd_{39}$ alloy is the detection layer on which the SPHE-induced spin dynamics have been studied. Both layers display in-plane magnetic anisotropy. Figure 6.1 (b) shows the hysteresis loops of the $Co_{61}Gd_{39}$ (15)/Cu (4)/CoPt (3) spin valve structure measured by mean of XMCD at the Gd M_5 and the Co L_3 resonance edges at 300 K. A detailed discussion of the shape of these hysteresis loops are provided in section 4.3.2.

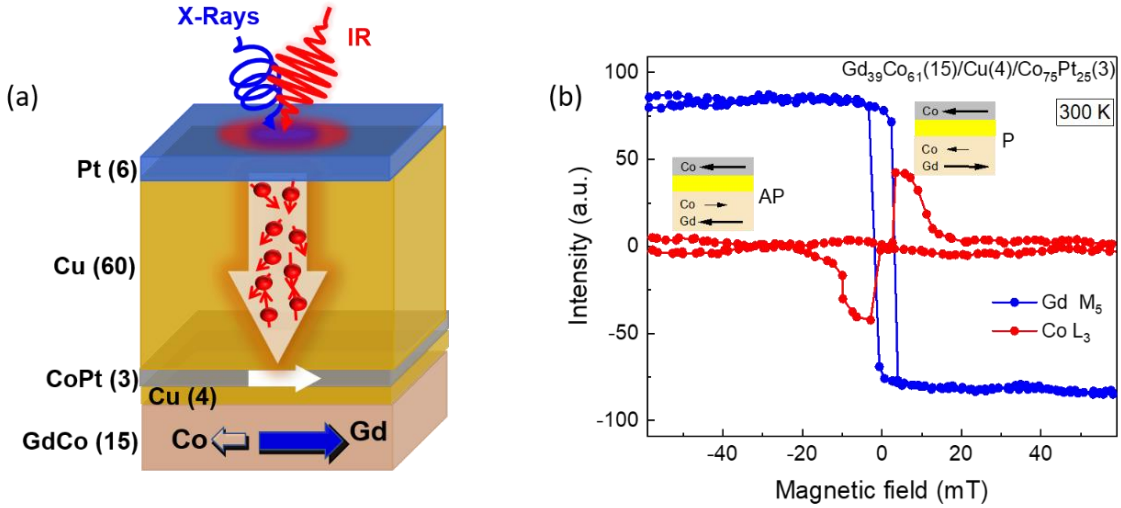

Figure 6.1: Schematic of spin valve used for SPHE study – $Co_{61}Gd_{39}$ (15)/Cu (4)/CoPt (3)/Cu(60)/Pt(6), with in-plane anisotropy. Pt(6)/Cu(60) is used to generate and transport the ultrashort pulse of HE. CoPt (hard magnetic layer) acts as a spin polarizer, and $Co_{61}Gd_{39}$ is the detector layer. Arrows within the magnetic layers show the magnetic orientation of each element. (b) Hysteresis recorded at 300 K for $Co_{61}Gd_{39}$ (15)/Cu (4)/CoPt (3) at Gd M_5 (blue line) and Co L_3 (red line), respectively.

The hysteresis loop at the Co L_3 edge probes the magnetic properties of both layers, while the hysteresis loop at the Gd M_5 edge probes only the magnetic properties in the $Co_{61}Gd_{39}$ alloy. They show that both layers have distinct coercive fields and are not exchange-coupled. The spin-polarizer CoPt layer has a larger coercive field (Hc ~ 10 mT) than the $Co_{61}Gd_{39}$ alloy (Hc ~ 3

mT). Therefore, it is possible to reverse the magnetization of the $Co_{61}Gd_{39}$ layer with a moderate external magnetic field without reversing the CoPt layer.

It allows measuring the time-resolved XMCD as a function of pump-probe delay at the Gd M_5 resonance edge in two configurations: (1) Parallel and (2) antiparallel orientation of the Co magnetization in CoPt and $Co_{61}Gd_{39}$ layers (Fig. 6.1 (b)). This experimental protocol allows to distinguish the effect of spin-polarized effects from the thermal hot-electron induced demagnetization, as discussed in the previous chapter.

Prior to Tr-XMCD experiments in the femtoslicing mode, we optimized all the experimental parameters, such as the laser fluence, the temperature and the magnetic field, by using the picosecond mode, following the same protocol as described in section 5.1.2 for the FeGd alloy. The pump-probe experiments were performed at 60 mJ/cm² IR incidence fluence and T_{cryo} = 80 K for the two configurations. Similar to static XMCD measurements used for the characterization of the layer, the sample was tilted by 35° with respect to the X-ray propagation axis, which was needed to obtain a sizable projection of the in-plane magnetization on the X-ray propagation axis.

We measured the transient XMCD in P and AP configurations. However, before going into the discussion of the SPHE effect and in order to discuss the amplitudes and demagnetization times of the transient XMCD recorded at the Gd M_5 edge qualitatively, the HE induced demagnetization dynamics are shown in Figure 6.2. This curve shows the averaged P and AP delay scans where the HE-induced demagnetization is isolated from the spin effect. (Note that the individual P and AP delay scans are shown in Fig. 6.5.)

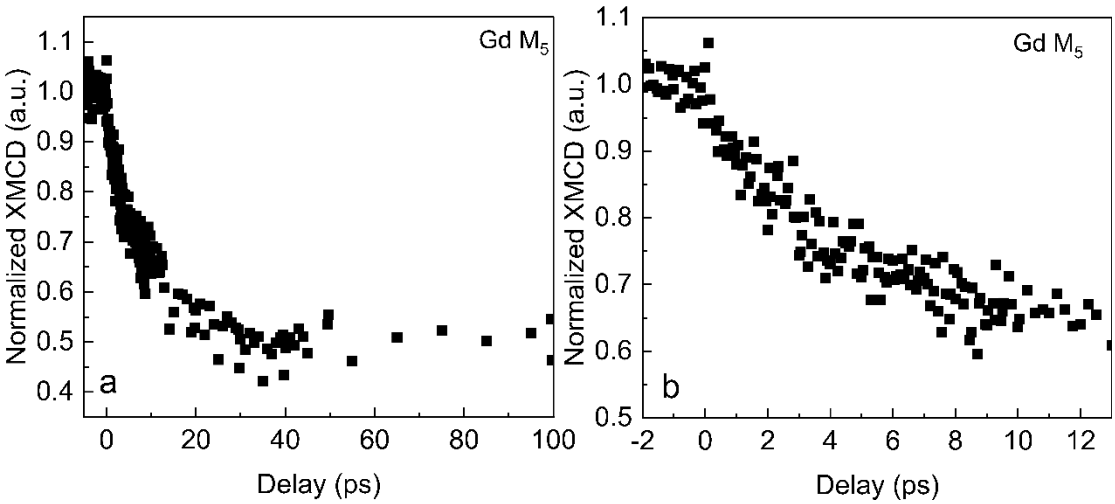

Figure 6.2 Hot electron induced dynamics obtained by averaging the transient XMCD measured at P and AP configuration at Gd M_5 edge (a) at a longer time scale upto 100 ps and (b) upto 13 ps time.

In Figure 6.2 a and 6.2 b, we observe that the demagnetization of the Gd 4f sublattice occurs within tens of picoseconds, which is very slow compared to

the hot electron-induced demagnetization of the Gd 4f sublattice in the FeGd alloys reported in the previous chapter. To explain this slow dynamic, let us discuss the hot-electron-induced data and compare them with the literature for similar alloys.

6.1.2 Hot-electron induced dynamics in $Co_{61}Gd_{39}$

The sample structure ensures that the $Co_{61}Gd_{39}$ layer is not directly excited by IR pump pulses. Therefore, the demagnetization of the Gd 4f sublattice observed in Figure 6.2 is induced by the photoexcited hot electron pulses [39]. In line with previous works on laser-induced demagnetization of Gd sublattices in Co_xGd_{100-x} alloys [92], we observe that the demagnetization occurs on two subsequent times scales with a maximum demagnetization amplitude reached at t_{min} ~ 38 ps. In the previous chapter, I have shown that it takes only t_{min} ~ 3.4 ps for the $Fe_{74}Gd_{26}$ alloy (see section 5.2.1). Since the sample structures are almost similar for both samples, this difference in t_{min} cannot be attributed to the characteristic of the HE pulses [41,45]. In a recent work, Ferté et al. showed that the characteristic laser-induced demagnetization times strongly depend on the CoGd alloy composition since there is no direct Gd 4f spin-lattice [92] as previously proposed by Wietstruk et al. for pure Gd layer [21]. Therefore, the angular momentum transfer from the Gd 4f spins to the lattice is mediated by the intra-atomic Gd 4f – Gd 5d exchange coupling, the inter-atomic Gd 5d- Co 3d exchange coupling, and finally, the Co 3d spin-lattice coupling. Although this study was based on direct IR excitation, we infer that such a mechanism is also responsible for the "slow" HE induced Gd 4f dynamics, as we report for the $Co_{61}Gd_{39}$ alloy (Fig. 6.2 a).

In order to challenge this assumption, we have extended our study to measure the hot-electron induced demagnetization of Gd 4f sublattice in a different alloy, i.e., $Co_{68.3}Gd_{31.7}$, which has a concentration close to recent work by Ferte et al. [92]. This second alloy grew with the same capping layer as used in the previous section but without any CoPt layer between capping and CoGd alloy to avoid the spin polarization effect in the HE-induced demagnetization.

6.1.3 A comparison between direct (IR) and indirect (HE) excitation of $Co_{68}Gd_{31}$

We have recorded the transient XMCD at the Gd M_5 edge of a $Co_{68.3}Gd_{31.7}$ (15)/ Cu (60)/ Pt (6) sample for a laser fluence of 80 mJ/cm^2 and T_{cyro} = 80 K as shown in Figure 6.3. In this Figure, I also plotted the IR laser induced

demagnetization of the Gd 4f sublattice in a similar $Co_{72}Gd_{28}$ alloy [92] for comparison.

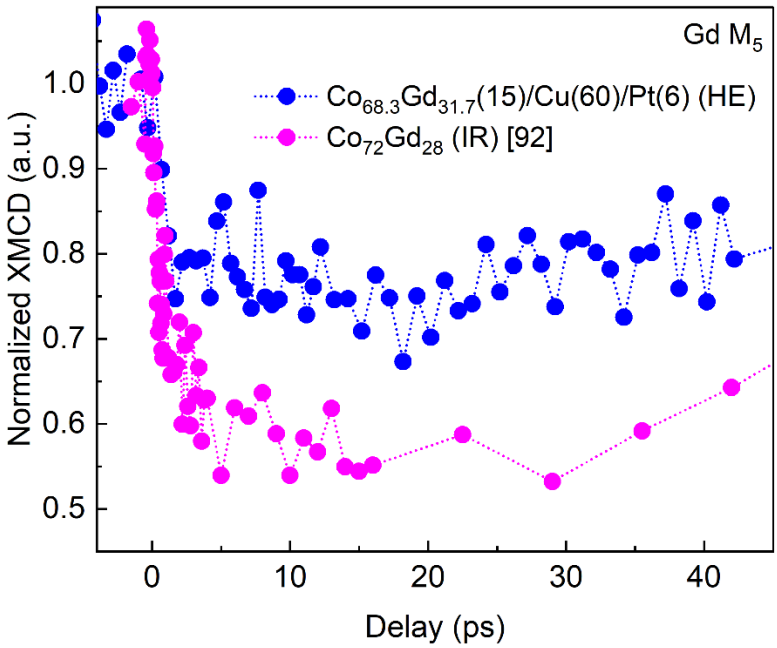

Figure 6.3 Hot electron induced dynamics at Gd M_5 edge for $Co_{68.3}Gd_{31.7}$ (15)/ Cu (60)/ Pt (6) (blue curve) at 80 mJ/cm² incidence laser fluence and T_{cryo} = 80 K. Compared with the direct IR excitation on similar composition (magenta curve).

Interestingly, we observe that the demagnetization of the Gd 4f sublattice in the $Co_{69}Gd_{31}$ alloy occurs on two subsequent time scales, just like the $Co_{61}Gd_{39}$. But in this case, the maximum demagnetization is reached at t_{min} ~20 ps instead of t_{min} ~38 ps.

Figure 6.4 shows a compilation of different results from literature and our results for both CoGd alloys, where the demagnetization time is shown as a function of the Gd concentration for direct IR excitation [21,84,92] and for HE induced dynamics (Green circles - our work). We observed a linear dependency of this time on Gd concentration for the different CoGd alloys, which supports the scenario of angular momentum flow from the Gd 4f spin to the lattice mediated by the RKKY coupling [21,92,111].

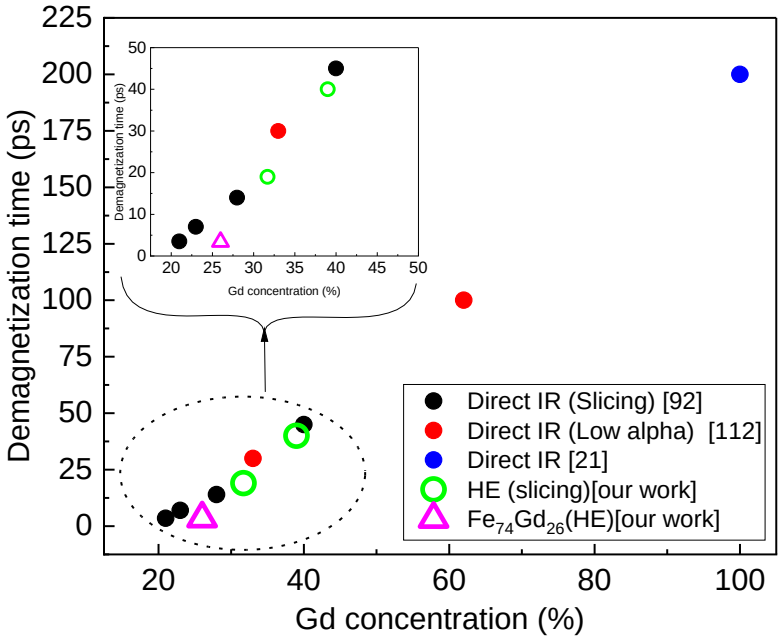

Figure 6.4 Demagnetization time (minima of demagnetization dynamics) as a function of Gd concentration from different studies and compared with our experiment results. Solid data points correspond to direct excitation, taken from the (black points) [92], (red points) [84], and pure Gd (blue) [21]. Open green circle data points represent our hot electron (HE) induced dynamics shown in this chapter. The open magenta triangle belongs to HE induced $Fe_{74}Gd_{26}$ dynamics from section 5.2.1.

Moreover, we have also reported the time delay at which the demagnetization is maximal for the $Fe_{74}Gd_{26}$ alloy in Figure 6.4. It is worth noticing that Radu et al. have reported the same value for the laser-induced demagnetization of the Gd 4f sublattice in a $Fe_{66}Co_9Gd_{25}$ alloy. The inset of Figure 6.4 emphasizes the striking difference between the $Fe_{74}Gd_{26}$ alloy and the CoGd alloys for comparable compositions. Unfortunately, although laser induced ultrafast spin dynamics in FeGd alloys have been widely investigated within the last decades [23,27,103,112,113], it was almost always in a very narrow composition range. A systematic study to investigate the dependence of the characteristic demagnetization time on composition in Fe_xGd_{100-x} is still lacking to compare with the case of CoGd alloys.

6.1.4 Observation of spin-polarized hot electron induced effects

This section is dedicated to the SPHE induced effect on $Co_{61}Gd_{39}$, the transient-XMCD results for both P and AP configurations at the Gd M_5 edge. Figure 6.5 shows the long (a) and the short (b) time scales for P and AP configurations. In Figure 6.5 b, we evidence the difference in the

demagnetization amplitudes and dynamics between ~8 and ~12 ps that are possibly related to the SPHE effects. At these delays the demagnetization is larger in the AP configuration. Since demagnetization is superposed from 0 ps to ~7 ps and at delays > 15 ps, we rule out any measurement artifacts. This difference is highlighted by drawing horizontal lines in Figure 6.5 (b) that give the demagnetization amplitude at a delay of 12 ps.

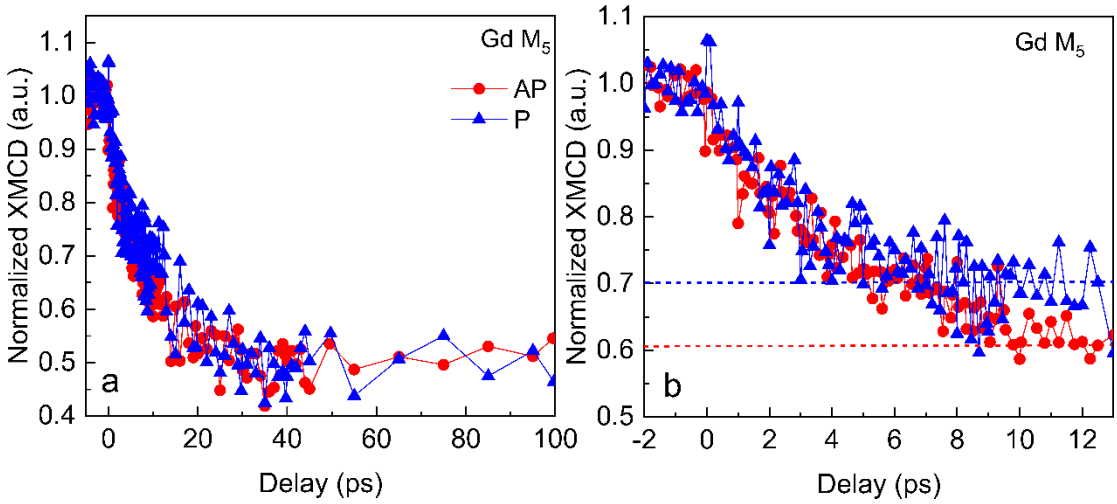

Figure 6.5 Pump-probe delay scans at GdM_5 for sample $Co_{61}Gd_{39}$ (15)/Cu (4)/CoPt (3), performed with 60mJ/cm² laser fluence at T=80 K (a) long delay range up to 100 ps and (b) short delay range (up to 13 ps). Blue and red curves with solid points represent the Co-Co parallel (blue) and antiparallel (red) orientations, respectively. The horizontal blue dotted line in (b) represents the -30% demagnetization amplitude for P reached at a delay of ~ 10 ps, whereas the red dotted line highlights the demagnetization amplitude of -40% in the AP case.

The difference in the P/AP dynamics can be a signature of the spin-polarized hot-electron pulses on the dynamics of Gd 4f spins, which was not observed in the case of $Fe_{74}Gd_{26}$ alloy (section 5.2.2). As discussed in the previous chapter, the theoretical calculations based on heat-driven dynamics with STT predict a signature of SPHE induced effect on the Gd 4f spin dynamics, but the size of the effect depends on the amplitude of thermal demagnetization (Fig 5.9). Therefore, the larger demagnetization of the Gd 4f sublattice in $Co_{61}Gd_{39}$ alloy (50 %) than that reported in the $Fe_{74}Gd_{26}$ alloy (30%) may explain the larger SPHE effects on Gd 4f spin dynamics. Furthermore, we cannot exclude that the efficiency of SPHE induced Gd 4f spin dynamics depends strongly on the band structure of the alloys, and thus, it may be more pronounced for Co-based than Fe-based alloys. Additionally, it's worth mentioning that demagnetization of the Gd 4f sublattice in $Co_{61}Gd_{39}$ is larger for AP configuration than P configuration, similar to the theoretical calculations for Gd4f in the FeGd sample.

Therefore, further experiments in CoGd and FeGd alloys above T_{comp}, where the magnetization is dominated by that of the 3d sublattice, are needed to challenge the accuracy of the model's predictions. However, the SPHE effect on Gd 4f spins in $Co_{69}Gd_{31}$ occurs on a much longer time scale (around 10 ps) than that observed for the Fe sublattice in the $Fe_{74}Gd_{26}$ alloys (Chapter 5) as well as that observed by Stamm et al. in Fe/Ni bilayers [6]. Unfortunately, this time scale cannot be reproduced by the theoretical model described in the previous chapter, which means that further theoretical developments are needed to get a complete picture.

Nevertheless, the hot-electron induced demagnetization is a "bulk" excitation, as shown by the large demagnetization amplitudes, the effects associated with the spin-polarization are surface sensitive due to the limited spin diffusion length in magnetic layers (~ 7 nm for Fe, 4.6 nm for Co [90]). It follows that the SPHE-induced spin dynamics are maximum within the first few nanometers of our CoGd (15) alloys. Since it's well known that amorphous CoGd ferrimagnetic alloys display in-depth compositional gradients [98], it is crucial to characterize the surface of our CoGd alloys.

6.2 Surface study Co_xGd_{100-x} alloys by XPS

In this part of the chapter, I will present an investigation of the surface composition of two alloys: $Co_{65}Gd_{35}$ and $Co_{80}Gd_{20}$. The measurements were performed using surface-sensitive soft X-ray photoelectron spectroscopy (XPS) on the TEMPO beamline at synchrotron SOLEIL. The experimental setup is shown in section 3.1.1.3. For this study, the sample's normal was aligned with the entrance of the photoelectron analyzer, while the X-ray beam impinged the samples at an angle of $\alpha_X = 44°$ with respect to the sample's normal.

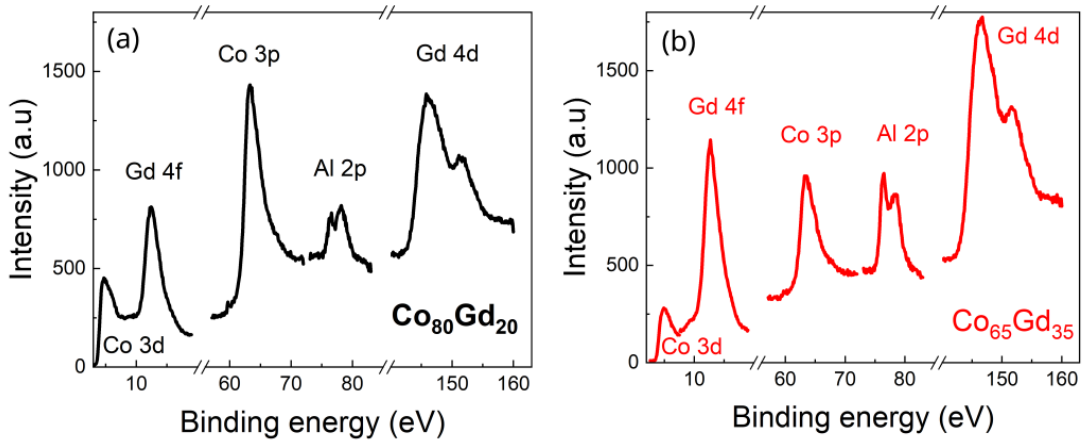

Figure 6.6: X-ray photoelectron spectra taken at 700 eV photon energy showing the Co 3p, 3d, Gd 4f,4d, and the Al 2p core-levels for the alloys (a) $Co_{80}Gd_{20}$ and (b) $Co_{65}Gd_{35}$.

The Co_xGd_{100-x}(20) alloy layers were grown by DC co-sputtering on [Ta(5)/Cu(20)/Ta(5)]x5 multilayers deposited on Si substrates (units in nm). The layers were capped with an Al (5) layer to prevent degradation of the alloy in the ambient atmosphere [98]. This Al (5) layer is partly oxidized during exposure to air, but its thickness ensures that a metallic Al layer remains in contact with the Co_xGd_{100-x} (20) alloys. Therefore, the actual structure of the samples is Al_2O_3(~3)/Al (~2)/Co_xGd_{100-x} (20)/ [Ta(5)/Cu (20)/Ta (5)]5/Si. Due to the limited mean free path of the photoelectrons (~1 nm), the Al_2O_3(~3)/Al (~2) capping layer was almost completely removed in-situ by Ar+ sputtering before the XPS measurements. We regularly monitored the change in thickness as a function of sputtering time to minimize the etching of the alloys.

We recorded the XPS spectra of the Al 2p, Gd 4d, 4f, and Co 3p, 3d core levels for $Co_{80}Gd_{20}$ and Co_6Gd_{35} at a photon energy of 700 eV, as shown in Figure 6.6.

These measurements were repeated at photon energies of 400 eV and 1000 eV. This protocol allows for varying the surface sensitivity of core-level XPS since the electron inelastic mean free path depends on the kinetic energy of photoelectrons and, thus, on the photon energy (Table 6.1) [114]. As a consequence, the larger photon energies allow probing deeper into the layer.

The mean free path of the Co 3p and Gd 4f core-level photoelectrons in bulk Co and Gd, as a function of photon energy are summarized in Table 6.1.

Photon energy (eV)	**Mean free path λ (nm)**	
	λCo	**λGd**
400	**0.62**	**0.98**
700	**0.82**	**1.47**
1000	**0.97**	**1.94**

Table 6.1: Mean free paths of the Co 3p and Gd 4f core-level photoelectrons in bulk Co and Gd as a function of the incident photon energy as given by [114]. We have considered that Co 3p and Gd 4f have almost identical kinetic energies and thus identical IMFP.

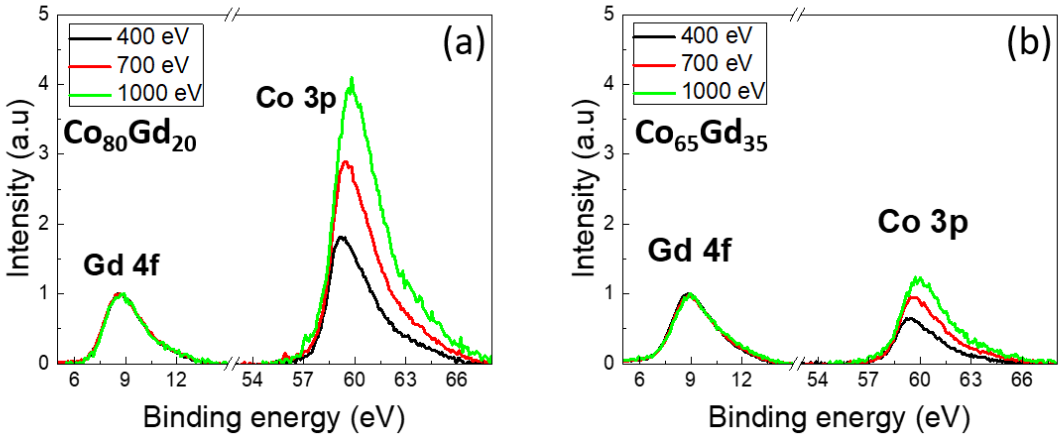

Figure 6.7: X-ray Photoelectron spectra of the Co 3p and Gd 4f core-levels for (a) $Co_{80}Gd_{20}$ and (b) $Co_{65}Gd_{35}$ at the photon energies of 400 eV (black spectra), 700 eV (red spectra) and 1000 eV (green spectra). The spectra have been subtracted by a Shirley function and normalized by the photoionization cross section [115]. All spectra have been normalized to 1 at the Gd4f.

Figure 6.7 shows the Gd 4f and Co 3p core-levels as a function of the photon energy for the $Co_{80}Gd_{20}$ (a) and $Co_{65}Gd_{35}$ (b) alloys, respectively. To perform a quantitative analysis of the average atomic concentration of each element, before calculating the area under the peak, a Shirley-like background was subtracted from the experimental XPS core-level peaks, and the peak's area was normalized by the energy-dependent photoionization cross-section of the materials [115]. Additionally, the spectra were normalized with the height of the Gd 4f peak for direct comparison. Figure 6.7 (a, b) shows that the height of the Co 3p peak increases with respect to that of the Gd 4f on an increase of photon energy from 400 eV to 1000 eV.

In order to quantify the Gd excess at the surface of the alloy with respect to the nominal composition, we define R as the ratio between the Gd 4f and Co 3p core-level peak's area.

$$R = \frac{A_{Gd_{4f}}}{A_{Co_{3p}}}$$

Where, $A_{Gd_{4f}}$ *and* $A_{Co_{3p}}$ are the areas under Gd 4f and Co 3p core level peaks. The dependence of R on the photon energy for both alloys is depicted in Figure 6.8 (a). R decreases on changing the energy and illustrates that the atomic concentration of Co increases on moving from the surface (400 eV) to the alloy's

bulk (1000 eV). It shows that the concentration in the alloy is inhomogeneous and that the surface is rich in Gd compared to the nominal bulk concentration.

Experimental evidence of surface inhomogeneous composition was further validated by a model (developed by M. Pace [PhD thesis - 2023]).

In this model, the concentration of alloy was calculated as a function of thickness (t). The XPS signal of an element *x* coming from the ith layer, A_x^i is written as:

$$A_x^i = \exp\left(\sum_{j=0}^{i}\left\{-\frac{1}{cos\theta}\frac{1}{(C_{Co(x)}(j)\lambda_{Co} + C_{Gd(100-x)}\lambda_{Gd})}\right\}\right)$$

Where, $C_{Co(x)}(j)$ and $C_{Gd(100-x)}(j)$ are the concentration of Co and Gd in Co_xGd_{100-x} alloy in the layer j and λ is the photoelectron mean free path (IMFP) in the bulk Co and Gd. Then, the total XPS signal of element x is given by:

$$A_x = \sum_{i=0}^{150} A_x^i$$

Here, 150 represents the thickness of the alloy. R is calculated by extracting the ratio A_{Gd}/A_{Co}. Here, sample thickness was divided in a series of 150 individual layers of 1 Å thickness. Additionally, to calculate concentration profile, effective λ was used by considering the linear combination of Co and Gd in each layer *i* and IMFP of photoelectrons crossing through each layer *i*. By varying the concentration step by step the value R was calculated for each atomic layer and summed to a final value until matching the experimental values at all photon energies.

This elementary model provided a qualitative description of the variation of concentration within the alloys. Figure 6.8 (b) shows the simulated profile for two alloys. The profile was determined by optimizing the calculated and experimental dependence of R on photon energy, shown in Figure 6.8 (a). Considering the limited inelastic mean free path of photoelectrons in CoGd alloys (Table 6.1), we have set the composition to the nominal value as given by VSM measurements for thicknesses above 5 nm.

In the case of $Co_{80}Gd_{20}$ alloy, the simulated profile shows a segregated Gd layer on top of an almost homogeneous sample with almost the nominal composition as previously reported for a comparable alloy composition [98].

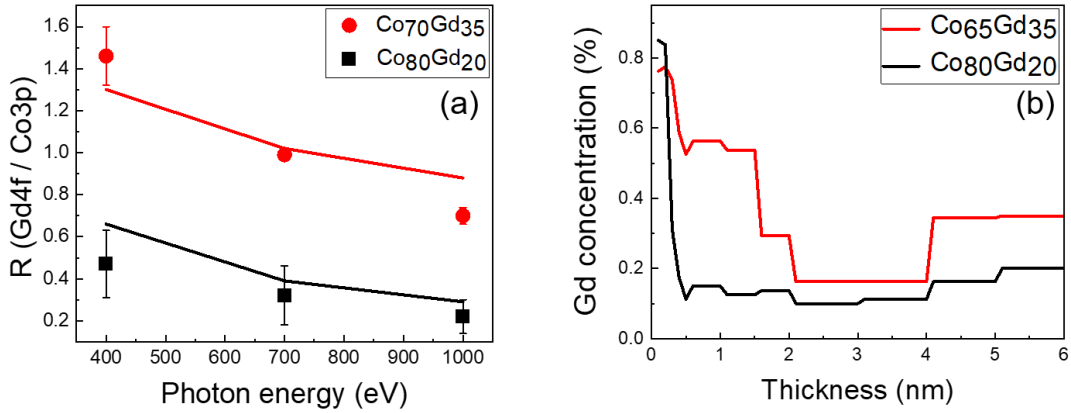

Figure 6.8 (*a) Comparison between the experimental (symbols) and the calculated (solid lines) energy dependence of the ratio R= Gd 4f / Co 3p. (b) Simulated Gd composition profile at the surface of the $Co_{80}Gd_{20}$ (black line) and the $Co_{65}Gd_{35}$ (red line) alloys.*

However, the simulated profile of the $Co_{65}Gd_{35}$ alloy shows a pronounced Gd compositional gradient at the surface of the alloy and, thus, a sizable increase of the Gd contents over almost 2 nm with respect to the nominal composition.

Therefore, our observations based on XPS demonstrate that the alloys are inhomogeneous and that these profiles depend on the alloy composition.: The segregation of Gd on the surface is more pronounced in Gd-rich alloys.

We concluded paragraph 6.1 by pointing to the limited spin-diffusion length of the hot-electron and we have inferred that the SPHE induced effects could be more pronounced at the surface of the CoGd alloys. Our surface-sensitive measurements have demonstrated that the surface of our Co61Gd39 alloys is Gd-rich. Since we have also shown that the characteristic demagnetization times depend on the alloy's composition (Fig. 6.4), we suppose that the observation of SPHE induced effect on the ~10 ps time range could be caused by the "slow" dynamics at the surface.

6.3 Conclusions

In the first part of this chapter, we reported on the hot electron induced dynamics of Gd 4f moments in two different alloys: $Co_{61}Gd_{39}$ and $Co_{68.3}Gd_{31}$. Both alloys showed two-step demagnetization, which agrees with IR induced demagnetization in CoGd alloys, as reported in recent work [92]. By comparing with the available literature, we showed that the characteristic demagnetization times depend linearly on Gd composition irrespective of the mean of excitation, either IR or HE pulses. In the case of $Co_{61}Gd_{39}$/Cu (4)/CoPt (3), we observed at

a few picoseconds delay a possible signature of SPHE induced dynamics on Gd 4f spin, faster in the case of AP than P configuration.

In the second part of this chapter, we have shown that the surface of the CoGd alloys is Gd rich compared to the bulk, and these inhomogeneities are composition-dependent. Indeed, the Gd migration at the surface is more pronounced in alloys that display a larger Gd content in the bulk, as predicted by surface-free energy considerations [116]. We believe that the result of this study is important for understanding the "long" time scale on which the SPHE-induced Gd 4f spin dynamics occur. It is a consequence of the limited spin-diffusion length of HE (i.e., a surface-sensitive effect) and the "slow" dynamics expected for a Gd-rich alloy (Fig. 6.4).

Therefore, this work calls for in-depth resolved experiments with nanometer spatial resolution (eventually combined with sub-picosecond time resolutions). Such experiments can be conducted either at large scale facilities [117] or by using table-top X-ray sources [118].

Chapter 7 General Discussion

In this work, we studied the SPHE induced dynamics at Fe3d and Gd 4f moments in two systems: $Fe_{74}Gd_{26}$ (15) / Cu (10)/ {Co (0.6)/Pt (1)*3} and $Co_{61}Gd_{39}$ /Cu (4) / CoPt (3) based spin-valve structures.

1. In the case of FeGd alloys, results at Fe L_3 show that the dynamics in the parallel case (P) are faster than for the AP case. However, these results are surprising when compared with the previous work done on ferromagnetic 3d TM-based spin valve structures, i.e., CoPt/Ru/CoPt [3] and Fe/Ru/Ni [6]. In both previous studies, they observed faster dynamics when both magnetizations of the 3d layers were antiparallel to each other. Theoretical calculations are definitively mandatory for the interpretations of our results. The theoretical calculations based on heat-driven dynamics with STT confirmed the effect at FeL_3 in the $Fe_{74}Gd_{26}$ alloy and showed the dependence of the size of the effect with the laser fluence. According to the simulated dynamics, the spin polarization of SPHE current is opposite to the CoPt magnetization, i.e., minority spin can be mainly responsible for accelerating the demagnetization dynamics of Fe 3d moments. Until now, only one parallel magnetization geometry has shown the opposite trend in 3d TM-based spin valve structures favoring spin switching by Igarashi et al. [7]. Based on our work and calculations, we can emphasize that the outcoming SPHE current from CoPt has opposite polarization than Co magnetization and explain the apparent surprising results for parallel magnetization geometries. However, to ascertain this point, it's important to calculate the spin polarization of hot electrons considering band structure.
2. This model further predicts that at the GdM_5, we should expect a smaller and opposite effect, i.e., the AP configuration leads to faster demagnetization in the Gd4f sublattice. The result is in line with STT, where spin polarization of SPHE current is opposite to the Gd 4f magnetization, which accelerates its demagnetization.

3. In the case of $Co_{61}Gd_{39}$/Cu (4)/CoPt (3) at Gd M_5, we observed that ultrafast spin current accelerates the dynamics in the case of AP configuration than P configuration. This difference in the dynamics can be the signature of the spin-polarized hot-electron pulses. This SPHE effect occurs on a longer time scale than for FeGd alloys as well as observed by Stamm et al. [6]. We

explained this observation by the segregation of Gd at the surface of the alloy. However, in all RE-TM alloy systems, the spin current interaction is complex due to the detailed spin-resolved band structure.

4. Compared demagnetization dynamics:
   By considering the dynamics of Gd 4f spins in the $Co_{61}Gd_{39}$ and $Fe_{74}Gd_{26}$ alloys, the larger demagnetization amplitude at the Gd M_5 (50%) in $Co_{61}Gd_{39}$ explains the larger SPHE effects compared to $Fe_{74}Gd_{26}$, where Gd 4f was demagnetized only be 30%. This observation supports the predictions of the model. However, the exact efficiency depends strongly on the band structure and does not allow comparing SPHE effects for different alloys. The major difference between both alloys is the time scale of demagnetization measured at Gd M_5. The fact that very slow demagnetization dynamics are measured in CoGd alloys is the origin of the difficulties to resolve ultrafast SPHE effects at subpicosecond time scales. This long demagnetization times are also making more complex the simulations and interpretations of the SPHE induced dynamics.

Finally, to understand our results for each system, we need to compare our results with the theoretical modeling. We will also need more systematic measurements on different alloys and single-element spin valves to test further the modeling proposed in this work. The theoretical calculations evidenced to observe the small signatures of spin currents in the ultrafast demagnetization, we need high signal-to-noise data and strong demagnetization amplitude obtained with large laser fluences.

Conclusion and outlook

Conclusion

In this thesis, I have explored the impact of SPHE induced effect on two different spin valve structures consisting of out-of-plane $Fe_{74}Gd_{26}$/Cu/{Co/Pt}*3 and of an in-plane $Co_{61}Gd_{39}$ /Cu/CoPt. Using Tr-XMCD measurements combined with a theoretical approach, we measured the element specific dynamics and observed the SPHE effect on TM 3d and RE 4f sublattices. The key findings are summarized as follows:

1- In the case of out-of-plane FeGd-based spin-valves, we investigated the spin-polarized hot electron-induced dynamics of Fe 3d and Gd 4f moments in a $Fe_{74}Gd_{26}$ alloy. Results at Fe L_3 and Gd M_5 indicated that hot electron demagnetization dynamics are comparable to direct excitation. Additionally, an increase in the fluence revealed that faster dynamics in Fe could be observed for HE-induced demagnetization.

- From fitting, crucial parameters such as demagnetization time, hot electron pulse width, and recovery were obtained. The estimation of hot electron pulses highlighted their elongation as they pass through different capping layers.
- Fluence dependence study demonstrated a strong correlation between spin current and laser fluence. The results at the Fe L_3 edge, at incident IR fluence of 120 mJ/cm^2, indicate that the presence of spin current effect modified the demagnetization speed of Fe3d by 4% in $Fe_{74}Gd_{26}$. However, this effect was negligible at a low fluence value.
- The results at the Gd M_5 edge show no spin dependent effect, probably due to the low fluence used during the pump-probe experiments, combined with a limited signal to noise ratio.
- Theoretical calculations based on atomistic spin dynamics with STT successfully reproduced the spin dependent demagnetization dynamics at Fe and Gd edges. The calculations confirmed that Gd4f effects are smaller than the one measured for 3dFe. The calculations were conducted by considering the 100 % spin polarization out of the thin polarizer film Co/Pt. The theoretical calculations lead to the determination of the spin polarization in the SPHE current, which is opposite to the magnetization of the Co/Pt multilayer. This founding is new and surprising but to the best of our knowledge we do not have any indication of well-defined spin polarization out of such multilayers.

This combined experimental and theoretical approach provided detailed insight into the SPHE effect on RE-TM-based alloy systems, particularly in $Fe_{74}Gd_{26}$. These results on $Fe_{74}Gd_{26}$ raise questions about how dynamics are opposite in the case of P and AP configuration. Further exploration of the SPHE effect's dependence on the compensation temperature could contribute to a better understanding this effect.

2- In the case of the CoGd based spin-valves, we investigated the spin-polarized hot electron and hot-electron induced dynamics of Gd 4f moments in two different alloys: $Co_{61}Gd_{39}$ and $Co_{68.3}Gd_{31.7}$. The key findings of this work can be summarized as follows:

- Both the alloys showed slow demagnetization dynamics. Additionally, we observed that demagnetization increased with the increase of Gd concentration, as Ferte et al. [92] reported in direct IR excitation. This increase in the demagnetization time exhibits linear dependence on Gd concentration. It explains the very slow demagnetization in our CoGd alloys.
- In the case of $Co_{61}Gd_{39}$/Cu (4)/CoPt (3), we observed that ultrafast spin current accelerated the Gd4f dynamics in the case of AP configuration relatively longer time scale (between 8-12 ps), which shows that parallel spins between Gd4f and SPHE spins help the demagnetization of 4f magnetization. However, we observed that SPHE induced effect occurs on longer time scale.
- As measured by photoemission, this could be due to important Gd segregation at the surface for large content of Gd in these CoGd alloys.

Outlook

Further exploration of the SPHE effect using ultrashort X-rays and its dependence on the fluence could contribute to a better understanding this effect. For such studies, using ultrabright XFEL sources would allow us to increase the X-ray fluence so that we could record the ultrafast dynamics in the ultrathin CoPt polarizer films as well as in ultrathin ferrimagnetic films.

Further systematic experiments for other systems as a function of the incident fluence, will be allow to corroborate theoretical modeling predictions, to explain the microscopic mechanisms at during the first hundreds of femtoseconds.

References:

[1] A. V. Kimel and M. Li, *Writing Magnetic Memory with Ultrashort Light Pulses*, Nat. Rev. Mater. **4**, 189 (2019).

[2] M. Battiato, K. Carva, and P. M. Oppeneer, *Theory of Laser-Induced Ultrafast Superdiffusive Spin Transport in Layered Heterostructures*, Phys. Rev. B **86**, 024404 (2012).

[3] G. Malinowski, F. Dalla Longa, J. H. H. Rietjens, P. V. Paluskar, R. Huijink, H. J. M. Swagten, and B. Koopmans, *Control of Speed and Efficiency of Ultrafast Demagnetization by Direct Transfer of Spin Angular Momentum*, Nat. Phys. **4**, 855 (2008).

[4] A. Melnikov, I. Razdolski, T. O. Wehling, E. Th. Papaioannou, V. Roddatis, P. Fumagalli, O. Aktsipetrov, A. I. Lichtenstein, and U. Bovensiepen, *Ultrafast Transport of Laser-Excited Spin-Polarized Carriers in $\mathrm{Au}/\mathrm{Fe}/\mathrm{MgO}(001)$*, Phys. Rev. Lett. **107**, 076601 (2011).

[5] A. J. Schellekens, K. C. Kuiper, R. R. J. C. de Wit, and B. Koopmans, *Ultrafast Spin-Transfer Torque Driven by Femtosecond Pulsed-Laser Excitation*, Nat. Commun. **5**, 4333 (2014).

[6] C. Stamm et al., *X-Ray Detection of Ultrashort Spin Current Pulses in Synthetic Antiferromagnets*, J. Appl. Phys. **127**, 223902 (2020).

[7] J. Igarashi, W. Zhang, Q. Remy, E. Díaz, J.-X. Lin, J. Hohlfeld, M. Hehn, S. Mangin, J. Gorchon, and G. Malinowski, *Optically Induced Ultrafast Magnetization Switching in Ferromagnetic Spin Valves*, Nat. Mater. **22**, 6 (2023).

[8] S. K. Kim, G. S. D. Beach, K.-J. Lee, T. Ono, T. Rasing, and H. Yang, *Ferrimagnetic Spintronics*, Nat. Mater. **21**, 1 (2022).

[9] J. Finley and L. Liu, *Spintronics with Compensated Ferrimagnets*, Appl. Phys. Lett. **116**, 110501 (2020).

[10] M. H. Kryder, E. C. Gage, T. W. McDaniel, W. A. Challener, R. E. Rottmayer, G. Ju, Y.-T. Hsia, and M. F. Erden, *Heat Assisted Magnetic Recording*, Proc. IEEE **96**, 1810 (2008).

[11] M. N. Baibich, J. M. Broto, A. Fert, F. N. Van Dau, F. Petroff, P. Etienne, G. Creuzet, A. Friederich, and J. Chazelas, *Giant Magnetoresistance of (001)Fe/(001)Cr Magnetic Superlattices*, Phys. Rev. Lett. **61**, 2472 (1988).

[12] G. Binasch, P. Grünberg, F. Saurenbach, and W. Zinn, *Enhanced Magnetoresistance in Layered Magnetic Structures with Antiferromagnetic Interlayer Exchange*, Phys. Rev. B **39**, 4828 (1989).

[13] A. Fert, *Nobel Lecture: Origin, Development, and Future of Spintronics*, Rev. Mod. Phys. **80**, 1517 (2008).

[14] U. Hartmann, editor , *Magnetic Multilayers and Giant Magnetoresistance*, Vol. 37 (Springer, Berlin, Heidelberg, 2000).

[15] S. Bhatti, R. Sbiaa, A. Hirohata, H. Ohno, S. Fukami, and S. N. Piramanayagam, *Spintronics Based Random Access Memory: A Review*, Mater. Today **20**, 530 (2017).

[16] J. C. Slonczewski, *Current-Driven Excitation of Magnetic Multilayers*, J. Magn. Magn. Mater. **159**, L1 (1996).

[17] L. Berger, *Emission of Spin Waves by a Magnetic Multilayer Traversed by a Current*, Phys. Rev. B **54**, 9353 (1996).

[18] J. M. Slaughter et al., *High Density ST-MRAM Technology (Invited)*, in *2012 International Electron Devices Meeting* (2012), p. 29.3.1-29.3.4.

[19] E. Beaurepaire, J.-C. Merle, A. Daunois, and J.-Y. Bigot, *Ultrafast Spin Dynamics in Ferromagnetic Nickel*, Phys. Rev. Lett. **76**, 4250 (1996).

[20] B. Koopmans, G. Malinowski, F. Dalla Longa, D. Steiauf, M. Fähnle, T. Roth, M. Cinchetti, and M. Aeschlimann, *Explaining the Paradoxical Diversity of Ultrafast Laser-Induced Demagnetization*, Nat. Mater. **9**, 3 (2010).

[21] M. Wietstruk, A. Melnikov, C. Stamm, T. Kachel, N. Pontius, M. Sultan, C. Gahl, M. Weinelt, H. A. Dürr, and U. Bovensiepen, *Hot-Electron-Driven Enhancement of Spin-Lattice Coupling in Gd and Tb 4f Ferromagnets Observed by Femtosecond X-Ray Magnetic Circular Dichroism*, Phys. Rev. Lett. **106**, 127401 (2011).

[22] N. Bergeard, V. López-Flores, V. Halté, M. Hehn, C. Stamm, N. Pontius, E. Beaurepaire, and C. Boeglin, *Ultrafast Angular Momentum Transfer in Multisublattice Ferrimagnets*, Nat. Commun. **5**, 3466 (2014).

[23] I. Radu et al., *Ultrafast and Distinct Spin Dynamics in Magnetic Alloys*, SPIN **05**, 1550004 (2015).

[24] T. Ferté, N. Bergeard, L. Le Guyader, M. Hehn, G. Malinowski, E. Terrier, E. Otero, K. Holldack, N. Pontius, and C. Boeglin, *Element-Resolved Ultrafast Demagnetization Rates in Ferrimagnetic CoDy*, Phys. Rev. B **96**, 134303 (2017).

[25] T. Ferté, G. Malinowski, E. Terrier, V. Halté, L. L. Guyader, K. Holldack, M. Hehn, C. Boeglin, and N. Bergeard, *Laser Induced Ultrafast 3d and 4f Spin Dynamics in CoDy Ferrimagnetic Alloys as a Function of Temperature*, J. Magn. Magn. Mater. **530**, 167883 (2021).

[26] C. D. Stanciu, F. Hansteen, A. V. Kimel, A. Kirilyuk, A. Tsukamoto, A. Itoh, and Th. Rasing, *All-Optical Magnetic Recording with Circularly Polarized Light*, Phys. Rev. Lett. **99**, 047601 (2007).

[27] I. Radu et al., *Transient Ferromagnetic-like State Mediating Ultrafast Reversal of Antiferromagnetically Coupled Spins*, Nature **472**, 205 (2011).

[28] J. Stohr, *Magnetism* (Springer, Berlin, Heidelberg, 2006).

[29] E. Carpene, E. Mancini, C. Dallera, M. Brenna, E. Puppin, and S. De Silvestri, *Dynamics of Electron-Magnon Interaction and Ultrafast Demagnetization in Thin Iron Films*, Phys. Rev. B **78**, 174422 (2008).

[30] E. G. Tveten, A. Brataas, and Y. Tserkovnyak, *Electron-Magnon Scattering in Magnetic Heterostructures Far out of Equilibrium*, Phys. Rev. B **92**, 180412 (2015).

[31] M. Krauß, T. Roth, S. Alebrand, D. Steil, M. Cinchetti, M. Aeschlimann, and H. C. Schneider, *Ultrafast Demagnetization of Ferromagnetic Transition Metals: The Role of the Coulomb Interaction*, Phys. Rev. B **80**, 180407 (2009).

[32] M. Battiato, K. Carva, and P. M. Oppeneer, *Superdiffusive Spin Transport as a Mechanism of Ultrafast Demagnetization*, Phys. Rev. Lett. **105**, 027203 (2010).

[33] E. Turgut et al., *Controlling the Competition between Optically Induced Ultrafast Spin-Flip Scattering and Spin Transport in Magnetic Multilayers*, Phys. Rev. Lett. **110**, 197201 (2013).

[34] M. L. M. Lalieu, P. L. J. Helgers, and B. Koopmans, *Absorption and Generation of Femtosecond Laser-Pulse Excited Spin Currents in Noncollinear Magnetic Bilayers*, Phys. Rev. B **96**, 014417 (2017).

[35] J. H. Mentink, J. Hellsvik, D. V. Afanasiev, B. A. Ivanov, A. Kirilyuk, A. V. Kimel, O. Eriksson, M. I. Katsnelson, and Th. Rasing, *Ultrafast Spin Dynamics in Multisublattice Magnets*, Phys. Rev. Lett. **108**, 057202 (2012).

[36] G.-M. Choi, B.-C. Min, K.-J. Lee, and D. G. Cahill, *Spin Current Generated by Thermally Driven Ultrafast Demagnetization*, Nat. Commun. **5**, 4334 (2014).

[37] A. Eschenlohr, M. Battiato, P. Maldonado, N. Pontius, T. Kachel, K. Holldack, R. Mitzner, A. Föhlisch, P. M. Oppeneer, and C. Stamm, *Ultrafast Spin Transport as Key to Femtosecond Demagnetization*, Nat. Mater. **12**, 332 (2013).

[38] B. Vodungbo et al., *Indirect Excitation of Ultrafast Demagnetization*, Sci. Rep. **6**, 18970 (2016).

[39] N. Bergeard, M. Hehn, S. Mangin, G. Lengaigne, F. Montaigne, M. L. M. Lalieu, B. Koopmans, and G. Malinowski, *Hot-Electron-Induced Ultrafast Demagnetization in Co / Pt Multilayers*, Phys. Rev. Lett. **117**, 147203 (2016).

[40] N. Bergeard, M. Hehn, K. Carva, P. Baláž, S. Mangin, and G. Malinowski, *Tailoring Femtosecond Hot-Electron Pulses for Ultrafast Spin Manipulation*, Appl. Phys. Lett. **117**, 222408 (2020).

[41] T. Ferté, N. Bergeard, G. Malinowski, E. Terrier, L. Le Guyader, K. Holldack, M. Hehn, and C. Boeglin, *Ultrafast Demagnetization in Buried Co80Dy20 as Fingerprint of Hot-Electron Transport*, J. Magn. Magn. Mater. **485**, 320 (2019).

[42] T. A. Ostler et al., *Ultrafast Heating as a Sufficient Stimulus for Magnetization Reversal in a Ferrimagnet*, Nat. Commun. **3**, 666 (2012).

[43] A. Kirilyuk, A. V. Kimel, and T. Rasing, *Laser-Induced Magnetization Dynamics and Reversal in Ferrimagnetic Alloys*, Rep. Prog. Phys. **76**, 026501 (2013).

[44] L. Avilés-Félix et al., *Single-Shot All-Optical Switching of Magnetization in Tb/Co Multilayer-Based Electrodes*, Sci. Rep. **10**, 5211 (2020).

[45] T. Ferte, N. Bergeard, G. Malinowski, R. Abrudan, T. Kachel, K. Holldack, M. Hehn, and C. Boeglin, *Ultrafast Hot-Electron Induced Quenching of Tb 4 f Magnetic Order*, Phys. Rev. B **96**, 144427 (2017).

[46] S. A. Siddiqui, J. Sklenar, K. Kang, M. J. Gilbert, A. Schleife, N. Mason, and A. Hoffmann, *Metallic Antiferromagnets*, J. Appl. Phys. **128**, 040904 (2020).

[47] S. Mangin et al., *Engineered Materials for All-Optical Helicity-Dependent Magnetic Switching*, Nat. Mater. **13**, 3 (2014).

[48] Y. Xu, M. Hehn, W. Zhao, X. Lin, G. Malinowski, and S. Mangin, *From Single to Multiple Pulse All-Optical Switching in GdFeCo Thin Films*, Phys. Rev. B **100**, 064424 (2019).

[49] J. Hintermayr, A. Ullrich, and M. Albrecht, *Structure and Magnetic Properties of Ferrimagnetic [Gd/Fe]n Multilayer and GdxFe100−x Thin Films*, AIP Adv. **11**, 095214 (2021).

[50] R. Chimata et al., *All-Thermal Switching of Amorphous Gd-Fe Alloys: Analysis of Structural Properties and Magnetization Dynamics*, Phys. Rev. B **92**, 094411 (2015).

[51] O. Eriksson, A. Bergman, L. Bergqvist, and J. Hellsvik, *Atomistic Spin Dynamics: Foundations and Applications* (Oxford university press, 2017).

[52] J. Stöhr and H. Siegmann, *From Fundamentals to Nanoscale Dynamics*, Magn. Fundam. Nanoscale Dyn. J Stöhr HC Siegmann Springer Ser. Solid-State Phys. Vol 152 Berl. Springer 2006 **152**, (2006).

[53] I. A. Campbell, *Indirect Exchange for Rare Earths in Metals*, J. Phys. F Met. Phys. **2**, L47 (1972).

[54] A. Vaterlaus, T. Beutler, and F. Meier, *Spin-Lattice Relaxation Time of Ferromagnetic Gadolinium Determined with Time-Resolved Spin-Polarized Photoemission*, Phys. Rev. Lett. **67**, 3314 (1991).

[55] J. Hohlfeld, S.-S. Wellershoff, J. Güdde, U. Conrad, V. Jähnke, and E. Matthias, *Electron and Lattice Dynamics Following Optical Excitation of Metals*, Chem. Phys. **251**, 237 (2000).

[56] C. E. Graves, Nanoscale Spin Reversal and Magnetization Growth in GdFeCo Studied by Ultrafast Time-Resolved X-Ray Diffraction, PhD Thesis, Stanford University, 2014.

[57] S. D. Brorson, A. Kazeroonian, J. S. Moodera, D. W. Face, T. K. Cheng, E. P. Ippen, M. S. Dresselhaus, and G. Dresselhaus, *Femtosecond Room-Temperature Measurement of the Electron-Phonon Coupling Constant \ensuremath{\gamma} in Metallic Superconductors*, Phys. Rev. Lett. **64**, 2172 (1990).

[58] A. Kirilyuk, A. V. Kimel, and T. Rasing, *Ultrafast Optical Manipulation of Magnetic Order*, Rev. Mod. Phys. **82**, 2731 (2010).

[59] M. Pankratova, I. P. Miranda, D. Thonig, M. Pereiro, E. Sjöqvist, A. Delin, O. Eriksson, and A. Bergman, *Heat-Conserving Three-Temperature Model for Ultrafast Demagnetization in Nickel*, Phys. Rev. B **106**, 174407 (2022).

[60] C. Stamm et al., *Femtosecond Modification of Electron Localization and Transfer of Angular Momentum in Nickel*, Nat. Mater. **6**, 740 (2007).

[61] D. Rudolf et al., *Ultrafast Magnetization Enhancement in Metallic Multilayers Driven by Superdiffusive Spin Current*, Nat. Commun. **3**, 1 (2012).

[62] A. J. Schellekens, W. Verhoeven, T. N. Vader, and B. Koopmans, *Investigating the Contribution of Superdiffusive Transport to Ultrafast Demagnetization of Ferromagnetic Thin Films*, Appl. Phys. Lett. **102**, 252408 (2013).

[63] M. Hofherr et al., *Speed and Efficiency of Femtosecond Spin Current Injection into a Nonmagnetic Material*, Phys. Rev. B **96**, 100403 (2017).

[64] K. Bühlmann, G. Saerens, A. Vaterlaus, and Y. Acremann, *Detection of Femtosecond Spin Injection into a Thin Gold Layer by Time and Spin Resolved Photoemission*, Sci. Rep. **10**, 1 (2020).

[65] T. Kampfrath et al., *Terahertz Spin Current Pulses Controlled by Magnetic Heterostructures*, Nat. Nanotechnol. **8**, 256 (2013).

[66] S. Bonetti, *X-Ray Imaging of Spin Currents and Magnetisation Dynamics at the Nanoscale*, J. Phys. Condens. Matter **29**, 133004 (2017).

[67] *Renesas Develops Embedded MRAM Macro That Achieves over 200MHz Fast Random-Read Access and a 10.4 MB/s Fast Write Throughput for High Performance MCUs | Renesas*, https://www.renesas.com/us/en/about/press-room/renesas-develops-embedded-mram-macro-achieves-over-200mhz-fast-random-read-access-and-104-mbs-fast.

[68] G.-M. Choi, C.-H. Moon, B.-C. Min, K.-J. Lee, and D. G. Cahill, *Thermal Spin-Transfer Torque Driven by the Spin-Dependent Seebeck Effect in Metallic Spin-Valves*, Nat. Phys. **11**, 7 (2015).

[69] A. Alekhin et al., *Femtosecond Spin Current Pulses Generated by the Nonthermal Spin-Dependent Seebeck Effect and Interacting with Ferromagnets in Spin Valves*, Phys. Rev. Lett. **119**, 017202 (2017).

[70] G.-M. Choi and B.-C. Min, *Laser-Driven Spin Generation in the Conduction Bands of Ferrimagnetic Metals*, Phys. Rev. B **97**, 014410 (2018).

[71] T. Ferté, Dynamique ultrarapide de l'aimantation dans les alliages de métaux de transitions et de terres rares, phdthesis, Université de Strasbourg, 2017.

[72] H. Tanaka, S. Takayama, and T. Fujiwara, *Electronic-Structure Calculations for Amorphous and Crystalline Gd 33 Fe 67 Alloys*, Phys. Rev. B **46**, 7390 (1992).

[73] J. H. Mentink, J. Hellsvik, D. V. Afanasiev, B. A. Ivanov, A. Kirilyuk, A. V. Kimel, O. Eriksson, M. I. Katsnelson, and Th. Rasing, *Ultrafast Spin Dynamics in Multisublattice Magnets*, Phys. Rev. Lett. **108**, 057202 (2012).

[74] C. S. Davies, T. Janssen, J. H. Mentink, A. Tsukamoto, A. V. Kimel, A. F. G. van der Meer, A. Stupakiewicz, and A. Kirilyuk, *Pathways for Single-Shot All-Optical Switching of Magnetization in Ferrimagnets*, Phys. Rev. Appl. **13**, 024064 (2020).

[75] M. Faraday, *On the Magnetization of Light and the Illumination of Magnetic Lines of Force c. 1* (The Royal Society, 1846).

[76] J. Kerr, *On Rotation of the Plane of Polarization by Reflection from the Pole of a Magnet*, Lond. Edinb. Dublin Philos. Mag. J. Sci. **3**, 321 (1877).

[77] H. Ebert, *Magneto-Optical Effects in Transition Metal Systems*, Rep. Prog. Phys. **59**, 1665 (1996).

[78] B. T. Thole, P. Carra, F. Sette, and G. Van Der Laan, *X-Ray Circular Dichroism as a Probe of Orbital Magnetization*, Phys. Rev. Lett. **68**, 1943 (1992).

[79] P. Carra, B. T. Thole, M. Altarelli, and X. Wang, *X-Ray Circular Dichroism and Local Magnetic Fields*, Phys. Rev. Lett. **70**, 694 (1993).

[80] J. L. Erskine and E. A. Stern, *Magneto-Optic Kerr Effects in Gadolinium*, Phys. Rev. B **8**, 1239 (1973).

[81] P. Hansen, C. Clausen, G. Much, M. Rosenkranz, and K. Witter, *Magnetic and Magneto-optical Properties of Rare-earth Transition-metal Alloys Containing Gd, Tb, Fe, Co*, J. Appl. Phys. **66**, 756 (1989).

[82] R.-M. Abrudan and F. Radu, *ALICE: A Diffractometer/Reflectometer for Soft X-Ray Resonant Magnetic Scattering at BESSY II*, J. Large-Scale Res. Facil. JLSRF **2**, A69 (2016).

[83] M. G. Silly et al., *Pump−probe Experiments at the TEMPO Beamline Using the Low-α Operation Mode of Synchrotron SOLEIL*, J. Synchrotron Radiat. **24**, 886 (2017).

[84] M. Pacé et al., *Laser Induced Ultrafast Gd 4f Spin Dynamics at the Surface of Amorphous CoxGd100-x Ferrimagnetic Alloys*, J. Electron Spectrosc. Relat. Phenom. **275**, 147461 (2024).

[85] A. A. Zholents and M. S. Zolotorev, *Femtosecond X-Ray Pulses of Synchrotron Radiation*, Phys. Rev. Lett. **76**, 912 (1996).

[86] K. Holldack et al., *FemtoSpeX: A Versatile Optical Pump–Soft X-Ray Probe Facility with 100 Fs X-Ray Pulses of Variable Polarization*, J. Synchrotron Radiat. **21**, 1090 (2014).

[87] K. Carva, D. Legut, and P. M. Oppeneer, *Influence of Laser-Excited Electron Distributions on the X-Ray Magnetic Circular Dichroism Spectra: Implications for Femtosecond Demagnetization in Ni*, Europhys. Lett. **86**, 57002 (2009).

[88] C. Boeglin, E. Beaurepaire, V. Halté, V. López-Flores, C. Stamm, N. Pontius, H. A. Dürr, and J.-Y. Bigot, *Distinguishing the Ultrafast Dynamics of Spin and Orbital Moments in Solids*, Nature **465**, 458 (2010).

[89] D. Schick, S. Eckert, N. Pontius, R. Mitzner, A. Föhlisch, K. Holldack, and F. Sorgenfrei, *Versatile Soft X-Ray-Optical Cross-Correlator for Ultrafast Applications*, Struct. Dyn. **3**, 054304 (2016).

[90] K.-H. Ko and G.-M. Choi, *Optical Method of Determining the Spin Diffusion Length of Ferromagnetic Metals*, J. Magn. Magn. Mater. **510**, 166945 (2020).

[91] S. J. Byrnes, *Multilayer Optical Calculations*, (2020).

[92] T. Ferté et al., *Laser Induced Ultrafast Gd 4f Spin Dynamics in Co100-xGdx Alloys by Means of Time-Resolved XMCD*, Eur. Phys. J. Spec. Top. **232**, 2213 (2023).

[93] Y. Mimura, N. Imamura, T. Kobayashi, A. Okada, and Y. Kushiro, *Magnetic Properties of Amorphous Alloy Films of Fe with Gd, Tb, Dy, Ho, or Er*, J. Appl. Phys. **49**, 1208 (2008).

[94] Q. Remy, Ultrafast Spin Dynamics and Transport in Magnetic Metallic Heterostructures, phdthesis, Université de Lorraine, 2021.

[95] R. Abrudan, F. Brüssing, R. Salikhov, J. Meermann, I. Radu, H. Ryll, F. Radu, and H. Zabel, *ALICE – An Advanced Reflectometer for Static and Dynamic Experiments in Magnetism at Synchrotron Radiation Facilities*, Rev. Sci. Instrum. **86**, 063902 (2015).

[96] L. J. Tao, R. J. Gambino, S. Kirkpatrick, J. J. Cuomo, and H. Lilienthal, *Magnetic Properties of Amorphous GdCo Films*, AIP Conf. Proc. **18**, 641 (1974).

[97] J. Aboaf, S. Herd, and E. Klokholm, *Magnetic Properties and Structure of Cobalt-Platinum Thin Films*, IEEE Trans. Magn. **19**, 1514 (1983).

[98] N. Bergeard, A. Mougin, M. Izquierdo, E. Fonda, and F. Sirotti, *Correlation between Structure, Electronic Properties, and Magnetism in Co x Gd 1 − x Thin Amorphous Films*, Phys. Rev. B **96**, 064418 (2017).

[99] H. J. Leamy and A. G. Dirks, *The Microstructure of Amorphous Rare-Earth/Transition-Metal Thin Films*, J. Phys. Appl. Phys. **10**, L95 (1977).

[100] N. Bergeard, Matériaux magnétiques pour l'étude de la dynamique de l'aimantation, phdthesis, Université Paris Sud - Paris XI, 2010.

[101] R. C. Taylor and A. Gangulee, *Magnetization and Magnetic Anisotropy in Evaporated GdCo Amorphous Films*, J. Appl. Phys. **47**, 4666 (2008).

[102] T. Lichtenberg, M. Beens, M. H. Jansen, B. Koopmans, and R. A. Duine, *Probing Optically Induced Spin Currents Using Terahertz Spin Waves in Noncollinear Magnetic Bilayers*, Phys. Rev. B **105**, 144416 (2022).

[103] C. E. Graves et al., *Nanoscale Spin Reversal by Non-Local Angular Momentum Transfer Following Ultrafast Laser Excitation in Ferrimagnetic GdFeCo*, Nat. Mater. **12**, 293 (2013).

[104] A. Meo, C. E. Cronshaw, S. Jenkins, A. Lees, and R. F. L. Evans, *Spin-Transfer and Spin-Orbit Torques in the Landau–Lifshitz–Gilbert Equation*, J. Phys. Condens. Matter **35**, 025801 (2022).

[105] M. Pankratova, I. P. Miranda, D. Thonig, M. Pereiro, E. Sjoqvist, A. Delin, P. Scheid, O. Eriksson, and A. Bergman, *Heat-Conserving Three-Temperature Model for Ultrafast Demagnetization of 3d Ferromagnets*, arXiv:2308.08996.

[106] Q. Remy, J. Hohlfeld, M. Vergès, Y. Le Guen, J. Gorchon, G. Malinowski, S. Mangin, and M. Hehn, *Accelerating Ultrafast Magnetization Reversal by Non-Local Spin Transfer*, Nat. Commun. **14**, 1 (2023).

[107] D. Liu, C. Jiang, H. Li, and C. Xu, *Dependence of the Gd Concentration Range for Thermally Induced Magnetization Switching on the Intrinsic Damping*, Appl. Phys. Lett. **122**, 202406 (2023).

[108] D. Gupta et al., *Tuning of the Ultrafast Demagnetization by Ultrashort Spin Polarized Currents in Multi-Sublattice Ferrimagnets*, arXiv:2403.11739.

[109] U. Atxitia, J. Barker, R. W. Chantrell, and O. Chubykalo-Fesenko, *Controlling the Polarity of the Transient Ferromagneticlike State in Ferrimagnets*, Phys. Rev. B **89**, 224421 (2014).

[110] V. López-Flores, N. Bergeard, V. Halté, C. Stamm, N. Pontius, M. Hehn, E. Otero, E. Beaurepaire, and C. Boeglin, *Role of Critical Spin Fluctuations in Ultrafast Demagnetization of Transition-Metal Rare-Earth Alloys*, Phys. Rev. B **87**, 214412 (2013).

[111] A. Eschenlohr, M. Sultan, A. Melnikov, N. Bergeard, J. Wieczorek, T. Kachel, C. Stamm, and U. Bovensiepen, *Role of Spin-Lattice Coupling in the Ultrafast Demagnetization of Gd 1 − x Tb x Alloys*, Phys. Rev. B **89**, 214423 (2014).

[112] D. J. Higley et al., *Femtosecond X-Ray Magnetic Circular Dichroism Absorption Spectroscopy at an X-Ray Free Electron Laser*, Rev. Sci. Instrum. **87**, 033110 (2016).

[113] M. Hennecke, I. Radu, R. Abrudan, T. Kachel, K. Holldack, R. Mitzner, A. Tsukamoto, and S. Eisebitt, *Angular Momentum Flow During Ultrafast Demagnetization of a Ferrimagnet*, Phys. Rev. Lett. **122**, 157202 (2019).

[114] A. Jablonski, *C. J. Powell, Surface and Microanalysis Science Division National Institute of Standards and Technology Gaithersburg, MD, USA*, (n.d.).

[115] J. J. Yeh and I. Lindau, *Atomic Subshell Photoionization Cross Sections and Asymmetry Parameters: 1 ⩽ Z ⩽ 103*, At. Data Nucl. Data Tables **32**, 1 (1985).

[116] L. Z. Mezey and J. Giber, *The Surface Free Energies of Solid Chemical Elements: Calculation from Internal Free Enthalpies of Atomization*, Jpn. J. Appl. Phys. **21**, 1569 (1982).

[117] E. Jal, V. López-Flores, N. Pontius, T. Ferté, N. Bergeard, C. Boeglin, B. Vodungbo, J. Lüning, and N. Jaouen, *Structural Dynamics during Laser-Induced Ultrafast Demagnetization*, Phys. Rev. B **95**, 184422 (2017).

[118] M. Hennecke et al., *Ultrafast Element- and Depth-Resolved Magnetization Dynamics Probed by Transverse Magneto-Optical Kerr Effect Spectroscopy in the Soft x-Ray Range*, Phys. Rev. Res. **4**, L022062 (2022).

[119] P. Johnson and R. Christy, *Optical Constants of Transition Metals: Ti, V, Cr, Mn, Fe, Co, Ni, and Pd*, Phys. Rev. B **9**, 5056 (1974).

[120] Haynes, W. M., editor *Handbook of Chemistry and Physics*, CRC Press, 96 edition (2015-2016)

Appendix

Refractive index values for TMM calculations:

Elements	**Refractive index (800 nm)**
Pt	2.83 + 4.95 *i* [120]
Cu	0.26 + 5.26 *i* [120]
Co	2.53 + 4.88 *i* [119]
Fe	2.94 + 3.39 *i* [119]
Ta	1.09 + 3.73 *i* [120]

Table I: Refractive indices at 800 nm wavelength used to calculate the absorption profile.

Fitting procedure and parameters:

To quantify the characteristic parameters of dynamics, data was fitted using double exponential equation, given by:

$$F(t) = G(t - t_0) * [y_0 + A \times H(t - t_0)\left(1 - e^{-\frac{(t-t_0)}{\tau_d}}\right) \times (e^{-\frac{(t-t_0)}{t_{r1}}} + e^{-\frac{(t-t_0)}{t_{r2}}})]$$

In this fitting equation, G(t) is the Gaussian function, which involves the experimental time resolution of 130 fs by considering the pulse width of IR laser (60 fs) and X-ray pulses (100 fs). H(t), is the Heaviside function (H(t) = 0 if t = 0, and H(t) = 1 if t > 0), illustrates the starting of dynamics. The parameters, y_0 and A, represents the value of XMCD at the negative delay, and the demagnetization amplitude, which is the amount of energy transferred to the system. Two exponentials correspond to the demagnetization and recovery, respectively. τ_d, and t_{r1} represents the characteristic ultrafast demagnetization time and the fast recovery. t_{r2} is the second slow recovery, which corresponds to the lattice thermal equilibration time. t_0, represents the temporal overlap, when both IR and X-ray pulses overlap.

Estimation of hot electron pulse elongation

Gaussian pulse width was estimated by using above fitting equation. From fitting we obtained G(t) = 420 fs. This fitting was extended for different pulse duration and recorded the change in χ^2.

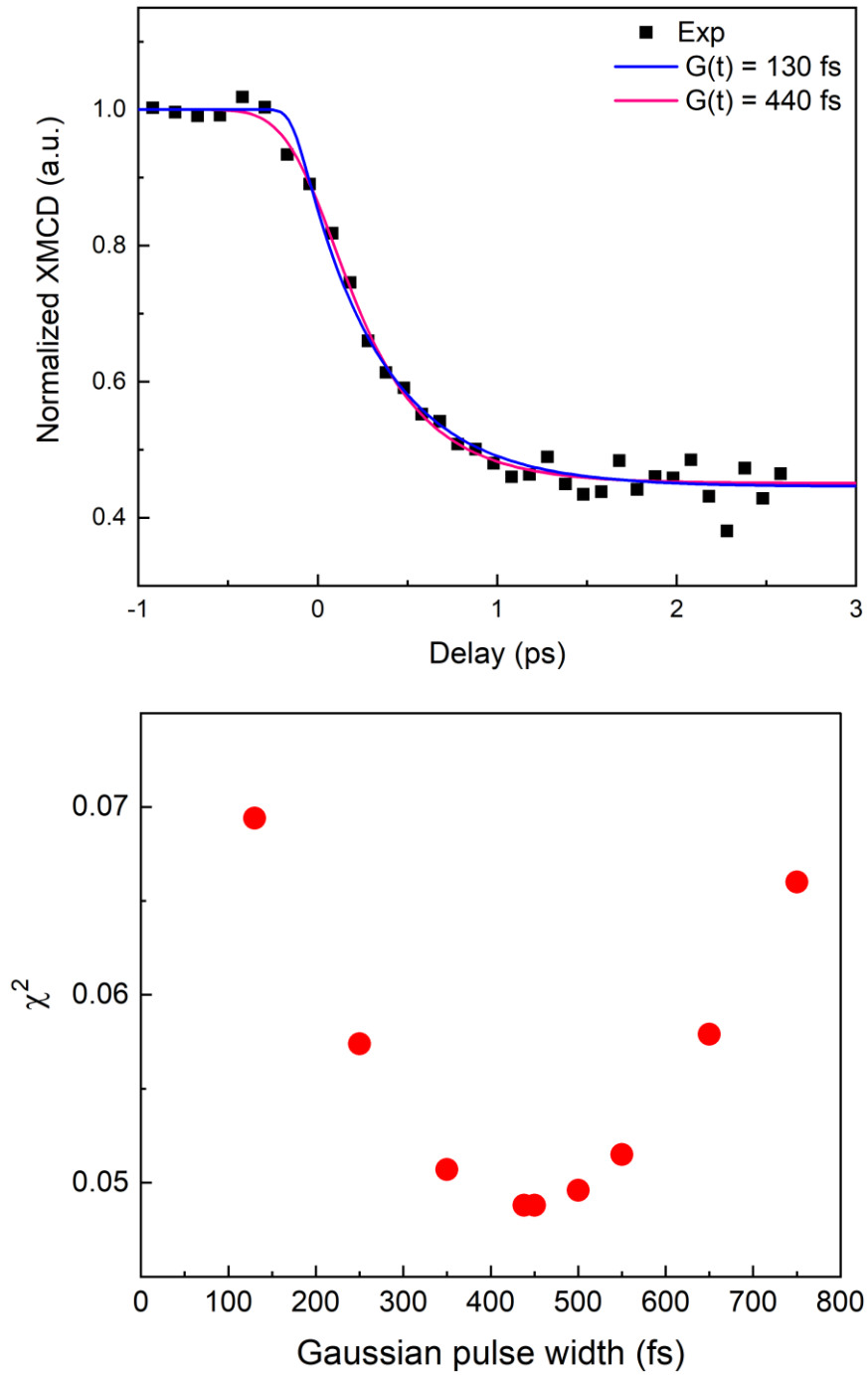

Figure I: (a) Fittings with the G(t) = 130 fs (magenta) and 440 fs (blue). (b) Variation of χ^2 with the Gaussian pulse width G(t).

Figure I(a) show the fitting with the two different G(t) values (130 fs and 440 fs). The variation of χ^2 with the different Gaussian pulse width is shown in Figure I(b). Its clear from the Figure I(b) that minima of χ^2 lies values within range of 350 – 500 fs. Therefore, we estimated pulse width of 420 ± 80 fs, by considering the 20% uncertainty from the minimum value.

Résumé

1.1 Introduction

La démonstration théorique de l'existence de l'état quantique de spin des électrons remonte déjà à une centaine d'années. Depuis lors, les domaines magnétiques ont montré leur importance dans de nombreux domaines de recherche. L'une des applications les plus importantes de nos jours est la technologie moderne de l'information pour les supports d'enregistrement magnétiques. Il y a plus de 60 ans, la manipulation conventionnelle par des champs magnétiques externes était utilisée dans les disques durs (HDD) par enregistrement magnétique thermiquement assisté (HAMR) [1]. L'augmentation de la capacité de stockage des données et l'accélération des temps d'accès entraînent non seulement une réduction des dimensions des domaines codant l'information, mais aussi la nécessité de temps d'accès plus rapides.

Dans ce contexte, la découverte de la magnétorésistance géante (GMR) par Albert Fert [2] et Peter Grünberg [3] en 1988 a constitué une révolution dans l'industrie de l'enregistrement. Cette découverte a marqué le début d'une nouvelle ère dans le magnétisme moderne, appelée la spintronique [4,5]. Il a été démontré que la résistivité changeait par le biais du mécanisme de diffusion dépendant du spin entre deux couches magnétiques parallèles-antiparallèles dans les structures à vanne de spin. Ces travaux ont donné lieu à de nouveaux développements, par exemple la mémoire à accès aléatoire magnétorésistive (MRAM) [6].

Parallèlement, l'écriture magnétique a été développée à l'aide de différentes méthodes, telles que la commutation de nanodomaines magnétiques induite par le champ, le courant et la lumière. L'avantage des dispositifs à induction électronique par rapport aux dispositifs conventionnels à champ magnétique réside dans leur faible consommation d'énergie, l'un des problèmes les plus actuels. Étant donné que les besoins actuels exigent également un temps de traitement plus rapide au coût le plus bas possible, de nouveaux concepts combinent des méthodes induites par le courant et la lumière basées sur des impulsions ultracourtes de courants polarisés en spin, introduisant le concept de couple de transfert de spin (STT) dans les structures de vannes de spin [7,8]. Les dispositifs basés sur le STT sont commercialisés depuis 2016 [9], et le temps de commutation peut être rapide, jusqu'à 200 ps [4], mais au prix d'une réduction de la durée de l'impulsion, et donc de l'énergie de commutation. Malgré tous les processus de commutation susmentionnés

utilisés dans les dispositifs de mémoire, tous ces effets tournent autour d'un élément crucial: le courant de spin. Il est essentiel de comprendre sa génération, son optimisation et son interaction avec d'autres couches magnétiques pour continuer à améliorer la technologie.

La même année que la découverte du concept STT, en 1996, la découverte de la dynamique de désaimantation ultrarapide par Bigot et Beaurepaire a ouvert un nouveau champ de recherche en magnétisme appelé femtomagnétisme. Ils ont observé qu'en envoyant une impulsion laser IR, l'aimantation d'un film de Ni peut être annihilé en moins de 1 ps [10]. Cette découverte a donné lieu à de nombreuses expériences confirmant la dynamique ultrarapide de l'aimantation dans divers matériaux, y compris les ferromagnétiques classiques à base de métaux de transition tels que le Fe, le Ni et le Co [11], ainsi que les éléments à base de terres rares (Gd, Tb, Dy) [11,12] et les alliages associés présentant une anisotropie hors du plan [13-16].

Une étude de Stanciu et al. a montré que l'aimantation d'un alliage ferrimagnétique GdCoFe peut être inversée à l'aide d'un laser polarisé circulaire d'une durée de 40 fs sans appliquer de champ magnétique [17]. Ce phénomène, connu sous le nom de commutation tout optique dépendante de l'hélicité (HD-AOS), permet une commutation déterministe à l'aide d'une lumière polarisée circulairement gauche ou droite [17]. Peu après, Radu et al. ont montré que même une lumière polarisée linéairement pouvait induire le renversement de l'aimantation dans les alliages GdCoFe, introduisant ainsi le concept de commutation tout optique indépendante de l'hélicité (HI-AOS) [18].

Outre leur importance technologique, l'exploration des matériaux à l'échelle de temps femto-picoseconde offre des perspectives intrigantes d'un point de vue fondamental. Cette échelle de temps particulière correspond aux interactions magnétiques fondamentales telles que l'interaction d'échange, le couplage spin-orbite et l'anisotropie magnétique [19]. Plusieurs mécanismes ont été proposés pour élucider la perte d'aimantation à l'échelle de temps fs, notamment le modèle à trois températures de Beaurepaire et Bigot [10] ainsi que plusieurs mécanismes locaux [11,20-22] et non locaux [23,24]. Parmi eux, le mécanisme non local, introduit par Battiato et al. et connu sous le nom de transport de spin superdiffusif, explique que la perte d'aimantation lors de l'excitation laser est due à la migration des électrons excités par le laser dans la couche métallique adjacente [23]. Ce processus a généré le courant de spin superdiffusif (SC) dans le régime ultrarapide en raison du libre parcours moyen des électrons excités dépendant du spin. Avant de développer ce modèle superdiffusif, Malinowski et al. avaient démontré expérimentalement le transport du moment angulaire du spin lors de l'excitation laser dans une structure multicouche magnétique [25]. Par la suite, différents groupes ont

utilisé le concept de courant de spin superdiffusif pour manipuler l'aimantation de couches magnétiques adjacentes [26-30], ainsi que pour générer des impulsions de courant de spin dans la gamme THz [31]. Récemment, les travaux d'Igarashi et de ses collaborateurs [32] ont montré que la commutation dans une structure de vanne de spin ferromagnétique était inférieure à une picoseconde, même avec l'utilisation de 80 nm de Cu entre deux couches magnétiques, fusionnant ainsi la spintronique et le femtomagnétisme. Ils ont observé que l'orientation antiparallèle des deux couches magnétiques dans la vanne de spin favorise la commutation de la couche molle induite par les électrons chauds (HE) [29,32]. De manière surprenante, d'autres résultats contre-intuitifs ont révélé que certains systèmes de vanne de spin ne présentent une commutation de la couche molle que pour une orientation parallèle entre la couche dure et molle [35]. Ces résultats concluent que l'orientation permettant une commutation réussie dépend de la fluence dans un système de vanne de spin donné, ce qui soulève à nouveau des questions sur les multiples mécanismes à l'origine de la commutation de spin.

Des études utilisant la résolution temporelle des rayons X et permettant de distinguer les éléments chimiques et leur aimantation, ont montré que les électrons chauds induits par laser peuvent être utilisés comme excitations indirectes de la désaimantation ultrarapide dans le Ni [33], travail qui a été suivi par beaucoup d'autres [34-36]. Jusqu'à présent, ces études ont également pris en compte différents ferro-aimants, y compris les alliages TM-RE [15,37]. Cependant, aucun effet de polarisation du spin dans la désaimantation induite par l'HE n'a encore été étudié dans les alliages 4f RE et TM-RE. C'est l'une des motivations de mon travail de thèse, qui se concentre sur la description de la démagnétisation ultrarapide induite par un courant polarisé en spin avec sélectivité des éléments dans les fer-aimants RE-TM, des matériaux importants permettant de faire progresser la spintronique et le stockage de données magnétiques vers le régime temporelle sub-picoseconde. Ces matériaux font également partie des systèmes qui présentent une commutation tout optique à impulsion unique, une propriété importante pour les applications utilisant la spintronique ultrarapide [17,18,38-40]

1.2 Motivation de ce travail de thèse

Jusqu'à présent, plusieurs expériences ont étudié la dynamique de spin ultrarapide induite par de tels courants de spin fs dans des structures à vanne de spin [25,27,29]. Cependant, ces travaux étaient axés sur l'excitation directe des multicouches magnétique et la couche intercalaire était trop fine pour éviter l'excitation de la couche magnétique inférieure, ce qui a rendu complexe l'étude

isolée du courant de spin. Une autre approche peut consister à bloquer la lumière IR et à utiliser des impulsions HE [33-37,41] pour exciter la structure magnétique et polariser le courant HE avant la couche de détection. Cependant, ces travaux se concentrent sur les métaux de transition ferromagnétiques 3d. Des études récentes suggèrent que les matériaux antiferromagnétiques (AFM) sont plus prometteurs pour le contrôle de l'aimantation ultrarapide dans les dispositifs spintroniques ultrarapides [42]. Parmi ces matériaux AFM, les alliages terres rares/métaux de transition (RE-TM) représentent des systèmes modèles [43]. Au cours des dernières années, de nombreuses études ont été menées pour observer **AOS** dans ces types de systèmes modèles [18,44,45]. En raison de la dépendance à la température différente de deux sous-réseaux magnétiques, c'est-à-dire les moments 3d et 4f, les deux sous-réseaux possèdent des dynamiques différentes lorsqu'ils sont excités avec des systèmes laser IR intenses.

En outre, ces alliages présentent diverses propriétés électroniques et magnétiques lorsque l'on modifie la concentration atomique et la température [46,47]. Par conséquent, l'étude de ces matériaux est cruciale pour l'ingénierie des différents matériaux en vue de faire progresser les dispositifs magnétiques. Il est donc crucial de comprendre l'impact des courants de spin polarisés sur ces matériaux.

Par conséquent, pour comprendre le comportement du courant de spin, j'étudie ici la dynamique de spin femtoseconde induite par des électrons chauds polarisés dans de tels alliages RE-TM. Pour observer l'effet induit par le courant de spin sur les moments TM 3d et Gd 4f, j'ai utilisé la technique de dichroïsme circulaire magnétique utilisant la résolution temporelle des rayons X , opérationnel sur la ligne de faisceau femtoslicante de HZB-BESSY II, à Berlin. Cette installation à grande échelle fournit des impulsions de rayons X ultra-courtes de ~100 fs comme sonde avec une polarisation circulaire, et leur énergie peut être réglée jusqu'à 1300 eV. Par conséquent, en utilisant cette expérience de pointe, nous pouvons résoudre la dynamique spécifique des éléments dans les systèmes d'alliage RE-TM. En outre, la modélisation théorique basée sur des simulations atomistiques de dynamique de spin [47,48] reproduit la dynamique ultrarapide expérimentale de ce système, ce qui permet d'identifier le processus microscopique de transfert du moment angulaire du spin aux échelle de temps femto- et picoseconde.

1.3 Structure de l'échantillon et dispositif expérimental

La structure de l'échantillon utilisé pour étudier l'effet SPHE (spin-polarized hot electron) est constituée de l'empilement suivant : Si3N4 /Ta(5)/Cu (20)/Ta (5)/FM2(15)/Cu (t)/FM1(t)/Cu (60)/Pt (6), comme le

montre la figure 1. Les valeurs numériques entre parenthèses correspondent à l'épaisseur de chaque couche en nanomètres.

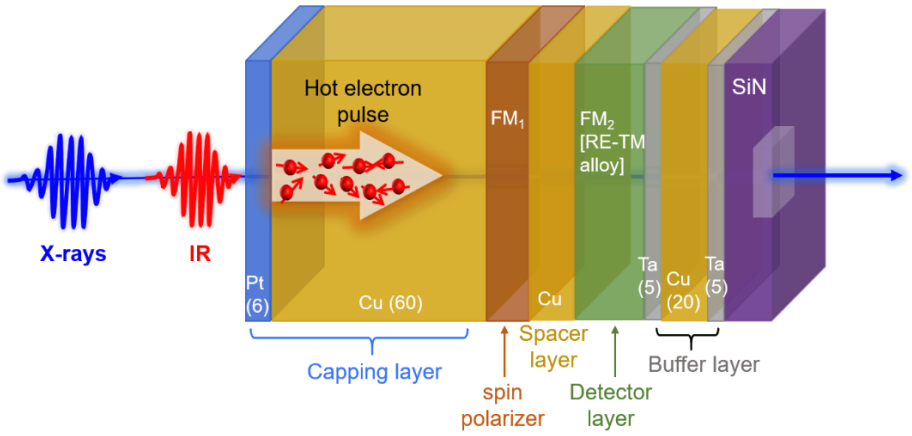

Figure 1 Schéma de la structure de l'échantillon : La structure de l'échantillon utilisé pour étudier la dynamique induite par les électrons chauds polarisés en spin (SPHE) se compose de l'empilement suivant, de droite à gauche : SiN/ Ta (5)/ Cu (20)/ Ta (5)/ FM2 (15)/ Cu (t)/ FM1/Cu(60)/ Pt (6). Les épaisseurs de chaque couche entre parenthèses sont exprimées en nm. La grande flèche dans Cu (60) représente la direction du flux d'électrons chauds, et à l'intérieur, les courts points rouges avec des flèches rouges représentent les électrons chauds non polarisés avec leurs spins aléatoirement orientés.

La couche supérieure de Pt (6)/Cu (60) est excitée par un laser de pompe IR intense (800 nm) pour générer des impulsions d'électrons chauds (HE) ultracourtes. Des travaux antérieurs ont montré que la plupart des HE sont générés dans la couche de Pt, et que l'efficacité de la conversion est optimisée pour une épaisseur de Pt d'environ 6 nm [36]. Les HE sont injectées dans la couche de Cu (60) pour être transportées vers la couche FM1 enterrée. Malgré une efficacité limitée pour la photoexcitation des HE, la couche de Cu (60) a deux fonctions fondamentales : premièrement, elle absorbe l'impulsion IR pour éviter l'excitation IR directe de la couche FM1 et deuxièmement, le Cu (60) assure le transport balistique (c'est-à-dire une perte d'énergie minimale) [35]. Ici, FM1, la première couche magnétique, agit comme un polariseur de spin (couche fixe), et FM2, la seconde, est la couche d'intérêt (couche libre) par laquelle nous voulons étudier l'effet de la SPHE générée par FM1.

Dans ce travail de thèse, les principaux défis consistent à trouver les systèmes appropriés pour l'étude de la SPHE, c'est-à-dire que la première couche FM1 (polariseur de spin) doit avoir une coercivité plus importante que la couche FM2 inférieure. Pour ce faire, nous avons étudié différents alliages

TM-RE et systèmes multicouches magnétiques tels que CoPt, CoGd, FeGd et FeCoGd, de compositions et d'épaisseurs différentes afin d'optimiser la structure de la vanne de spin pour les études SPHE.

Pour optimiser chaque couche, diverses mesures ont été effectuées en laboratoire et dans différentes "Très Grandes Infrastructures de Recherches" (TGIR), telles que la magnétométrie Kerr magnéto-optique (MOKE), la spectroscopie d'absorption des rayons X (XAS), la photoémission des rayons X (XPS), etc.

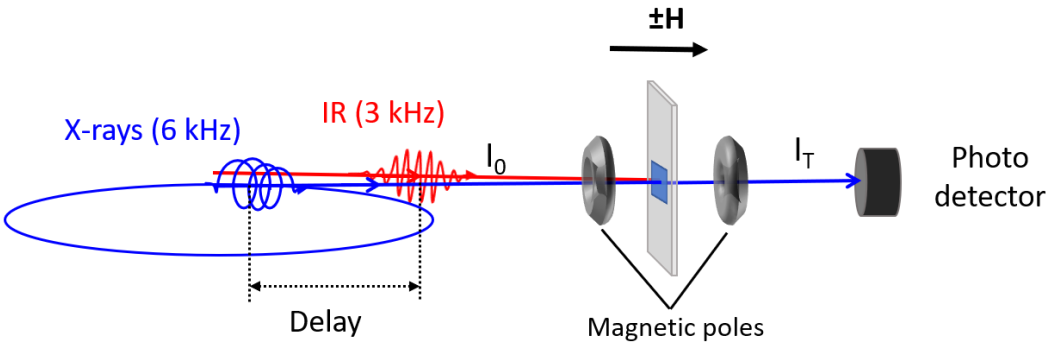

Figure 2 ***Schéma du dispositif expérimental**: Technique de dichroïsme circulaire magnétique des rayons X résolue dans le temps (Tr-XMCD) au synchrotron BESSY II, Berlin* [49].

Pour étudier l'effet de polarisation du spin, les mesures Tr-XMCD ont été réalisées en utilisant la technique pompe-sonde. La figure 2 montre le schéma du dispositif expérimental installé sur la ligne Femtoslicing, HZB-BESSY II, Berlin. Dans cette expérience, un laser IR très intense (800 nm) d'une largeur d'impulsion de 60 fs avec un taux de répétition de 3 kHz est utilisé comme pompe et des rayons X ultracourts à polarisation circulaire d'une durée de 100 fs avec un taux de répétition de 6 kHz sont utilisés comme sonde. La pompe et la sonde sont toutes deux séparées par un angle de 1°, et l'incident se produit normalement sur l'échantillon. Le spectre d'absorption des rayons X est enregistré dans la géométrie de transmission par un détecteur à photodiode à avalanche. Nous avons enregistré l'intensité des rayons X transmis aux seuils d'absorptions correspondants du niveau du noyau élémentaire : les seuils TM L3 et RE M5. Pour mettre en évidence l'efficacité de ces courants de spin fs par rapport à la démagnétisation thermique pure, nous avons réalisé l'expérience avec un alignement parallèle et antiparallèle de l'aimantation de la couche FM1 et de la couche FM2.

1.4 Dynamique induite par les électrons chauds polarisés en spin dans le système d'alliage FeGd

Dans ce chapitre, nous avons étudié l'impact de l'effet induit par les électrons chauds polarisés en spin (SPHE) sur la désaimantation de la vanne de spin constituée de $Fe_{74}Gd_{26}(15)/Cu/\{Co/Pt\}*3$. Nous avons mesuré le changement de XMCD en fonction du délai pompe-sonde à Fe L_3 (points pleins dans la Fig. 3(a)) et Gd M_5 (points pleins dans la Fig. 3(b)) à une fluence laser de 120 mJ/cm² et 40 mJ/cm² à une température de 80 K au cryostat. Pour distinguer l'effet SPHE de la courbe de démagnétisation thermique, la mesure est effectuée dans deux configurations : L'aimantation du Co est parallèle (P) (courbe bleue) et antiparallèle (AP) (courbe rouge) à l'aimantation du Fe. À courte échelle de temps (Fig. 3 a), c'est-à-dire en dessous de 2,5 ps, nous constatons que la dynamique expérimentale dans le cas parallèle (P) est plus rapide et d'une amplitude légèrement plus grande que dans le cas AP. Le changement observé dans la dynamique de démagnétisation entre les cas P et AP est lié à la différence dans les orientations relatives du spin entre le SPHE et le moment Fe dans le $Fe_{74}Gd_{26}$. Cependant, dans le cas du Gd M_5, dans le niveau de bruit expérimental atteint (Fig. 3 b), il n'y a pas de différence entre les configurations P et AP.

Nous présentons les premiers résultats expérimentaux mettant en évidence les échelles de temps de l'extinction ultrarapide de l'aimantation dans le ferrimagnétique $Fe_{74}Gd_{26}$, induite par des impulsions ultracourtes de courants de spin tels qu'ils sont produits dans une structure de vanne de spin magnétique colinéaire (CoPt/ Cu/ FeGd).

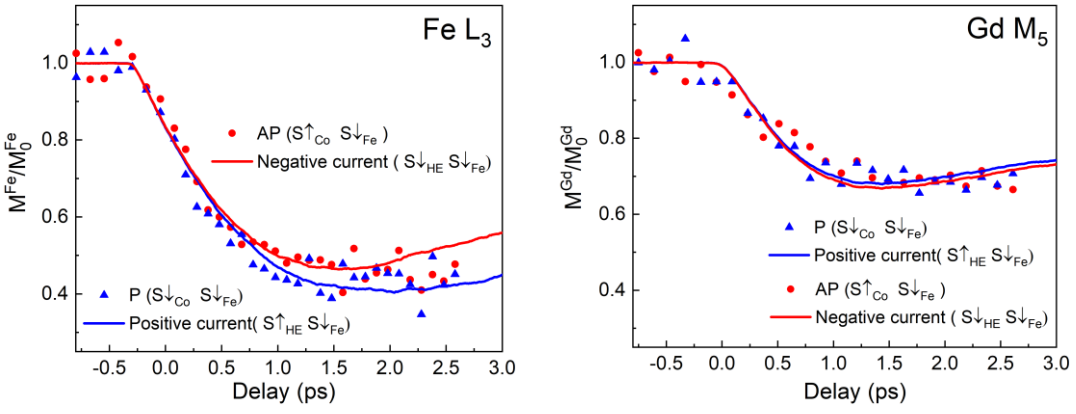

Figure 3 Dynamique de désaimantation expérimentale et simulée par Tr-XMCD et dynamique atomistique du spin du Fe dans le $Fe_{74}Gd_{26}$ pour des fluences incidentes de 120 mJ/cm² et absorbées de 3,2 mJ/cm² (a) et du Gd dans le $Fe_{74}Gd_{26}$ pour des fluences incidentes de 40 mJ/cm² et absorbées de 1,2 mJ/cm² (b). La valeur de la fluence laser a été ajustée pour correspondre à nos données expérimentales. Les symboles

bleus (rouges) sont les résultats expérimentaux pour les configurations P(AP). Les lignes pleines en bleu (rouge) sont les simulations de courant de spin positif (négatif) pour un amortissement de Gilbert a =0,1. Dans les simulations, la polarisation du SPHE est opposée aux moments du Co, comme le montrent les flèches dans les légendes.

Ce travail combine des résultats expérimentaux obtenus à l'aide de la XMCD résolue en temps et des simulations de dynamique de spin atomique basées sur une description théorique de pointe, mettant en évidence la désaimantation induite par l'HE dépendante du spin à l'échelle de temps ultra-courte qui définit les mécanismes microscopiques à l'œuvre. En s'appuyant sur la géométrie et la composition définies expérimentalement ainsi que sur les échanges inter atomiques, la modélisation théorique basée sur des simulations atomistiques de dynamique de spin reproduit la dynamique ultrarapide expérimentale du Fe74Gd26, ce qui permet d'identifier le processus microscopique de transfert du moment angulaire du spin à l'échelle de temps la plus courte. La dynamique simulée (lignes pleines) pour les moments du Fe et du Gd est comparée aux résultats expérimentaux (points de données pleins) dans la figure 3.

Le modèle reproduit les données expérimentales et révèle comment les excitations SPHE conduisent la démagnétisation dans les deux sous-réseaux Fe74Gd26. Il est particulièrement intéressant de noter que les calculs théoriques reproduisent les échelles de temps et les amplitudes des résultats expérimentaux enregistrés aux bords du Fe L3 et du Gd M5, ce qui permet de déterminer indirectement le degré de polarisation du spin dans le courant SPHE. Les calculs théoriques permettent de déterminer la polarisation du spin dans le courant SPHE, qui est opposée à l'aimantation de la multicouche Co/Pt. Cette découverte est nouvelle et surprenante, mais à notre connaissance, nous n'avons aucune indication d'une polarisation de spin bien définie dans de telles multicouches.

Ce modèle peut également être utilisé pour prédire l'impact des variations, en fonction de la fluence, de l'échauffement induit par l'HE et de la STT dans les deux sous-réseaux $Fe_{74}Gd_{26}$.

1.5 Dynamique induite par les électrons chauds polarisés en spin dans le système d'alliage CoGd.

1.4.1 Observation des effets induits par les électrons chauds polarisés en spin

Nous avons effectué la même mesure que celle expliquée dans la section précédente en choisissant la structure d'échantillon suivante : SiN/Ta (5) /Cu (20)/Ta (5) / Co61Gd39 (15) /Cu (4) /Co75Pt25(3) /Cu (60) /Pt (6). La dynamique a été mesurée dans les orientations parallèles et antiparallèles de l'aimantation du CoPt et du CoGd à une fluence de 60 mJ/cm2, comme le montre la figure 4.

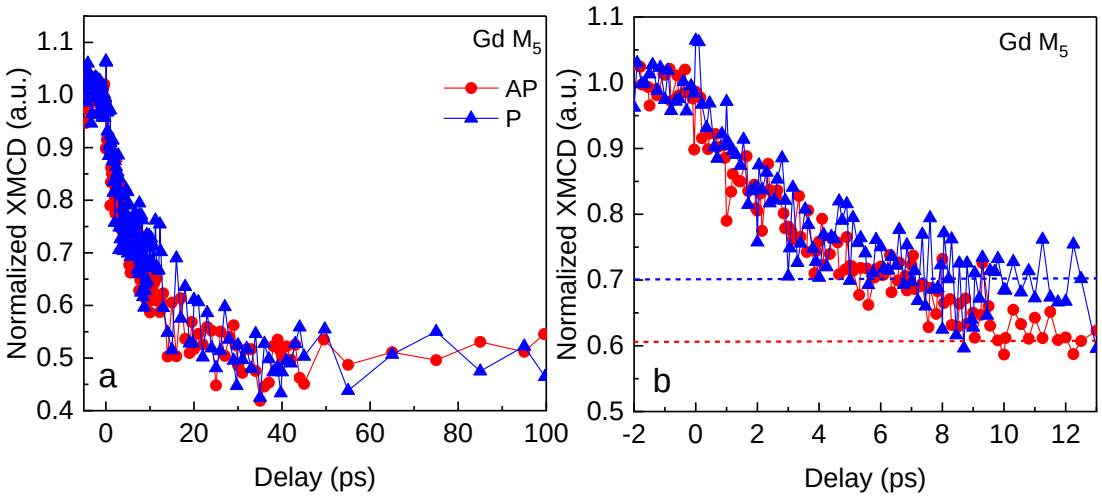

Figure 4 *Balayages du retard pompe-sonde au Gd$_{M5}$ pour l'échantillon Co$_{61}$Gd$_{39}$ (15)/Cu (4)/CoPt (3), effectués avec une fluence laser de 60mJ/cm2 à T=80 K (a) longue plage de retard jusqu'à 100 ps et (b) courte plage de retard (jusqu'à 13 ps). Les courbes bleues et rouges avec des points pleins représentent les orientations Co-Co parallèle (bleu) et antiparallèle (rouge), respectivement. La ligne pointillée bleue horizontale en (b) représente l'amplitude de démagnétisation de -30% pour P atteinte à un délai de ~ 10 ps, tandis que la ligne pointillée rouge met en évidence l'amplitude de la désaimantation de -40% dans le cas AP.*

Nous avons observé que la désaimantation du sous-réseau Gd4f est étonnamment très lente par rapport à la dynamique du Gd dans le FeGd (Fig. 3(b)). Il faut jusqu'à 30 ps pour atteindre 50 % de la désaimantation, alors que dans le FeGd, le Gd commence à se rétablir en moins de 10 ps. En outre, en raison de la faiblesse des statistiques sur la dynamique, il était très difficile d'observer l'effet.

Les effets associés à la polarisation du spin sont sensibles à la surface en raison de la longueur limitée de diffusion du spin dans les couches magnétiques (~ 7 nm pour le Fe, 4,6 nm pour le Co [50]). Il s'ensuit que la dynamique de spin induite par la SPHE est maximale dans les premiers nanomètres de nos alliages CoGd (15). Comme il est bien connu que les alliages ferrimagnétiques CoGd amorphes présentent des gradients de composition en profondeur [51], il est crucial de caractériser la surface de nos alliages CoGd.

1.4.2 Étude de surface des alliages CoxGd100-x par XPS

Dans ce travail, nous avons étudié l'effet de la concentration en Gd sur la ségrégation dans l'alliage CoGd. Pour cela, nous avons étudié deux alliages différents proches de nos compositions d'alliage par spectroscopie étudiant la dynamique ultrarapide : $Co_{80}Gd_{20}$ et $Co_{65}Gd_{35}$ (composition proche de notre système utilisé pour l'étude SPHE). Nous avons utilisé la technique de spectroscopie de photoémission de rayons X sensible à la surface, sur la ligne TEMPO, au synchrotron SOLEIL, à Paris. Nous avons enregistré les spectres XPS des niveaux de coeurs du Gd 4f et du Co 3p à des énergies de photons de 400, 700 et 1000 eV, comme le montre la figure 5(a, b).

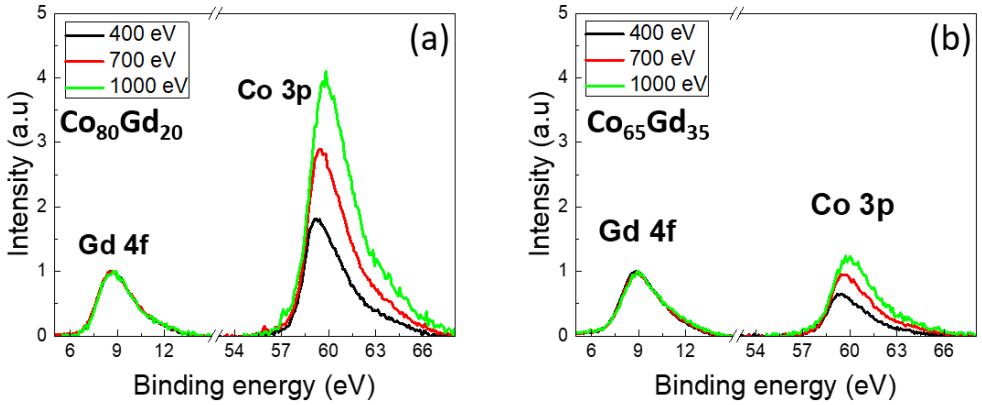

Figure 5 Spectres XPS mesurés à la transition du niveau central de Gd 4f et Co 3p pour (a) $Co_{80}Gd_{20}$, (b) $Co_{65}Gd_{35}$ pour trois énergies de photons : 400 eV (noir), 700 eV (rouge) et 1000 eV (vert). Les spectres sont normalisés par rapport au Gd 4f.

Cette mesure a permis de faire varier la sensibilité de surface des électrons émis au niveau du noyau puisque le libre parcours moyen des électrons dépend de l'énergie cinétique du photoélectron, donc de l'énergie du photon, Plus l'énergie du photon est grande, plus la profondeur de la sonde est importante. En fig 4, les spectres ont été normalisés par rapport au pic du Gd 4f pour une comparaison directe.

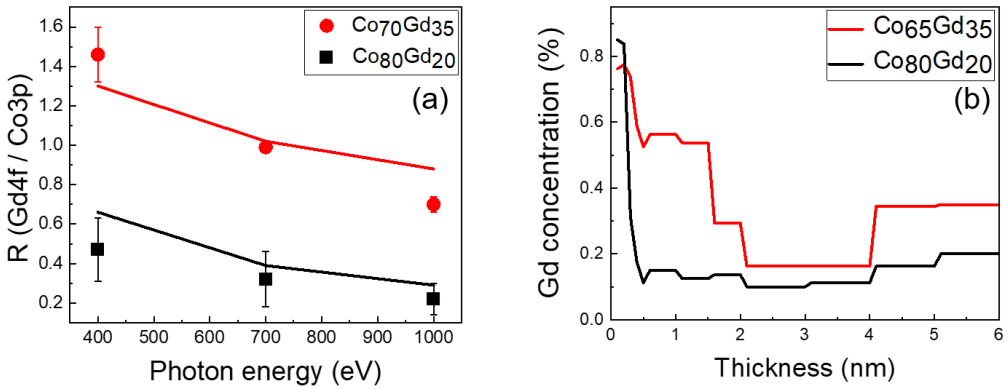

Figure 6 Comparaison entre la dépendance en énergie du rapport R= Gd 4f/ Co 3p expérimentale (symboles) et calculée (lignes pleines). (b) Profil de composition en Gd simulé à la surface de l'alliage $Co_{80}Gd_{20}$ (ligne noire) et $Co_{65}Gd_{35}$ (ligne rouge).

Afin de quantifier l'excès de Gd à la surface de l'alliage par rapport à la composition nominale, nous définissons R comme le rapport entre les surfaces des pics des niveaux de cœur du Gd 4f et du Co 3p. La dépendance de R par rapport à l'énergie des photons est illustrée dans la figure 5(a). Pour décrire le profil de la surface, un modèle a été développé, qui est expliqué en détail dans la thèse de M. Pace [13]. Ce modèle a fourni la meilleure correspondance entre calcule et expérience pour les valeurs de R en fonction de l'énergie de photons (fig 5 (a)). La spectroscopie XPS est une technique sensible à la surface, limitant donc la sensibilité de ce profil à 5 nm. Notre modèle impose donc une composition nominale de l'alliage entre 5 et 15 nm (épaisseur totale). La figure 5 (b) montre le profil calculé, qui montre clairement que la surface de l'alliage est riche en Gd. Dans le cas du $Co_{65}Gd_{35}$, cette inhomogénéité est plus importante que dans le cas du $Co_{80}Gd_{20}$. Cette forte ségrégation du Gd est présente sur plus de 2 nm en surface par rapport à la composition nominale. Par conséquent, nos observations basées sur le XPS démontrent que les alliages sont non-homogènes et que ces écarts de non-homogénéité dépendent de la composition de l'alliage en volume.

Les résultats de cette étude ont des conséquences importantes pour la description de la dynamique ultrarapide des éléments de terres rares, en particulier lorsque des techniques sensibles à la surface sont utilisées, telles que la photoémission ou la réflectométrie des rayons X. Les conséquences sont également importantes pour la spintronique ultrarapide lorsque des couches ferrimagnétiques ultraminces à base de terres rares (~5 nm) sont utilisés.

1.6 Bibliography

[1] M. H. Kryder, E. C. Gage, T. W. McDaniel, W. A. Challener, R. E. Rottmayer, G. Ju, Y.-T. Hsia, and M. F. Erden, *Heat Assisted Magnetic Recording*, Proc. IEEE **96**, 1810 (2008).

[2] M. N. Baibich, J. M. Broto, A. Fert, F. N. Van Dau, F. Petroff, P. Etienne, G. Creuzet, A. Friederich, and J. Chazelas, *Giant Magnetoresistance of (001)Fe/(001)Cr Magnetic Superlattices*, Phys. Rev. Lett. **61**, 2472 (1988).

[3] G. Binasch, P. Grünberg, F. Saurenbach, and W. Zinn, *Enhanced Magnetoresistance in Layered Magnetic Structures with Antiferromagnetic Interlayer Exchange*, Phys. Rev. B **39**, 4828 (1989).

[4] A. Fert, *Nobel Lecture: Origin, Development, and Future of Spintronics*, Rev. Mod. Phys. **80**, 1517 (2008).

[5] U. Hartmann, editor , *Magnetic Multilayers and Giant Magnetoresistance*, Vol. 37 (Springer, Berlin, Heidelberg, 2000).

[6] S. Bhatti, R. Sbiaa, A. Hirohata, H. Ohno, S. Fukami, and S. N. Piramanayagam, *Spintronics Based Random Access Memory: A Review*, Mater. Today **20**, 530 (2017).

[7] J. C. Slonczewski, *Current-Driven Excitation of Magnetic Multilayers*, J. Magn. Magn. Mater. **159**, L1 (1996).

[8] L. Berger, *Emission of Spin Waves by a Magnetic Multilayer Traversed by a Current*, Phys. Rev. B **54**, 9353 (1996).

[9] J. M. Slaughter et al., *High Density ST-MRAM Technology (Invited)*, in *2012 International Electron Devices Meeting* (2012), p. 29.3.1-29.3.4.

[10] E. Beaurepaire, J.-C. Merle, A. Daunois, and J.-Y. Bigot, *Ultrafast Spin Dynamics in Ferromagnetic Nickel*, Phys. Rev. Lett. **76**, 4250 (1996).

[11] B. Koopmans, G. Malinowski, F. Dalla Longa, D. Steiauf, M. Fähnle, T. Roth, M. Cinchetti, and M. Aeschlimann, *Explaining the Paradoxical Diversity of Ultrafast Laser-Induced Demagnetization*, Nat. Mater. **9**, 3 (2010).

[12] M. Wietstruk, A. Melnikov, C. Stamm, T. Kachel, N. Pontius, M. Sultan, C. Gahl, M. Weinelt, H. A. Dürr, and U. Bovensiepen, *Hot-Electron-Driven Enhancement of Spin-Lattice Coupling in Gd and Tb 4f Ferromagnets Observed by Femtosecond X-Ray Magnetic Circular Dichroism*, Phys. Rev. Lett. **106**, 127401 (2011).

[13] N. Bergeard, V. López-Flores, V. Halté, M. Hehn, C. Stamm, N. Pontius, E. Beaurepaire, and C. Boeglin, *Ultrafast Angular Momentum Transfer in Multisublattice Ferrimagnets*, Nat. Commun. **5**, 3466 (2014).

[14] I. Radu et al., *Ultrafast and Distinct Spin Dynamics in Magnetic Alloys*, SPIN **05**, 1550004 (2015).

[15] T. Ferté, N. Bergeard, L. Le Guyader, M. Hehn, G. Malinowski, E. Terrier, E. Otero, K. Holldack, N. Pontius, and C. Boeglin, *Element-Resolved Ultrafast Demagnetization Rates in Ferrimagnetic CoDy*, Phys. Rev. B **96**, 134303 (2017).

[16] T. Ferté, G. Malinowski, E. Terrier, V. Halté, L. L. Guyader, K. Holldack, M. Hehn, C. Boeglin, and N. Bergeard, *Laser Induced Ultrafast 3d and 4f Spin Dynamics in CoDy Ferrimagnetic Alloys as a Function of Temperature*, J. Magn. Magn. Mater. **530**, 167883 (2021).

[17] C. D. Stanciu, F. Hansteen, A. V. Kimel, A. Kirilyuk, A. Tsukamoto, A. Itoh, and Th. Rasing, *All-Optical Magnetic Recording with Circularly Polarized Light*, Phys. Rev. Lett. **99**, 047601 (2007).

[18] I. Radu et al., *Transient Ferromagnetic-like State Mediating Ultrafast Reversal of Antiferromagnetically Coupled Spins*, Nature **472**, 205 (2011).

[19] J. Stohr, *Magnetism* (Springer, Berlin, Heidelberg, 2006).

[20] E. Carpene, E. Mancini, C. Dallera, M. Brenna, E. Puppin, and S. De Silvestri, *Dynamics of Electron-Magnon Interaction and Ultrafast Demagnetization in Thin Iron Films*, Phys. Rev. B **78**, 174422 (2008).

[21] E. G. Tveten, A. Brataas, and Y. Tserkovnyak, *Electron-Magnon Scattering in Magnetic Heterostructures Far out of Equilibrium*, Phys. Rev. B **92**, 180412 (2015).

[22] M. Krauß, T. Roth, S. Alebrand, D. Steil, M. Cinchetti, M. Aeschlimann, and H. C. Schneider, *Ultrafast Demagnetization of Ferromagnetic Transition Metals: The Role of the Coulomb Interaction*, Phys. Rev. B **80**, 180407 (2009).

[23] M. Battiato, K. Carva, and P. M. Oppeneer, *Superdiffusive Spin Transport as a Mechanism of Ultrafast Demagnetization*, Phys. Rev. Lett. **105**, 027203 (2010).

[24] M. Battiato, K. Carva, and P. M. Oppeneer, *Theory of Laser-Induced Ultrafast Superdiffusive Spin Transport in Layered Heterostructures*, Phys. Rev. B **86**, 024404 (2012).

[25] G. Malinowski, F. Dalla Longa, J. H. H. Rietjens, P. V. Paluskar, R. Huijink, H. J. M. Swagten, and B. Koopmans, *Control of Speed and Efficiency of Ultrafast Demagnetization by Direct Transfer of Spin Angular Momentum*, Nat. Phys. **4**, 855 (2008).

[26] E. Turgut et al., *Controlling the Competition between Optically Induced Ultrafast Spin-Flip Scattering and Spin Transport in Magnetic Multilayers*, Phys. Rev. Lett. **110**, 197201 (2013).

[27] A. J. Schellekens, K. C. Kuiper, R. R. J. C. de Wit, and B. Koopmans, *Ultrafast Spin-Transfer Torque Driven by Femtosecond Pulsed-Laser Excitation*, Nat. Commun. **5**, 4333 (2014).

[28] M. L. M. Lalieu, P. L. J. Helgers, and B. Koopmans, *Absorption and Generation of Femtosecond Laser-Pulse Excited Spin Currents in Noncollinear Magnetic Bilayers*, Phys. Rev. B **96**, 014417 (2017).

[29] C. Stamm et al., *X-Ray Detection of Ultrashort Spin Current Pulses in Synthetic Antiferromagnets*, J. Appl. Phys. **127**, 223902 (2020).

[30] J. H. Mentink, J. Hellsvik, D. V. Afanasiev, B. A. Ivanov, A. Kirilyuk, A. V. Kimel, O. Eriksson, M. I. Katsnelson, and Th. Rasing, *Ultrafast Spin Dynamics in Multisublattice Magnets*, Phys. Rev. Lett. **108**, 057202 (2012).

[31] G.-M. Choi, B.-C. Min, K.-J. Lee, and D. G. Cahill, *Spin Current Generated by Thermally Driven Ultrafast Demagnetization*, Nat. Commun. **5**, 4334 (2014).

[32] J. Igarashi, W. Zhang, Q. Remy, E. Díaz, J.-X. Lin, J. Hohlfeld, M. Hehn, S. Mangin, J. Gorchon, and G. Malinowski, *Optically Induced Ultrafast Magnetization Switching in Ferromagnetic Spin Valves*, Nat. Mater. **22**, 6 (2023).

[33] A. Eschenlohr, M. Battiato, P. Maldonado, N. Pontius, T. Kachel, K. Holldack, R. Mitzner, A. Föhlisch, P. M. Oppeneer, and C. Stamm, *Ultrafast Spin Transport as Key to Femtosecond Demagnetization*, Nat. Mater. **12**, 332 (2013).

[34] B. Vodungbo et al., *Indirect Excitation of Ultrafast Demagnetization*, Sci. Rep. **6**, 18970 (2016).

[35] N. Bergeard, M. Hehn, S. Mangin, G. Lengaigne, F. Montaigne, M. L. M. Lalieu, B. Koopmans, and G. Malinowski, *Hot-Electron-Induced Ultrafast Demagnetization in Co/ Pt Multilayers*, Phys. Rev. Lett. **117**, 147203 (2016).

[36] N. Bergeard, M. Hehn, K. Carva, P. Baláž, S. Mangin, and G. Malinowski, *Tailoring Femtosecond Hot-Electron Pulses for Ultrafast Spin Manipulation*, Appl. Phys. Lett. **117**, 222408 (2020).

[37] T. Ferté, N. Bergeard, G. Malinowski, E. Terrier, L. Le Guyader, K. Holldack, M. Hehn, and C. Boeglin, *Ultrafast Demagnetization in Buried Co80Dy20 as Fingerprint of Hot-Electron Transport*, J. Magn. Magn. Mater. **485**, 320 (2019).

[38] T. A. Ostler et al., *Ultrafast Heating as a Sufficient Stimulus for Magnetization Reversal in a Ferrimagnet*, Nat. Commun. **3**, 666 (2012).

[39] A. Kirilyuk, A. V. Kimel, and T. Rasing, *Laser-Induced Magnetization Dynamics and Reversal in Ferrimagnetic Alloys*, Rep. Prog. Phys. **76**, 026501 (2013).

[40] L. Avilés-Félix et al., *Single-Shot All-Optical Switching of Magnetization in Tb/Co Multilayer-Based Electrodes*, Sci. Rep. **10**, 5211 (2020).

[41] T. Ferte, N. Bergeard, G. Malinowski, R. Abrudan, T. Kachel, K. Holldack, M. Hehn, and C. Boeglin, *Ultrafast Hot-Electron Induced Quenching of Tb 4 f Magnetic Order*, Phys. Rev. B **96**, 144427 (2017).

[42] S. A. Siddiqui, J. Sklenar, K. Kang, M. J. Gilbert, A. Schleife, N. Mason, and A. Hoffmann, *Metallic Antiferromagnets*, J. Appl. Phys. **128**, 040904 (2020).

[43] J. Finley and L. Liu, *Spintronics with Compensated Ferrimagnets*, Appl. Phys. Lett. **116**, 110501 (2020).

[44] S. Mangin et al., *Engineered Materials for All-Optical Helicity-Dependent Magnetic Switching*, Nat. Mater. **13**, 3 (2014).

[45] Y. Xu, M. Hehn, W. Zhao, X. Lin, G. Malinowski, and S. Mangin, *From Single to Multiple Pulse All-Optical Switching in GdFeCo Thin Films*, Phys. Rev. B **100**, 064424 (2019).

[46] J. Hintermayr, A. Ullrich, and M. Albrecht, *Structure and Magnetic Properties of Ferrimagnetic [Gd/Fe]n Multilayer and GdxFe100−x Thin Films*, AIP Adv. **11**, 095214 (2021).

[47] R. Chimata et al., *All-Thermal Switching of Amorphous Gd-Fe Alloys: Analysis of Structural Properties and Magnetization Dynamics*, Phys. Rev. B **92**, 094411 (2015).

[48] O. Eriksson, A. Bergman, L. Bergqvist, and J. Hellsvik, *Atomistic Spin Dynamics: Foundations and Applications* (Oxford university press, 2017).

[49] K. Holldack et al., *FemtoSpeX: A Versatile Optical Pump–Soft X-Ray Probe Facility with 100 Fs X-Ray Pulses of Variable Polarization*, J. Synchrotron Radiat. **21**, 1090 (2014).

[50] K.-H. Ko and G.-M. Choi, *Optical Method of Determining the Spin Diffusion Length of Ferromagnetic Metals*, J. Magn. Magn. Mater. **510**, 166945 (2020).

[51] N. Bergeard, A. Mougin, M. Izquierdo, E. Fonda, and F. Sirotti, *Correlation between Structure, Electronic Properties, and Magnetism in Co x Gd 1 − x Thin Amorphous Films*, Phys. Rev. B **96**, 064418 (2017).

[52] M. Pacé et al., *Laser Induced Ultrafast Gd 4f Spin Dynamics at the Surface of Amorphous CoxGd100-x Ferrimagnetic Alloys*, arXiv:2401.05130.

Deeksha GUPTA

Dynamique de l'aimantation ultrarapide induite par des électrons chauds polarisés dans des structures à valve de spin basées sur un ferrimagnet

Résumé

Mots clés : Magnétisme, magnétisme ultrarapide, dynamique ultrarapide, alliages de terres rares et de métaux de transition, XMCD, polarisation de spin, électrons chauds.

Les impulsions laser femtosecondes peuvent être utilisées pour induire des changements ultrarapides de l'aimantation dans les matériaux magnétiques. Plusieurs mécanismes microscopiques ont été proposés pour expliquer les observations, notamment le transport d'impulsions ultra courtes d'électrons chauds polarisés en spin (SPHE). Ces courants de spin ultrarapides suscitent un intérêt croissant en raison des défis récents de la spintronique ultrarapide, mais ils restent très mal caractérisés. L'un des principaux défis consiste à caractériser les courants ultrarapides polarisés en spin et les mécanismes microscopiques à l'origine de la manipulation de l'aimantation induite par ces SPHE, en particulier dans le cas des alliages ferrimagnétiques à fort intérêt technologique.

Dans mon travail de thèse, j'étudie la dynamique de désaimantation induite par le courant de spin sub-picoseconde dans les systèmes d'alliages de terres rares (RE) et de métaux de transition (TM). Pour distinguer la dynamique spécifique à chaque élément, j'ai utilisé la technique de dichroïsme circulaire magnétique à rayons X, résolu en temps dans une Très Grande Infrastructures de Recherche : HZB-BESSY II – Berlin.

Résumé en anglaise

Keywords: Magnetism, Ultrafast magnetism, Ultrafast demagnetization, Rare earth- Transition metal alloys, X-ray magnetic circular dichroism (XMCD), Spin polarization, Hot electrons, Spin current.

Femtosecond laser pulses can be used to induce ultrafast changes of the magnetization in magnetic materials. Several microscopic mechanisms have been proposed to explain the observations, including the transport of ultrashort spin-polarized hot-electrons (SPHE). Such ultrafast spin currents find growing interest because of the recent challenges in ultrafast spintronics however they are only poorly characterized. One of the key challenges is to characterize the spin-polarized ultrafast currents and the microscopic mechanisms behind SPHE induced manipulation of the magnetization, especially in the case of technologically relevant ferrimagnetic alloys.

In my thesis work, I investigate the sub-picosecond spin current-induced demagnetization dynamics in rare-earth (RE) and transition metal (TM) alloy systems. To distinguish the element-specific dynamics, I utilized the element selective technique of Time-resolved X-Ray Magnetic Circular Dichroism at the large-scale infrastructure HZB-BESSY II – Berlin.